Journal of Materials Chemistry A

ROYAL SOCIETY OF CHEMISTRY

REVIEW

View Article Online
View Journal | View Issue

Cite this: J. Mater. Chem. A, 2021, 9, 20131

Tuning the intrinsic catalytic activities of oxygen-evolution catalysts by doping: a comprehensive review

Sivasankara Rao Ede and Zhiping Luo *

Electrochemical water splitting produces clean hydrogen fuel as one of the pivotal alternative energies to fossil fuels in the near future. However, the anodic oxygen evolution reaction (OER) is a significant bottleneck that curtails large-scale applications of electrochemical water splitting technology, owing to its sluggish reaction kinetics. In the past few decades, various methods have been proposed to improve the OER kinetics. Among them, doping is a simple and efficient method to mold the OER kinetics of a catalyst by incorporating different or hetero atoms into the host lattice. These efforts are vital to design highly efficient OER catalysts for real-world applications. However, the OER mechanism of a doped catalyst varies, depending on the host lattice and the dopant. This review highlights different doping strategies and associated OER mechanisms of state-of-the-art catalysts, including oxides (noble metal oxides, perovskite oxides, spinel oxides, hydroxides and others), non-oxides (metal sulfides, metal selenides, metal phosphides, metal nitrides and metal carbides), and carbon-based catalysts (graphene, carbon nanotubes and others). Fundamental understanding of the doping effects on the OER from combined experimental and theoretical research provides guidelines for designing efficient catalysts.

Received 12th May 2021
Accepted 6th August 2021

DOI: 10.1039/d1ta04032d

rsc.li/materials-a

1. Introduction

The demand for transitioning the world's energy from fossil fuels to eco-friendly renewable energy is rapidly increasing, in order to cope with the depletion of fossil fuels and to curtail the associated CO_2 emission.[1] Currently, sunlight and wind are the main contributors to renewable energy, but they are highly intermittent.[2] To overcome this challenge, researchers have been working on new energy storage techniques that can sustain the erratic behavior of solar, wind and tidal energies.[3] Instead, we can store these excess energies in the form of hydrogen through water electrolysis (eqn (1)),[4] and the stored hydrogen is readily available as a fuel cell for energy production in a clean way without CO_2 emission (eqn (2)).[5]

$$2H_2O \xrightarrow{\text{electrolysis}} O_2 + 2H_2 \quad (1)$$

$$2H_2 + O_2 \rightarrow 2H_2O + \text{heat} \quad (2)$$

Hydrogen production through water electrolysis is a thermodynamically infeasible process that requires additional energy to drive this reaction, and theoretically, 1.23 V (pH = 0) electric potential is required.[6] However, the oxygen evolution reaction (OER) during the water electrolysis is associated with a sluggish reaction kinetics that comprises O=O bond formation with a loss of 4 e^-/4 H^+, requiring an even higher electric potential than the theoretical prediction.[7] The excess potential above the theoretical prediction is known as overpotential (η), which is one of the major benchmarks for denoting OER activity, along with high current density and low Tafel slope values.[8] Over the past few decades, significant research has been conducted to improve the OER kinetics through various strategies for economically viable hydrogen production.[9] So far, RuO_2 and IrO_2 catalysts have been proven to be two of the most efficient types of electrocatalyst for the OER in both acidic and alkaline media. However, the high cost associated with these catalysts hinders their large-scale water electrolysis application.[10] In alkaline media, researchers can replace these expensive catalysts with earth-abundant transition metal (TM)-based catalysts,[11] as they are stable in such alkaline environments, while being unstable in acidic media.[12,13] The catalyst stability is also an important factor for consideration.

The OER catalytic activity can be improved by enhancing the number of active sites on the surface of the catalyst, which is termed as the intrinsic activity of the catalyst.[14–22] The intrinsic activity of the OER catalyst can be augmented by introducing elemental dopants, creating vacancies, optimizing the morphology, decreasing the particle size, or *via* surface reconstruction during the OER process.[23] Among them, elemental doping is the most efficient way to engineer the activity of OER catalysts.[9] However, a fundamental understanding of OER mechanisms is required in catalyst design to shift its efficiency closer to the thermodynamic limit.[24] In the past few decades,

Department of Chemistry, Physics and Materials Science, Fayetteville State University, Fayetteville, North Carolina 28301, USA. E-mail: zluo@uncfsu.edu

several reaction mechanisms for the OER have been unveiled to fabricate efficient OER catalysts.[25]

To date, the current literature on OER catalysts lacks a comprehensive review on the doping effect in the OER mechanisms of catalysts. In this review, by corroborating experimental and theoretical results, we illustrate how particular elemental doping can improve the OER efficiency of a catalyst. In the beginning, OER intermediates by doping are listed. In particular materials, the OER mechanisms are presented, including the influence of dopant on improving the intrinsic activity through optimizing OER descriptors, such as e_g orbital occupancy, metal–oxygen covalency, and structural parameters like M–O bond binding energy, length, and angle. Various types of material that have exhibited efficient doping in the OER are reviewed. Understanding of these OER mechanisms will guide the design of new efficient OER catalysts.

2. OER mechanisms

Generally, in the OER, four electrons and protons are generated and combine on the surface of a catalyst. Several mechanisms are proposed for alkaline and acidic electrolytes; however, the research community primarily accepts the oxide[26] and electrochemical oxide[26] mechanisms. Karsil'shchikov[27] and Wade–Hackerman[28] pathways are the two known mechanisms in an acidic medium for the OER.[28] Here, the symbol * denotes an active catalytic site on the surface of the OER catalyst. In one of the reaction steps below, $2^*O \rightarrow 2^* + O_{2(g)}$ in both oxide mechanisms (Fig. 1a and c) or the electrochemical oxide mechanism (Fig. 1b and d), oxygen gas is generated. In case of recombination of two *O intermediates or generation of oxygen from the *O intermediate, oxygen evolution is impossible because of a substantial thermodynamic barrier. The oxygen gas is generated from the active catalytic site after two steps *via* the formation of intermediate *O–OH, a step which is the most sluggish one out of all rate-determining steps (RDSs) in the OER.

In acidic media, the cathodic reaction is expressed as

$$4H^+ + 4e^- \rightarrow 2H_2 \quad (3)$$

and the anodic reaction is

$$2H_2O \rightarrow O_{2(g)} + 4H^+ + 4e^- \quad (4)$$

The elementary steps of the oxide and electrochemical oxide mechanisms are described below:[26]

(a) Oxide mechanism (Fig. 1a), including reaction steps of $^* + H_2O \rightarrow {}^*OH + H^+(aq) + e^-$, $2^*OH \rightarrow {}^*O + H_2O$, $2^*O \rightarrow 2^* + O_2(g)$, $2^*O + H_2O \rightarrow {}^*O\text{–}OH + H^+ + e^-$, and $^*O\text{–}OH + H_2O \rightarrow {}^* + O_2(g) + H^+ + e^-$.

(b) Electrochemical oxide mechanism (Fig. 1b), including reaction steps of $^* + H_2O \rightarrow {}^*OH + H^+(aq) + e^-$, $2^*OH \rightarrow {}^*O + H^+(aq) + e^-$, $2^*O \rightarrow 2^* + O_2(g)$, $2^*O + H_2O \rightarrow {}^*O\text{–}OH + H^+ + e^-$, and $^*O\text{–}OH + H_2O \rightarrow {}^* + O_2(g) + H^+ + e^-$.

Likewise, in the alkaline medium, the cathodic reaction is

$$4H_2O + 4e^- \rightarrow 2H_2 + 4OH^- \quad (5)$$

and the anodic reaction is

$$4OH^- \rightarrow 2O_2(g) + 2H_2O + 4e^- \quad (6)$$

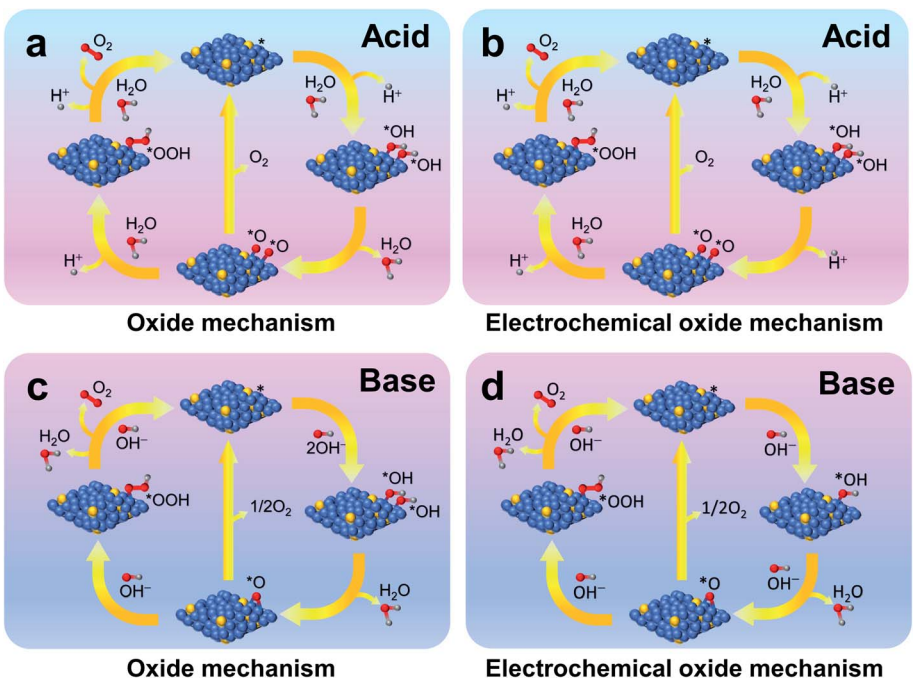

Fig. 1 Schematic illustrations of oxide (a and c) and electrochemical oxide (b and d) mechanisms of the OER in acid (a and b) and base (c and d) electrolytes, respectively.

The elementary steps of the oxide and electrochemical oxide mechanisms are described below:[26]

(a) Oxide mechanism (Fig. 1c), including reaction steps of $* + OH^- \rightarrow *OH + e^-$, $2*OH \rightarrow *O + H_2O$, $2*O \rightarrow 2* + O_2$ (g), $*O + OH^- \rightarrow *O\text{–}OH + e^-$, and $*O\text{–}OH + OH^- \rightarrow * + O_2$ (g) + H_2O.

(b) Electrochemical oxide mechanism (Fig. 1d), including reaction steps of $* + OH^- \rightarrow *OH + e^-$, $*OH + OH^- \rightarrow *O + H_2O + e^-$, $2*O \rightarrow 2* + O_2$ (g), $*O + OH^- \rightarrow *O\text{–}OH + e^-$, and $*O\text{–}OH + OH^- \rightarrow * + O_2$ (g) + H_2O.

There are three other well-known mechanisms proposed by, namely, Karsil'shchikov,[27] Yeager,[29] and Bockris,[30] in addition to the primarily recognized oxide and electrochemical oxide mechanisms.[26,28]

3. Why doping?

Besides the electrocatalyst type and chemical stability, the geometry and electronic structure are the key parameters for optimization in developing efficient OER catalysts.[31]

Geometrical surface area is the most fundamental and critical parameter, and it can be improved by synthesizing nanoforms of an electrocatalyst. By improving the specific surface area of the catalyst, the mass transfer rate and density of active catalytic sites can be accelerated.[32] However, nanomaterials are often aggregated, resulting in poor stability during long-term service.[9]

Tuning the electronic structure is another critical factor in improving the OER activities, and elemental doping is one of the best ways of tuning the electronic structure.[33] The tuning of the electronic structure by doping influences the binding energy of OER intermediates, such as *O, *OH, and *O–OH. Hence, compared with other approaches for improving OER activities, doping provides an effective way to achieve large-scale activity and long-term stability under harsh applied anodic overpotentials.

The dopant is present in trace or small amounts. Doping generates ionizable species within the host material by incorporating impurities. The ionizable species could lead to the shift of the Fermi level (E_F), enabling carrier transport with superior catalytic activity. Doping can be performed through (a) gating for direct carrier injection; (b) antisites and vacancies as structural defects; and (c) photodoping through generation of transient carrier species *via* photo-excitation. Incorporation of foreign atoms that do not produce free carriers is not considered as doping.[34]

In the following sections, we will elaborate on the influences of doping in the following common catalytic systems, including various oxides (noble metal oxides, perovskite oxides, spinel oxides, hydroxides and other oxides), non-oxides (metal sulfides, metal selenides, metal phosphides, metal nitrides, and metal carbides), and carbon-based catalysts. Fig. 2 shows the overpotential at 10 mA cm^{-2} and Tafel slope of the representative types of catalyst (data collected from the following sections). Lower overpotential and lower Tafel slopes are desirable for high catalytic performance. The effects of doping and its impacts on OER activity in the various prescribed electrocatalysts are finely discussed hereafter in terms of accelerating OER kinetics with less energy input.

4. Doping of oxide electrocatalysts

4.1 Noble metal (Ir and Ru) oxides

Table 1 provides a summary of some representative doped noble metal oxides and their catalytic performances. Both IrO_2 and RuO_2 are considered as benchmark catalysts for the OER in basic and acidic electrolytes. Under OER conditions, IrO_2 is more stable than RuO_2, but both oxides are unstable at high anodic potentials. RuO_2 leaches out into the electrolyte in the form of RuO_4 at high anodic potentials.[35] Likewise, IrO_2 also dissolves in the electrolyte by forming IrO_3 at high anodic potentials.[36] However, IrO_2 shows considerably higher stability but lower OER performance, compared to RuO_2.

Researchers doped RuO_2 with a small amount of Ir ($Ru_xIr_{1-x}O_2$) and observed a significant improvement in stability without sacrificing the OER performance.[37] Another way of enhancing the OER activity with lower total noble metal content is doping with earth-abundant metals, such as Cu,[38,39] Ni,[40] Co,[40,41] Mn,[42] Cr,[43,44] Ce,[45] W,[46] Mg,[47] and Zn.[48] For example, Cu-doped IrO_2 ($Cu_{0.3}Ir_{0.7}O_\delta$) displays improved OER activity in acidic, neutral and basic media, compared to pristine IrO_2.[39] The enhanced OER activity of $Cu_{0.3}Ir_{0.7}O_\delta$ is primarily imputed to the Jahn–Teller distortion in IrO_6 octahedra induced by Cu, as well as oxygen vacancies induced by Cu doping. Density functional theory (DFT) calculations revealed the improved OER

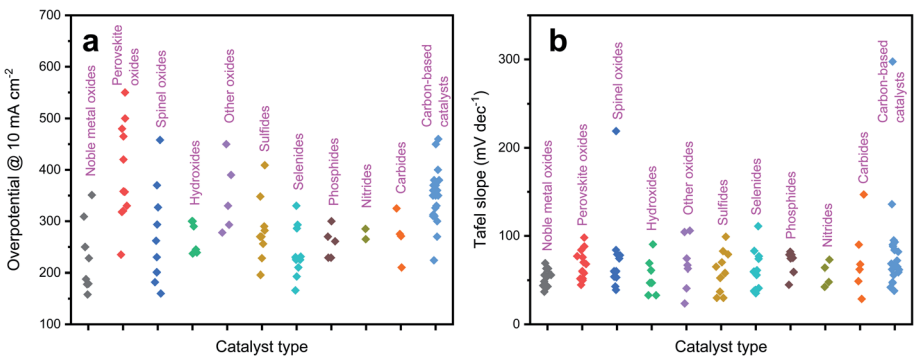

Fig. 2 Catalytic performance of representative types of catalyst: (a) overpotential @ 10 mA cm^{-2}; (b) Tafel slope.

Table 1 Summary of representative doped noble metal oxides and perovskite oxides and their catalytic performances

Catalyst	Overpotential at a specific current density	Tafel slope (mV dec^{-1})	Durability	Electrolyte
Noble metal oxides				
$Ce_{0.2}$–IrO_2@NPC[45]	224 mV @ 10 mA cm^{-2}	55.9	100 h @ 10 mA cm^{-2}	0.5 M H_2SO_4
Co-doped RuO_2 (ref. 41)	169 mV @ 10 mA cm^{-2}	63	50 h @ 10 mA cm^{-2}	0.5 M H_2SO_4
Cr-doped IrO_x (ref. 43)	250 mV @ 10 mA cm^{-2}	69	25 h @ 10 mA cm^{-2}	0.5 M H_2SO_4
$Cr_{0.6}Ru_{0.4}O_2$ (ref. 44)	178 mV @ 10 mA cm^{-2}	56	10 h @ 10 mA cm^{-2}	0.5 M H_2SO_4
Cu-doped RuO_2 (ref. 38)	188 mV @ 10 mA cm^{-2}	43.96	8 h @ 10 mA cm^{-2}	0.5 M H_2SO_4
Cu-doped IrO_2 (ref. 39)	351 mV @ 10 mA cm^{-2}	63	6000 s @ 1.68 V *vs.* RHE	0.1 M $HClO_4$
IrCoNi nanocrystals[40]	309 mV @ 10 mA cm^{-2}	53.8	—	0.5 M H_2SO_4
Mg-doped RuO_2 (ref. 47)	228 mV @ 10 mA cm^{-2}	48.66	30 h @ 1.15 V *vs.* RHE	0.5 M H_2SO_4
Mn-doped RuO_2 (ref. 42)	158 mV @ 10 mA cm^{-2}	42.94	10 h @ 10 mA cm^{-2}	0.5 M H_2SO_4
W-doped IrO_2 (ref. 46)	250 mV @ 10 mA cm^{-2}	56.6	—	0.1 M $HClO_4$
Zn-doped RuO_2 (ref. 48)	179 mV @ 10 mA cm^{-2}	36.9	20 h @ 10 mA cm^{-2}	0.5 M H_2SO_4
Perovskite oxides				
$Ba_2CoMo_{0.5}Nb_{0.5}O_{6-\delta}$[49]	445 mV @ 10 mA cm^{-2}	77	2 h @ 10 mA cm^{-2}	0.1 M KOH
$Ba_{0.5}Sr_{0.5}Co_{0.8}Fe_{0.2}O_{3-\delta}$[50]	340 mV @ 10 mA cm^{-2}	70	10 h @ 10 mA cm^{-2}	1 M KOH
$CaMn_{0.75}Nb_{0.25}O_{3-\delta}$[51]	550 mV @ 10 mA cm^{-2}	98	7000 s @ 1.65 V *vs.* RHE	0.1 M KOH
Co-doped $SrIrO_3$ (ref. 52)	235 mV @ 10 mA cm^{-2}	51.8	20 h @ 10 mA cm^{-2}	0.1 M $HClO_4$
$Pr_{0.5}Ba_{0.5}CoO_{3-\delta}$[53]	320 mV @ 10 mA cm^{-2}	60	120 min @ 5 mA cm^{-2}	0.1 M KOH
$PrBa_{0.5}Sr_{0.5}Co_{1.5}Fe_{0.5}O_{5+\delta}$[54]	358 mV @ 10 mA cm^{-2}	52	12 h @ 10 mA cm^{-2}	0.1 M KOH
P-doped $LaFeO_{3-\delta}$[55]	465 mV @ 10 mA cm^{-2}	50	—	0.1 M KOH
$SCFW_{0.4}$-BM[56]	357 mV @ 10 mA cm^{-2}	58	18 h @ 10 mA cm^{-2}	0.1 M KOH
$Sr_2Co_{1.5}Fe_{0.5}O_{6-\delta}$[57]	318 mV @ 10 mA cm^{-2}	44.8	10 h @ 10 mA cm^{-2}	1 M KOH
$SrCo_{0.95}P_{0.05}O_{3-\delta}$[58]	480 mV @ 10 mA cm^{-2}	84	7000 s @ 1.65 V *vs.* RHE	0.1 M KOH
Sr-doped $PrBaCo_2O_{5+\delta}$[59]	420 mV @ 10 mA cm^{-2}	75.8	10 h @ 0.1 mA cm^{-2}	1 M KOH
$SrCo_{0.9}Ti_{0.1}O_{3-\delta}$[60]	500 mV @ 10 mA cm^{-2}	88	10 h @ 10 mA cm^{-2}	0.1 M KOH
Yb-doped $CaMnO_3$ (ref. 61)	330 mV @ 10 mA cm^{-2}	68	1500 s @ 520 mV	0.1 M KOH

activity mechanism by the Cu doping. With the increase in Cu-doping, σ and π bonding regions become broader and shift to a lower energy level because of the occupancy of σ states. The partial density of states suggests that with an increase in Cu doping, the antibonding states of d_{xy} shift up; in contrast, d_{z^2} shifts down. The d_{xz} and d_{yz} orbitals were crossed by the Fermi level E_F, while the $d_{x^2-y^2}$ orbital is unchanged. Because of electrons hopping from d_{xz} and d_{yz} (t_{2g}) to d_{z^2}, the e_g level is partially filled as a consequence of enhanced degeneracy in Ir 5d orbitals by Cu doping. The strong interaction of e_g and O 2p orbitals facilitates bonding with oxygen intermediates during σ bond formation, which is more advantageous than the π bonding of t_{2g} orbitals.[39]

Suntivch *et al.* postulated that the OER catalyst, specifically perovskite oxide with the e_g value close to unity, will exhibit superior OER performance.[62] Later, other scientists found that the e_g filling values in some oxides also have a similar effect.[63] Site-specific deposition of a meager amount of Ir on facets of Ni nano-frameworks led to excellent OER activity in an acidic electrolyte and the catalyst even outperformed an Ir/C catalyst.[62] The oxygen adsorption of TMs was effectively tuned by doping with Ir. Similarly, Feng *et al.* reported porous IrCoNi nanocrystals as an efficient OER catalyst in highly corrosive $HClO_4$ electrolyte.[40] Fig. 3a shows the schematic illustration of IrCoNi porous hollow nanocrystals (PHNCs). A two-step process was followed to synthesize PHNCs. In the first step, IrCo single nanocrystals (SNCs) were prepared in oleylamine; and in the second step, IrCoNi PHNCs were obtained from SNCs by etching with Fe^{3+} in hexane/ethanol at room temperature. Fig. 3b shows a transmission electron microscopy (TEM) image of the as-synthesized IrCoNi PHNCs, presenting uniform hollow nanocrystals. The polarization curves of IrCo/C, IrCoNi/C, and IrNi/C PHNCs are compared with that of the Ir/C catalyst in Fig. 3c. The IrCoNi/C catalyst shows superior activity with an onset potential of 1.46 V and requires only 303 mV overpotential to achieve 10 mA cm^{-2} current density. The projected density of states (PDOS) of the d-band of Ir and IrCoNi catalysts is displayed in Fig. 3d, which shows the left side shift of the d-band center of IrCoNi from the Fermi level. The shift in the Fermi level facilitates the desired charge and discharge of OER intermediates. The schematic representation of OER reaction paths, as shown in Fig. 3e, reveals that the adsorption of OER intermediates becomes weaker when Ir is alloyed with Co and Ni, compared to pristine Ir. In another study, porous W-doped IrO_2 nanodendrites were found to exhibit superior OER performance under all pH conditions.[46] DFT calculations suggested that W doping stabilizes the IrO_2 at harsh anodic potentials by lowering the binding energies of oxygen intermediates. Qu *et al.* synthesized Cr-doped IrO_x nanowires and evaluated their OER activity in 0.5 M H_2SO_4 electrolyte.[43] The catalyst exhibits excellent OER activity with 25 h durability without any decay in activity. This high activity was ascribed to an increase in active site number and facile adsorption of OER intermediates *via* electronic structure tuning.

Like IrO_2, the OER performance and stability of RuO_2 were also enhanced by doping. Cu-doped RuO_2 porous nano-

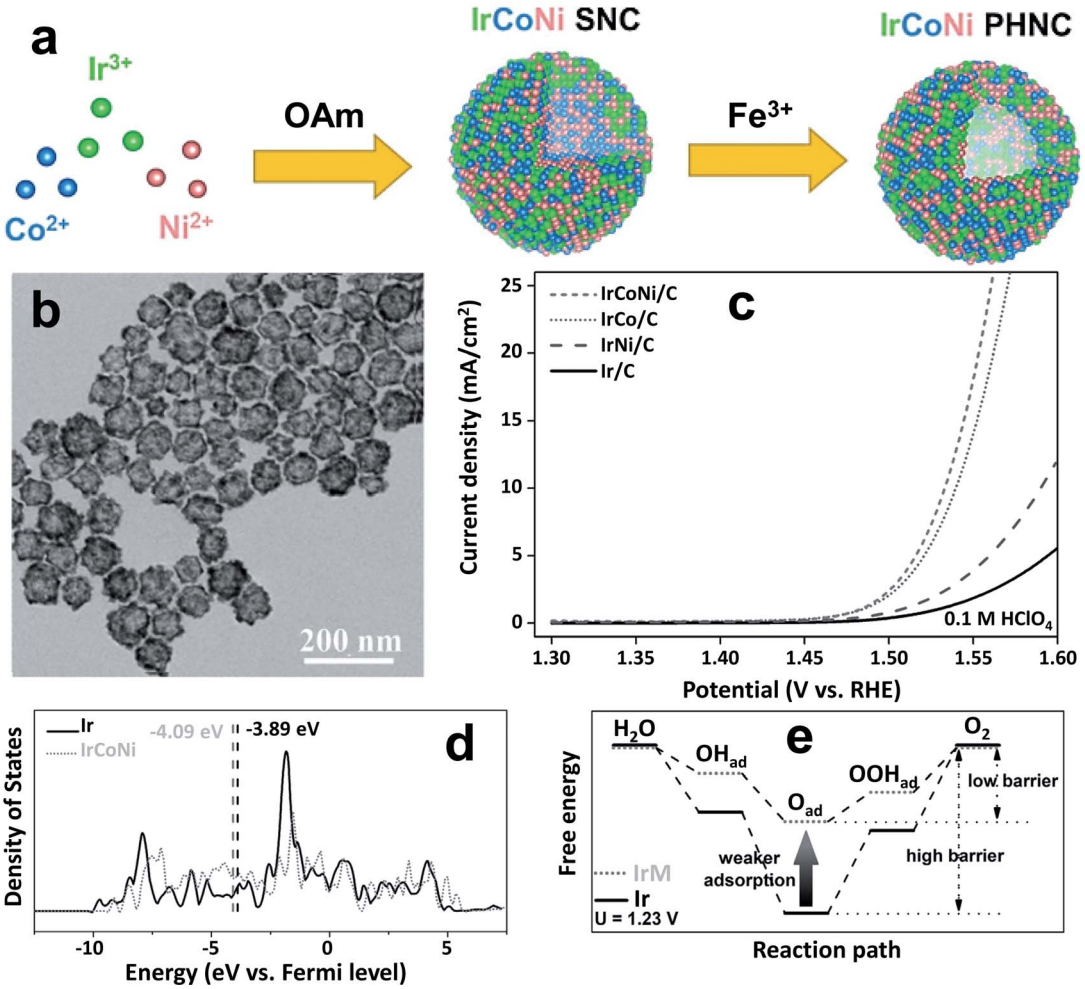

Fig. 3 (a) Schematic illustration of the formation process of IrCoNi PHNCs; (b) TEM image of the as-prepared IrCoNi PHNCs; (c) polarization curves of IrCo, IrCoNi, and IrNi for the OER with 95% *iR*-compensation; (d) projected DOS of d bands of Ir (solid) and IrCoNi models (dotted) with the corresponding d-band center denoted by dashed lines; (e) schematic illustration of reaction paths for the OER, indicating that alloying Ir with M leads to weaker adsorption of oxygen-based intermediates, thus decreasing the barrier in the reaction path.[40] Reproduced from ref. 40 with permission, © 2017 John Wiley and Sons.

polyhedra, derived from organic frameworks, are probably one of the best examples for enhancing OER activity *via* the formation of oxygen vacancies.[38] Here, most oxygen vacancies formed near Cu, causing the adjacent Ru atom to become more negative, and thus shifting the O 2p band center towards the Fermi level for superior OER activity. Recently, Chen's group reported Cr-doped RuO_2 as an efficient OER catalyst in an acidic medium derived from a metal–organic framework (MOF).[44] The schematic representation of the synthetic approach of this catalyst is shown in Fig. 4a. Initially, $RuCl_3$ was incorporated into the MOF of Cr. The resulting composite was annealed between 450 and 600 °C for 4 h, and the composite which was annealed at 550 °C showed the formation of $Cr_{0.6}Ru_{0.4}O_2$. Among $Cr_{1-x}Ru_xO_2$ catalysts, $Cr_{0.6}Ru_{0.4}O_2$ showed superior OER activity with a low overpotential of 178 mV at 10 mA cm^{-2} current density, and at the same current density, it maintained its stability for 10 h. Chromium incorporation optimizes the DOS for RuO_2 and decreases the Fermi energy level from 2.01 to 1.07 eV, which stabilizes the crystal structure of Cr-doped RuO_2. Fig. 4b displays the Ru site, which is coordinated with five atoms that act as an adsorption site for OER intermediates, and the formation of *OOH is found to be a RDS. The free energy change in the RDS is calculated to be 1.87 eV for the doped one, which is nearly 0.1 eV less than the free energy on the RuO_2 surface.[44] It was predicted that Mn doping also has a similar effect on improving the OER activity of RuO_2. Very recently, Chen *et al.* reported Mn-doped RuO_2 as an OER catalyst in an acid with a record low overpotential of 158 mV at 10 mA cm^{-2}, which was stable up to 5000 cycles at a scan rate of 100 mV s^{-1}.[42] Recently, Chen and co-workers demonstrated considerable improvement of OER activity of RuO_2 in an acid medium by doping with Mg in a one-step annealing of a Ru-exchanged MOF.[47] DFT calculations indicate the formation of oxygen vacancies on account of different oxidation states of Mg (2^+) and Ru (4^+), significantly bringing down the energy barrier for the RDS.[47]

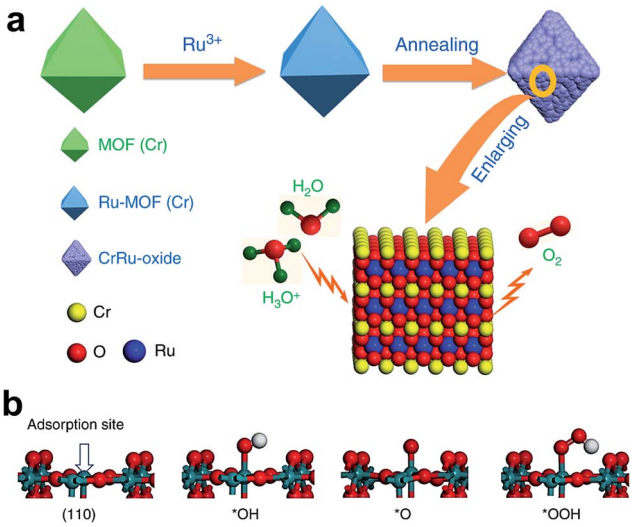

Fig. 4 (a) Schematic illustration of the preparation of $Cr_{0.6}Ru_{0.4}O_2$ electrocatalysts for OER application in acid media; (b) four-step OER process.[44] Reproduced with open access.

Creating defect-containing RuO_2 *via* doping and dopant leaching is another way of improving the OER activity and stability in acidic medium. For example, Tian *et al.* doped RuO_2 with zinc and leached it out by aging in an acid, and the catalyst displayed 179 mV overpotential and 20 h stability at a current density of 10 mA cm^{-2}.[48] The high catalytic activity is accredited to the synergetic effect of active sites and tuning of the electronic structure. Recently, an oxygen-defect-containing Ru-based catalyst was synthesized by doping with cobalt, which showed 169 mV overpotential and 50 h endurance at 10 mA cm^{-2} current density.[41] The doping generated a large amount of oxygen defects, following a vacancy-related lattice oxygen oxidation mechanism (LOM) rather than an adsorbate evolution reaction mechanism (AEM). Both computational and experimental studies elucidate this mechanism. All these studies revealed the effectiveness of doping Ir and Ru oxides for enabling higher activity and longer stability.

4.2 Perovskite oxides

Perovskite oxides are a large family of catalysts with the general formula ABO_3, where A is either an alkaline earth metal or a rare earth metal, and B is a TM. Table 1 provides a summary of some representative doped perovskite oxides and their catalytic performances. The ideal perovskite oxide displays a cubic crystal structure. The TMs are in the oxidation states of +3, +4, or a mixture of them, governed by the metal on the A-site.[18,64] The OER activity can be tailored by doping at either the A-site, B-site, or both sites to create oxygen vacancies in the perovskite.[18] The metal–oxygen hybridization depends upon the oxidation state of TMs, and the electronic properties of these perovskites rely on this parameter. The TMs with high electronegativity show high metal–oxygen hybridization, and the d-band center of the TM oxide moves closer to O 2p states as the electronegativity increases. However, besides the metal–oxygen hybridization, octahedral tilting, Jahn–Teller distortion, and displacement of B-site cations also play significant roles in governing the electronic properties of perovskite oxides.[18,65,66]

4.2.1 A-site doping. The activity and durability of $SrRuO_3$ perovskite are enhanced mainly by doping the Sr site with Na ($Sr_{0.95}Na_{0.05}RuO_3$), which results in a decrease in octahedral distortion and an increase in the oxidation state.[67] Na-doping results in no distortion in octahedra because of the change in the oxidation state of Ru with the inclusion of Na. DFT studies reveal that Na doping weakens the bonding between OER intermediates and Ru, allowing release of oxygen freely.[67] The increase in the oxidation state of Ru in Na-doped $SrRuO_3$ further improves its stability at high anodic potentials in an acidic medium. Doping of the La site of $LaCoO_3$ with Sr induces the formation of cobalt species with higher oxidation states, which influence its crystal structure in such a way that O–Co–O is aligned at 180°. As a consequence, Co 3d and O 2p orbitals are mixed efficiently to enhance the intrinsic OER activity of the perovskite.[68]

Grimaud *et al.* doped a series of lanthanides (Ln = Pr, Sm, Gd and Ho) at the A-site of $BaCoO_{3-\delta}$ to optimize the e_g filling values, thus improving the OER activity.[53] Among Ln-doped perovskites, $Pr_{0.5}Ba_{0.5}CoO_{3-\delta}$ shows superior activity. Estimated from X-ray absorption spectroscopy (XAS) and chemical titrations, the e_g filling values of all Ln-doped compounds are close to unity. However, DFT calculations suggest that hybridization of Co 3d and O 2p orbitals decreases from Pr to Ho, because of the decreased Co oxidation state with an increase in electronegativity of dopants from Pr to Ho. Similarly, when the A-site of $CaMnO_3$ is doped with Yb ($Ca_{0.9}Yb_{0.1}MnO_3$), the OER activity is found to be 100 times higher than that of the pristine sample.[61] The excellent OER performance of $Ca_{0.9}Yb_{0.1}MnO_3$ is attributed to the increased Mn^{3+}/Mn^{4+} ratio, which provides the double exchange of electrons and optimized e_g filling value of ~0.81. The OER activity of double perovskites was also tuned by doping the A-site; for instance, Sr doping of the Ba site of $PrBaCo_2O_{5+\delta}$ improves the population of Co^{4+} ions on the surface.[59] The doping enhances the ease of adsorption and deprotonation of *OOH intermediates from the catalyst surface, thus improving the OER performance of the perovskite.

4.2.2 B-site doping. It is critical to tune the electronic structure of the B site to regulate the electrochemical behavior of perovskite oxides; hence, doping the B-site is the most facile way of governing the OER performance.[49,56] For instance, Shao's group demonstrated that B-site doping of $SrTiO_3$ with cobalt and iron elements resulted in an improved electrocatalyst for the OER.[60] Among doped perovskites, $SrCo_{0.9}Ti_{0.1}O_{3-\delta}$ displayed enhanced OER activity owing to its optimized e_g filling value of 1.16, and formation of redox-active oxygen deficiency. In another report, the Mn site of $CaMnO_3$ is doped with Nb ($CaMn_{0.75}Nb_{0.25}O_{3-\delta}$), which enhances the OER performance in terms of current density by onefold, and mass activity by sevenfold, compared to the undoped perovskite.[51] The significant enhancement of electrochemical activity is imputed to the reduction of the oxidation state of Mn from +4 to +3 caused by doping with Nb^{5+}, which in turn tunes the e_g value close to unity.

Recently, researchers turned their attention to dope non-metals like phosphorus, sulfur, and silicon at the B-site to stabilize the crystal structure of perovskite oxides. An important reason for doping, specifically phosphorus, for improving electrocatalytic properties is that it has greater affinity towards combining with oxygen. Phosphorus doping at the B-site of $SrCoO_{3-\delta}$ (SC) perovskite results in tetragonal perovskite oxide $SrCo_{0.95}P_{0.05}O_{3-\delta}$ (SCP), which shows a considerable increase in OER performance in terms of activity and endurance relative to the parent compound.[58] Fig. 5a and b show linear sweep voltammetry (LSV) curves of SC and SCP before and after the accelerated degradation test (ADT) conducted by repetition of 1000 CV cycles. The ADT results show a decrease in the activity of SC after ADT, while SCP shows an increase in OER activity after the ADT. The enhanced OER activity during the ADT of SCP is due to the presence of P dopant. The high-resolution TEM (HR-TEM) images presented Fig. 5c and d suggest that the decrease in the activity of SC is because of the formation of a 10–15 nm thick amorphous layer after the ADT, which curtails the diffusion by blocking active sites, while SCP shows an only 1–2 nm thick amorphous layer (Fig. 5d). Fig. 5e shows a schematic illustration of the OER mechanism on SCP during the ADT, which indicates improved interaction between active cobalt sites and electrolyte through leaching of either Sr^{2+} or P^{5+} from the surface of the catalyst.

Likewise, Liu's group demonstrated the universality of P doping at the B-site of $LaFeO_{3-\delta}$, $LaCoO_{3-\delta}$ and $LaNiO_{3-\delta}$ perovskites for improving the electrochemical water oxidation capacity.[55] The superior activity is attributed largely to the generation of a large amount of O_2^{2-}/O^- species, and DFT calculation suggests a change in the oxidation state of the B cation that optimizes the e_g value (~1). Zou *et al.* doped a series of TMs at the B-site of 6H–$SrIrO_3$ for improving its OER activity in an acidic medium.[52] Among them, cobalt doping was found to enhance the OER activity of 6H–$SrIrO_3$ significantly. Fig. 6a presents the crystal structure of 6H–$SrIrO_3$ having two types of IrO_6 octahedron: one is face sharing (red), and the other one is corner-sharing isolated (olive green). Thus, the doped TMs can replace the Ir present in either the face sharing octahedra or corner-sharing octahedra. Fig. 6b displays the SEM image of Co-doped 6H–$SrIrO_3$ having plate-like morphology and the thickness of these plates decreased after doping. Fig. 6c shows the polarization curves of pristine and Co-doped catalysts in 0.1 M $HClO_4$ electrolyte. The catalyst with a 0.2 : 1 ratio of Co and Ir shows superior activity with the lowest overpotential of 235 mV at 10 mA cm^{-2}, and the catalytic activity is 2.5 times higher than that of the pristine catalyst. A comparison between the mass activities of pristine and Co-doped catalysts is presented in Fig. 6d, which suggests that the catalyst with the 0.2 : 1 ratio of Co and Ir has 3 times higher mass activity than 6H–$SrIrO_3$. However, both catalysts show nearly the same OER kinetics with Tafel values of 51.8 mV dec^{-1} for the catalyst with the 0.2 : 1 ratio of Co and Ir and 58.7 mV dec^{-1} for the pristine sample. Computational studies suggest that in the pristine sample, a downshift of the Ir 5d band center away from the Fermi level is observed. In contrast, the O 2p band moves close to the Fermi level in the doped 6H–$SrIrO_3$, which thus results in enhanced covalency and increases the OER activity.[52]

Very recently, our group doped Fe on the B-site of $SrCoO_{3-\delta}$ and observed the formation of a tetragonal intermediate structure between perovskite and brownmillerite, with a stoichiometric formula of $Sr_2Co_{1.5}Fe_{0.5}O_{6-\delta}$.[57] Fig. 7a presents the OER activity of Sr–Co–Fe-oxides, which shows that $Sr_2Co_{1.5}Fe_{0.5}O_{6-\delta}$ exhibits superior OER activity among all doped oxides. The enhanced OER activity is ascribed to the unique stacking of octahedral (oh) and tetrahedral (th) layered units of the tetragonal structure, as shown in Fig. 7b, providing facile interactions between the electrode and electrolyte surface. The stability of the $Sr_2Co_{1.5}Fe_{0.5}O_{6-\delta}$ catalyst was evaluated at 1.55 V for 10 h as shown in Fig. 7c, and it presents good stability with

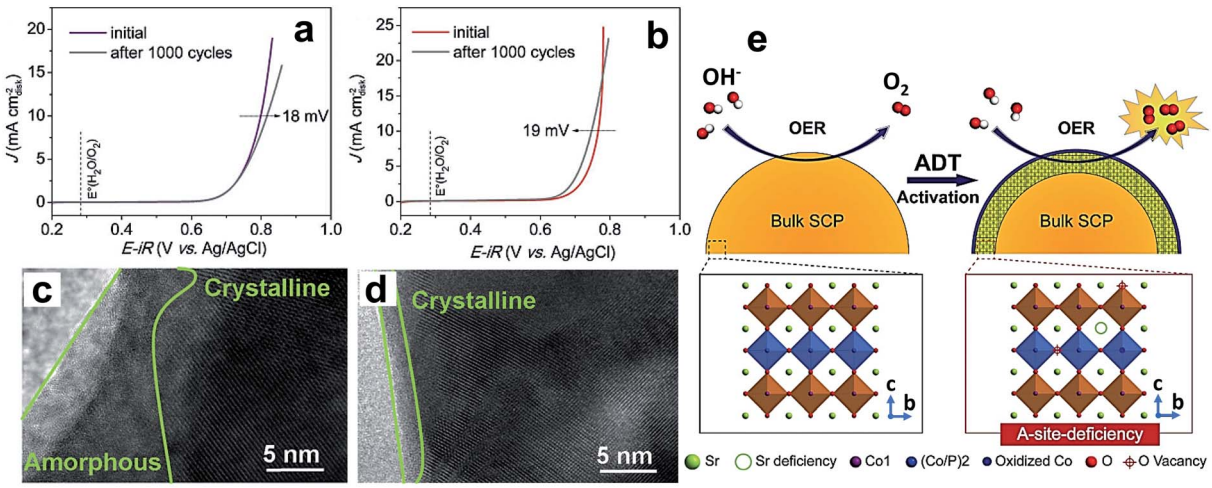

Fig. 5 (a and b) LSV curves for the OER on a RDE (1600 rpm) for the (a) SC and (b) SCP samples before and after an ADT of 1000 cycles in O_2-saturated 0.1 M KOH solution; HRTEM images of the surface regions of (c) SC and (d) SCP after an ADT of 1000 cycles; (e) schematic illustration of the main origin of the OER activation for the SCP sample during the ADT.[58] Reproduced from ref. 58 with permission, © 2017 John Wiley and Sons.

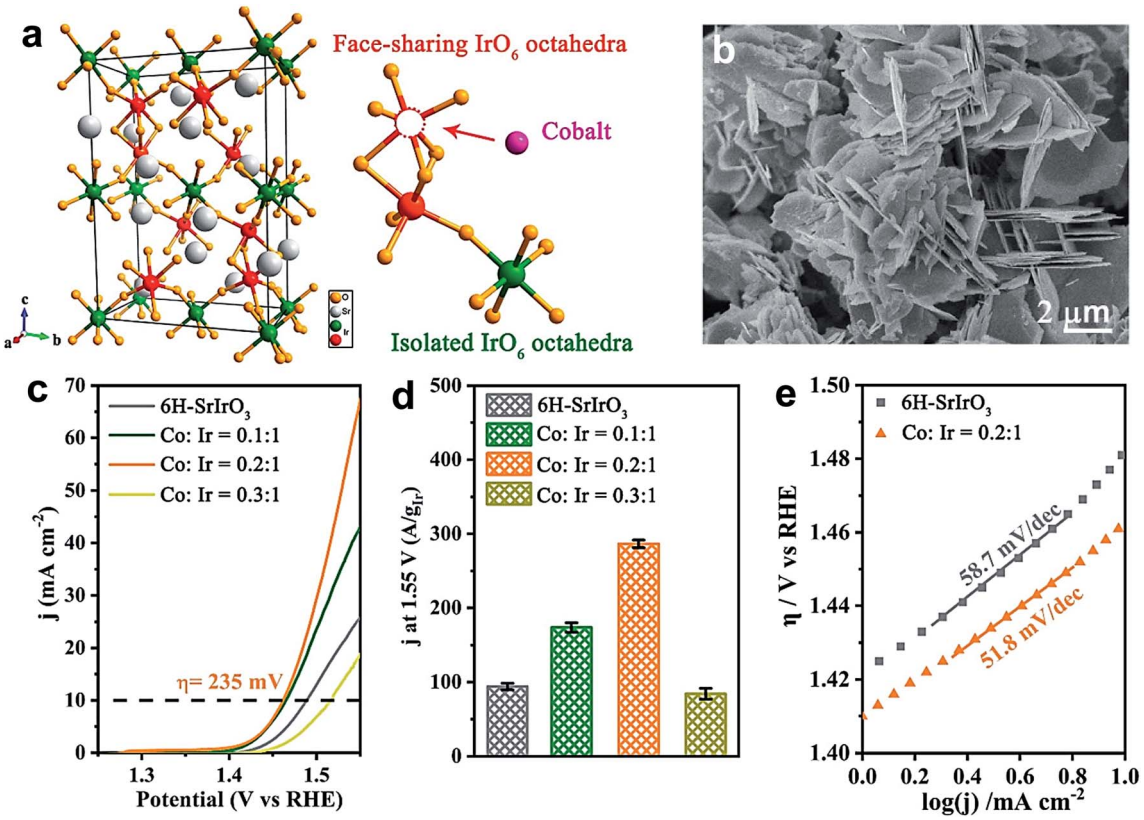

Fig. 6 (a) Crystal structure of 6H–$SrIrO_3$, and two kinds of Ir site for Co substitution. The iridium atom at face-sharing IrO_6 octahedra is marked by a red color and that at isolated IrO_6 octahedra is marked by an olive green color; (b) SEM image of Co doped 6H–$SrIrO_3$; (c) polarization curves of pure 6H–$SrIrO_3$ and Co-doped $SrIrO_3$ (Co : Ir = 0.1 : 1, 0.2 : 1, and 0.3 : 1) in 0.1 M $HClO_4$ solution with 85% *iR* compensation; (d) iridium amount-normalized mass activity of 6H–$SrIrO_3$ and Co-doped $SrIrO_3$ (Co : Ir = 0.1 : 1, 0.2 : 1, and 0.3 : 1); (e) Tafel slopes of 6H–$SrIrO_3$ and Co-doped 6H–$SrIrO_3$.[52] Reproduced from ref. 52 with permission, © 2019 American Chemical Society.

a slight increase in overpotential of 16 mV as depicted in Fig. 7d. Furthermore, theoretical calculations suggest that the enhanced covalency of Co 3d and O 2p is another prime contributor to the augmented OER performance of $Sr_2Co_{1.5}Fe_{0.5}O_{6-\delta}$. This tetragonal intermediate structure presents a model for developing advanced catalysts in other systems.

4.2.3 Both A- and B-site doping, and controlled formation of oxygen vacancies. Tuning the electrocatalytic activity of perovskites is also possible by simultaneously doping both A and B sites. $Ba_{0.5}Sr_{0.5}Co_{0.8}Fe_{0.2}O_{3-\delta}$ (BSCF) is a well-studied dual-doped perovskite, and it displayed significant intrinsic activity as a catalyst for the OER, which is an order magnitude higher than that of the benchmark catalyst IrO_2.[50] The higher activity of BSCF originates from having the e_g value close to unity, which is revealed by Shao-Horn's group by comparing several perovskite catalysts.[65] The doping of the Ba site with Sr and Co site with Fe in the double perovskite $PrBaCo_2O_{5+\delta}$ crystal structure significantly improves the OER performance.[54] Specifically, the perovskite nanofibers with the composition of $PrBa_{0.5}Sr_{0.5}Co_{1.5}Fe_{0.5}O_{5+\delta}$ displayed superior intrinsic activity that is way higher than that of the BSCF catalyst, and DFT calculations indicated that the O 2p band center was neither too close to nor too far away from the Fermi energy level. The adsorption scenarios of OER intermediates reveal that the *OH to *O conversion is the RDS, and the Fe site of Sr/Fe dual-doped $PrBaCo_2O_{5+\delta}$ requires a low overpotential (0.6 V) to initiate the reaction, while the Co site needs 0.7 V.[69] The best way to generate the oxygen vacancies in perovskites is doping a high valence A-site cation with a low valent dopant. For example, Sr doping at the A-site of $LaCoO_3$ results in ligand hole/oxygen deficiency. This deficiency increases with an increase in the Sr doping level.[70] The rise in oxygen vacancy leads to electroneutrality of the Co ion which improves the intermixing of Co 3d and O 2p orbitals. The evaluation of OER activity of a $La_{1-x}Sr_xCoO_{3-\delta}$ perovskite series (x = 0, 0.2, 0.4, 0.6, 0.8, and 1) suggests that with the increase in Sr content, the catalytic activity is improved. Furthermore, the authors evaluated *ex situ* electronic conductivity as a function of current density and found that the OER activity of the perovskite was enhanced with a large amount of Sr because of high electronic conductivity.

4.3 Spinel oxides

The general formula of spinel oxides is AB_2O_4. A and B are metal cations in general, which belong to the first row of TMs, or group 2 or group 13 in the periodic table. Table 2 provides a summary of representative doped spinel oxides and their catalytic performances. The structure of spinel oxides is complicated, because of the presence of two crystallographic

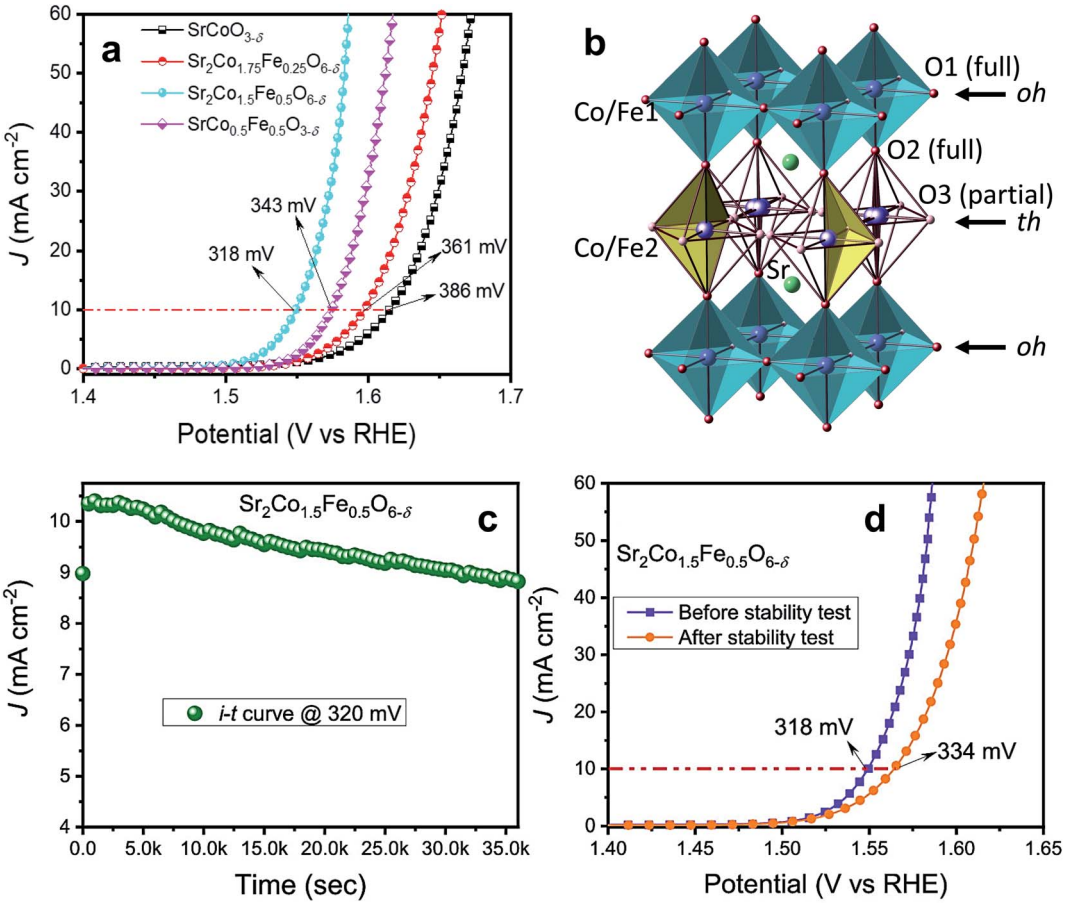

Fig. 7 (a) LSV plots of $SrCoO_{3-\delta}$, $Sr_2Co_{1.75}Fe_{0.25}O_{6-\delta}$, $Sr_2Co_{1.5}Fe_{0.5}O_{6-\delta}$ and $SrCo_{0.5}Fe_{0.5}O_{3-\delta}$ oxides; (b) structural model of the intermediate tetragonal phase containing a sequence of alternating octahedral (oh) and tetrahedral (th) layers (…oh–th–oh–th…), where only two randomly orientated tetrahedra are shown for clarity; (c) stability test of $Sr_2Co_{1.5}Fe_{0.5}O_{6-\delta}$ oxide at 1.550 V *vs.* RHE for 10 h; (d) LSV plots of samples before and after the stability test.[57] Reproduced from ref. 57 with permission, © 2021 American Chemical Society.

sites, namely octahedral oh and tetrahedral th sites, respectively, in a single structure.[22] Based on the arrangement of these crystallographic sites, they are classified into two types: one is spinel comprising A^{2+} on the th site and B^{3+} on the oh site, and the other one is inverse spinel containing A^{2+} on the oh site and B^{3+} on the th site. According to crystal field theory, the TM ions present in the oh and th sites show different d-orbital splitting, *i.e.*, $t_{2g}e_g$ for oh and e_gt_{2g} for th. This difference in d-orbital splitting plays a significant role in tuning the electronic properties of spinel oxides and optimizing OER performance.[71,72] Spinel oxides are highly stable in a basic medium with good electrical conductivity under harsh OER conditions. Mn-, Fe-, and Co-based spinel oxides are mostly reported as catalysts for the OER.[72]

4.3.1 MMn_2O_4. Mn_3O_4 is a normal spinel with Mn^{2+} on the th site and Mn^{3+} on the oh site, and its OER activity in the neutral medium is tuned by doping with various 3d-block elements such as Zn, Cu, Ni, Co, Fe, and Cr.[80] Among them, 5% Ni doping showed enhanced OER activity with better OER kinetics. Structural analysis suggests lattice distortion because Ni doping is a primary reason for improved OER activity.[80] Doping divalent metals such as Co, Zn, and Mg on the th site of Mn_3O_4 spinel results in good electrochemical properties. Specifically, Co doping is proven to be more effective in improving OER activity, and a tetragonal form of $Co_xMn_{3-x}O_4$ shows a superior activity compared to the cubic phase.[107] Enhanced OER activity of the tetragonal phase is made possible by optimizing the binding energies of OER intermediates with the defective Co (−0.26) and Mn (−0.60) sites, and the bonding energy is much lower than those of the cubic phase sites, with suppressed Jahn–Teller distortion. In $LiMn_2O_4$, lithium is on the th site, and doping of the Mn site significantly improves the OER activity. For instance, Manthiram *et al.* synthesized different morphologies (cubic, spherical, octahedral, and truncated octahedral) of $LiNi_xMn_{2-x}O_4$ and evaluated the electrochemical behavior for oxygen evolution.[108] $LiNi_{0.5}Mn_{1.5}O_4$ displayed enhanced OER activity with octahedral morphology because of the high surface area and fast reaction kinetics facilitated by the {111} crystal plane. Dismukes *et al.* doped Mg and Zn in the Li site and Co in the Mn site and found that spinel with the composition of $LiMn_{0.25}Co_{1.75}O_4$ exhibits augmented OER activity within this series.[78] From the mechanism, the superior OER activity is found to be linked with the reduction potential of the Mn(IV) cation, and greater reduction potential

Table 2 Summary of representative doped spinel oxides, hydroxides and other oxides and their catalytic performances

Catalyst	Overpotential at a specific current density	Tafel slope (mV dec^{-1})	Durability	Electrolyte
Spinel oxides				
Ag-doped Co_3O_4 (ref. 73)	680 mV @ 10 mA cm^{-2}	219	10 h @ 370 mV	0.5 M H_2SO_4
$Co_{2.25}Cr_{0.75}O_4$ (ref. 74)	350 mV @ 10 mA cm^{-2}	60	24 h @ 10 mA cm^{-2}	1 M NaOH
Cu-doped Co_3O_4 NAs/NF[75]	230 mV @ 10 mA cm^{-2}	84	20 h @ 10 mA cm^{-2}	1 M KOH
Fe-doped Co_3O_4 (ref. 76)	262 mV @ 10 mA cm^{-2}	43	50 h @ 100 mA cm^{-2}	1 M KOH
Fe-doped Co_3O_4 (ref. 77)	160 mV @ 10 mA cm^{-2}	78	~160 min @ 1.63 V *vs.* RHE	0.1 M KOH
Fe-doped $NiCo_2O_4$ (ref. 33)	201 mV @ 10 mA cm^{-2}	39	12 h @ 10 mA cm^{-2}	1 M KOH
$LiMn_{0.25}Co_{1.75}O_4$ (ref. 78)	370 mV @ 10 mA cm^{-2}	60	—	1 M NaOH
$Mn_{1.4}Co_{1.6}O_4$ (ref. 79)	327 mV @ 10 mA cm^{-2}	79	25 h @ 1.53 V *vs.* RHE	1 M KOH
Ni-doped Mn_3O_4 (ref. 80)	458 mV @ 10 mA cm^{-2}	74.4	21 h @ 10 mA cm^{-2}	3 M NaCl
NPCoO-UCSs[81]	182 mV @ 10 mA cm^{-2}	54	50 000 s @ 1.42 V *vs.* RHE	0.1 M KOH
$P_{8.6}$–Co_3O_4/NF[82]	260 mV @ 20 mA cm^{-2}	60	25 h @ 1.53 V *vs.* RHE	1 M KOH
P–Co_3O_4 (ref. 83)	280 mV @ 20 mA cm^{-2}	51.6	40 000 s @ 280 mV	1 M KOH
Se/Ni–Co_3O_4 (ref. 84)	290 mV @ 20 mA cm^{-2}	62.9	—	1 M KOH
V-doped Co_3O_4 (ref. 85)	293.6 mV @ 10 mA cm^{-2}	53.3	30 h @ 5 mA cm^{-2}	1 M KOH
Hydroxides				
Ce-doped NiFe LDH/CNT[86]	227 mV @ 10 mA cm^{-2}	33	30 000 s @ 10 mA cm^{-2}	1 M KOH
$Co_{0.54}Fe_{0.46}OOH$[87]	290 mV @ 10 mA cm^{-2}	47	—	0.1 M KOH
Cu-doped $Co(OH)_2$ (ref. 88)	300 mV @ 10 mA cm^{-2}	47	36 h @ 1.55 V *vs.* RHE	1 M KOH
Fe-doped $Co(OH)_2$ (ref. 89)	290 mV @ 10 mA cm^{-2}	69	12 h @ 10 mA cm^{-2}	1 M KOH
Fe–NiOOH[90]	181 mV @ 50 mA cm^{-2}	43.2	56 h @ 20 mA cm^{-2}	1 M NaOH
Mn and F dual-doped $Ni(OH)_2$ (ref. 91)	233 mV @ 20 mA cm^{-2}	56.9	10 h @ 20 mA cm^{-2}	1 M KOH
Ni-doped $Co(OH)_2$ (ref. 92)	300 mV @ 10 mA cm^{-2}	47	36 h @ 1.55 V *vs.* RHE	1 M KOH
Ni-doped FeOOH[93]	239 mV @ 10 mA cm^{-2}	90.4	—	1 M KOH
$Ni_{0.83}Fe_{0.17}(OH)_2$ (ref. 94)	245 mV @ 10 mA cm^{-2}	61	10 h @ 10 mA cm^{-2}	1 M KOH
Se-doped FeOOH[95]	348 mV @ 500 mA cm^{-2}	54	100 h @ 100 mA cm^{-2}	1 M KOH
W-doped $Ni(OH)_2$ (ref. 96)	237 mV @ 10 mA cm^{-2}	33	—	1 M KOH
Other oxides				
Ce-doped NiO–Au[97]	244 mV @ 100 mA cm^{-2}		>24 h @ 50 mA cm^{-2}	1 M KOH
Co-doped CuO[98]	299 mV @ 50 mA cm^{-2}	134	15 h @ 300 mV	1 M KOH
Co–MnO_2/O_V[99]	279 mV @ 20 mA cm^{-2}	75	12 h @ 10 mA cm^{-2}	1 M KOH
Co-doped ZnO[100]	450 mV @ 10 mA cm^{-2}	106	18 h @ 1.68 V *vs.* RHE	0.1 M phosphate-buffered saline
Fe–CoO/C nanofibers[101]	362 mV @ 10 mA cm^{-2}	74.4	—	1 M KOH
$Ni_xCo_{1-x}O$[102]	450 mV @ 10 mA cm^{-2}	66.8	—	1 M KOH
Ni-doped MnO_2 (ref. 103)	330 mV @ 10 mA cm^{-2}	23.7	>3 h @ 10 mA cm^{-2}	1 M KOH
V-, Fe-, Co- and Ni-doped MnO_2 (ref. 104)	390 mV @ 10 mA cm^{-2}	104.4	>27 h @ 20 mA cm^{-2}	1 M KOH
$Y_{2-x}Ba_xRu_2O_7$ (ref. 105)	278 mV @ 10 mA cm^{-2}	40.8	5 h @ 10 mA cm^{-2}	0.5 M H_2SO_4
Zn-doped CoO[106]	293 mV @ 10 mA cm^{-2}	63	24 h @ 10 mA cm^{-2}	1 M KOH

facilitates improved kinetics by directly driving surface oxidation.

4.3.2 MFe_2O_4. $CoFe_2O_4$ is an inverse spinel, in which one-eighth of the th sites are occupied by Fe^{3+} and one-half of the oh sites are occupied by Co^{2+} ions. The presence of such an arrangement provides good electrical conductivity as a consequence of electron hopping between valence states of cations on oh sites. It thus facilitates good electrochemical activity and produces longer stability in electrocatalytic reactions.[109–111] Doping of Co and Fe sites significantly influences the electrocatalytic activity of $CoFe_2O_4$. For example, Ni and Mn are doped in $CoFe_2O_4$ at the Fe site by stoichiometric mixing of Co_3O_4, Fe_2O_3, NiO, and MnO_2 using a solid-state synthesis.[109] The Ni-doped one displayed the lowest overpotential of 260 mV, which is attributed to Co(II/III) on oh sites along with Co(III) on th sites of the inverse spinel. Similarly, Ni doping at the Co site was also evaluated by synthesizing hollow nanospheres *via* a hydrothermal route. The inverse spinel $Ni_{0.75}Co_{0.25}Fe_2O_4$ showed the best OER activity, which is ascribed to the oxygen defects and cation distribution ratio on th and oh sites.[109] Singh *et al.* reported improved OER activity of $CoFe_2O_4$ through Cr doping at Fe site ($CoFe_{2-x}Cr_xO_4$), and the catalyst with the $CoFeCrO_4$ composition shows high OER activity because of fast discharge of OH^-.[111] Cr doping of $NiFe_2O_4$ at the Fe site also shows a similar result, and $NiFeCrO_4$ displayed superior activity within this series. Cr doping at the Fe site of $MnFe_2O_4$ and $CuFe_2O_4$ inverse spinels also showed improved OER activity. Doping pentavalent V into the lattice of $NiFe_2O_4$ significantly improves OER activity as well as its stability, which could be a consequence of the increased amount of Fe_2O_3 in the host lattice, along with enriched surface porosity.[110]

4.3.3 MCo_2O_4. Co_3O_4 is a normal spinel, whose Co^{2+} ions occupy th sites, while Co^{3+} ions occupy oh sites. It has been a well-known electrocatalyst for the OER in the past few decades

in alkaline media, owing to its high activity, long stability and low cost. However, pristine Co_3O_4 suffers from poor electrocatalytic activity on account of its low electronic conductivity. Doping elements like V,[85] Cr,[74] Fe,[76,77] Ni,[112] Cu,[75] Zn,[81] Ag,[73] and Li[113] into the lattice of Co_3O_4 spinel tunes its electronic structure, thus significantly improving OER activity. Incorporation of vanadium into the lattice of Co_3O_4 through doping produces a highly disordered and defect-rich surface lattice, which essentially contributes to the OER and increases its stability in an extreme OER environment. Furthermore, DFT calculations and a methanol oxidation probing method revealed that decreased energy of the RDS barrier is key to the superior activity of V-doped Co_3O_4.[85] The DFT calculations were performed on pristine and doped Co_3O_4 (100) surfaces with different OER intermediates. After V doping, the Gibbs free energy change is decreased from 1.73 eV (pristine) to 1.57 eV for the RDS, which is in accordance with methanol oxidation probing.[85] McCrory's group demonstrated the augmentation of OER performance of Co_3O_4 by the inclusion of a discrete amount of chromium ($Co_{3-x}Cr_xO_4$).[74] $Co_{2.25}Cr_{0.75}O_4$ is the most active one within the series, and its high activity is found to be caused by the increased electrophilic nature of Co^{2+} ions, thus enhancing the interaction between *O, *OH, and *OOH and active sites. Lou's group doped 13 metal atoms into the lattice of ultrathin nanosheets on the th sites of Co_3O_4 *via* a cooperative etching–coordination–reorganization approach.[76] Among these 13 atoms, doping of a discrete amount of Fe greatly increases the electrocatalytic OER activity. Fig. 8a shows the schematic representation of the synthesis of Fe-doped Co_3O_4 hierarchically hollow NPs (Fe–Co_3O_4 HHNPs). Fig. 8b–e show the SEM, HR-TEM, high-angle annular dark-field scanning TEM (HAADF-STEM), and elemental mapping images of Fe–Co_3O_4 HHNPs, respectively, which reveal that NPs are uniform having an edge size of 900 nm and a uniform distribution of a small amount of Fe. From the DFT calculations, it was found that decreased adsorption energy from 1.90 to 1.54 eV for converting *OH to *O species is a major cause.

In another report, Swaminathan *et al.* demonstrated how minute changes in the amount of Fe doping influenced the OER activity of Co_3O_4.[77] They doped 3, 4.5, and 6% of Fe into the host

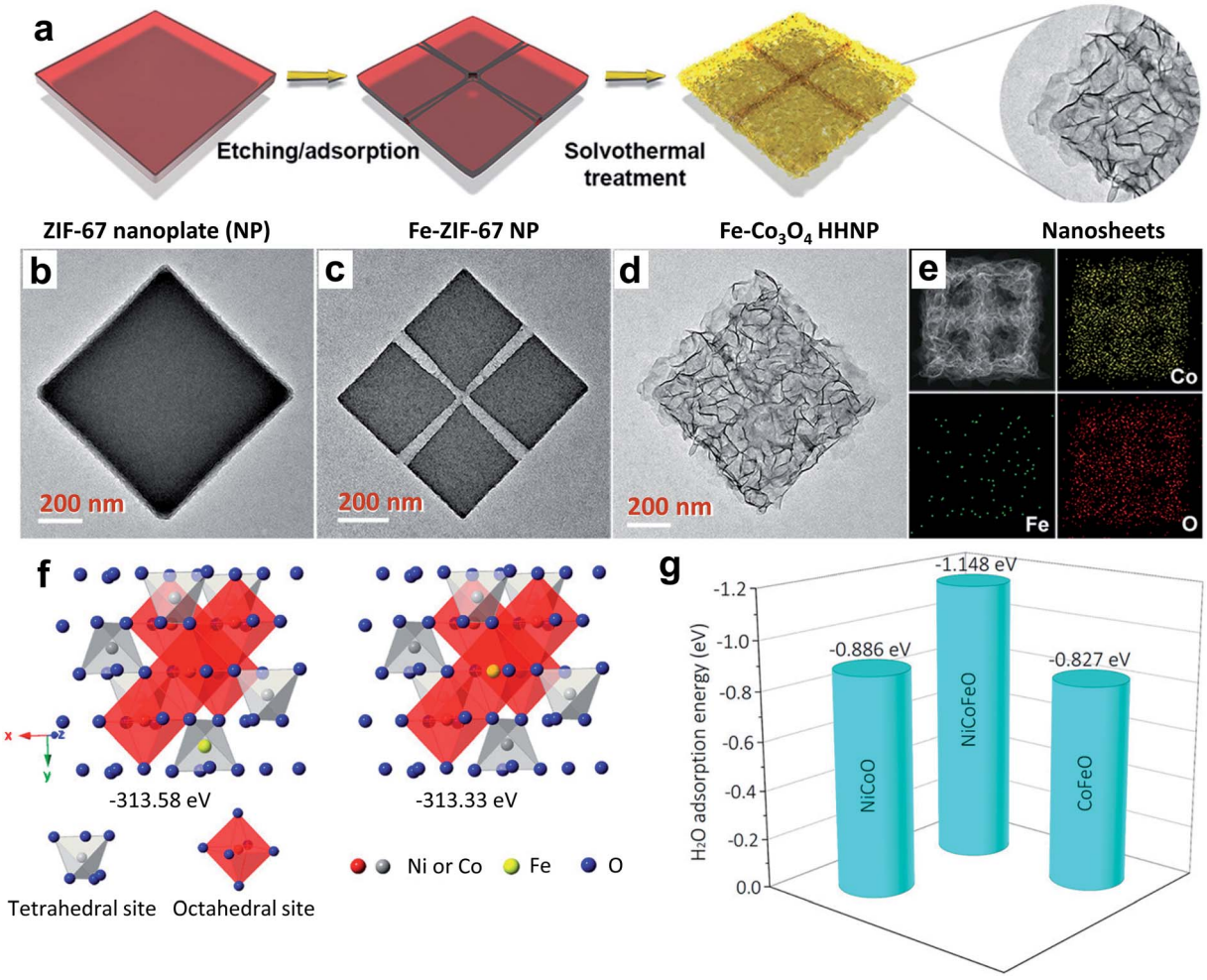

Fig. 8 (a) Schematic synthesis process of cross-channeled Fe–Co_3O_4 hierarchically hollow NPs (HHNPs); (b–d) TEM images of ZIF-67 NPs; (e) HAADF-STEM image and elemental mapping images of one Fe–Co_3O_4 HHNP.[76] Reproduced with open access. (f) Schematic illustration of the preference of Fe doping into tetrahedral sites of Ni–Co–O spinel oxides, and (g) adsorption energy of an H_2O molecule on the (001) surface of Ni–Co–O, Co–Fe–O, and Ni–Co–Fe–O spinels.[33] Reproduced from ref. 33 with permission, © 2019 American Chemical Society.

lattice and observed that above or below the optimum level of Fe doping, fading of OER activity occurred. The 4.5% Fe doping caused superior activity, and the DFT study identified a considerable downshift of the Fermi energy level, originating from the optimized adsorption energy of reaction intermediates. By comparing Ni, Cu, and Li dopants, Vitanov *et al.* studied the effectiveness of doping in improving the OER activity of Co_3O_4 spinel and noticed that doping with Li ($Li_xCo_{3-x}O_4$) produced a promising activity.[113] The raised activity of $Li_xCo_{3-x}O_4$ spinel is ascribed to faster reaction kinetics owing to the formation of active sites with high transfer coefficients, and a shortened reaction pathway to generate oxygen. Tian *et al.* revealed the Cu doping effect on improving the OER activity of Co_3O_4 nanosheets prepared on nickel foam, which outperforms the benchmark catalyst IrO_2 on nickel foam.[75] The high OER activity is found to have resulted from an increase in Co(III) species in the crystal lattice, along with highly uncovered active sites. Ding *et al.* demonstrated the improved OER performance of Co_3O_4 nanosheets by creation of oxygen vacancies upon Zn doping, which even surpassed that of the Ir/C catalyst.[81]

The stability and activity of Co_3O_4 spinel could be significantly enhanced in acidic electrolyte through Ag doping. Ag doping plays a crucial role in the growth of Co_3O_4 nanowire arrays, improving the surface area and stability under harsh acidic conditions and OER activity by providing shortened reaction paths.[73] $Ni_xCo_{2-x}O_4$ is an inverse spinel, in which Ni(II/III) is present in 16d oh sites and Co(II/III) is present in both 8a th sites and 16d oh sites. By tuning the Ni doping level, this inverse spinel's OER activity significantly increased, because the Ni^{2+}/Ni^{3+} ratio plays a key role in governing the conductivity, surface roughness, and density of active sites. For example, Zhang *et al.* systematically studied the influence of an increase in the Ni dopant level to improve the overall OER performance of $Ni_xCo_{2-x}O_4$.[112] When $x = 1$, it shows superior OER activity. In this composition, Ni is in the +3 oxidation state. The enhanced OER activity is a result of the 0.27 eV upshifting of the valence band maximum toward the Fermi level, which creates a new hole. Such an electronic configuration favors the adsorption of OER intermediates.[112] The doping of Fe at the Ni site of $NiCo_2O_4$ induces oxygen vacancies, which impacts the OER activity considerably. The $Fe_{0.1}Ni_{0.9}Co_2O_4$ composition shows superior activity within the doped series, which is accredited to the presence of an optimum amount of oxygen defects for triggering electrocatalytic activity.[114] Huang's group reported doping Fe into the th site of the $NiCo_2O_4$ lattice to improve its OER activity through a theoretical prediction.[33] As displayed in Fig. 8f, incorporation of Fe into the th site requires a lower energy (313.33 eV) compared to the oh site (313.58 eV) according to DFT calculations. Fig. 8g shows the DFT estimated H_2O adsorptive ability where the Fe-doped one is superior to the pristine one and $CoFe_2O_4$, which is highly favorable for improving OER performance to increase active sites. Furthermore, X-ray absorption spectroscopy confirms the successful incorporation of Fe into the th site of $NiCo_2O_4$, which enhances the OER performance by increasing the population of Ni^{3+} and Co^{2+} ions in oh sites. $Mn_xCo_{2-x}O_4$ is also an inverse spinel, and Mn cations preferably occupy oh sites. Lankauf *et al.* described $Mn_xCo_{2-x}O_4$ spinel by adjusting the composition of Mn ($x = 0$–2) using a soft chemistry method, and the spinel with a moderate content of Mn shows better OER activity.[79] The high activity was attributed to the improved oxidizing ability and better electronic conductivity. Chi *et al.* noticed that the change in copper content in the $Cu_xCo_{2-x}O_4$ spinel could influence its OER properties.[115] When x was increased from 0.7 to 0.9, more Cu^{2+} ions displaced Co^{3+} ions from oh sites. They occupy th sites, and thus the Co^{3+} ion population on th sites was significantly increased, resulting in superior OER performance.

Li and coworkers reported an increase in the OER performance of the $NiCo_2O_4$ catalyst through double-exchange interaction (DEI).[72] The DEI is induced by synergistic creation of oxygen vacancies (V_O) *via* doping with Fe and creating a heterojunction with MoS_2 (MoS_2/rFe–$NiCo_2O_4$) as shown in Fig. 9a. Fig. 9b and c show the SEM and TEM images of the MoS_2/rFe–$NiCo_2O_4$ catalyst, which is in the form of nanowires having a diameter of 50–60 nm, decorated with MoS_2 on Fe–$NiCo_2O_4$. Fig. 9d displays the comparative OER activity of $NoCo_2O_4$, Fe–$NoCo_2O_4$, MoS_2/Fe–$NoCo_2O_4$, rFe–$NoCo_2O_4$ and MoS_2/rFe–$NoCo_2O_4$ catalysts, which reveals that DEI has the most powerful effect on enhancing OER activity. Fig. 9e shows the schematic representation of the effect of DEI on enhancing the OER activity of MoS_2/rFe–$NiCo_2O_4$ through improving electrical conductivity, number of OER active sites, and reactivity of active centers. Recently, non-metal doping into Co_3O_4 was studied for improving electrochemical activity. For instance, Sun's group reported P-doped Co_3O_4 nanowires as an efficient OER catalyst in basic electrolyte.[82] The P-doped Co_3O_4 nanowires on nickel foam were prepared by low-temperature annealing using NaH_2PO_2. First-principles calculations revealed that P-doped Co_3O_4 nanowires have a much lower free-energy value for the rate-determining step than pristine Co_3O_4.[82] Wang *et al.* synthesized P-doped Co_3O_4 spinel by filling the *in situ* generated oxygen vacancies using an Ar plasma etching technique, and observed excellent OER activities after doping.[83] When oxygen vacancies were created in Co_3O_4, more electrons migrated into oh Co^{3+} 3d orbitals than th Co^{2+} 3d orbitals. With P doping, electrons are transferred out of the Co 3d states, resulting in more Co^{2+} on th sites than Co^{3+} on oh sites in P–Co_3O_4. Hence, the superior OER activity of the P-doped Co_3O_4 is linked with the presence of a greater number of Co^{2+} ions. Zhang *et al.* reported doping of Co_3O_4 with S by using facile solution-combustion and thioacetamide-sulfidation methods.[116] The S-doping enhances the OER performance of Co_3O_4 in terms of activity as well as stability in an alkaline medium. The formation of S-substituted CoO layers on the surface of Co_3O_4 is a major reason for the superior activity. Theoretical calculations indicate that improving the electronic conductivity by S doping was beneficial for overall electrochemical activity. Dual doping of Co_3O_4 on both cation and anion sites with Ni and Se, respectively, resulted in a significant increase in its OER performance.[84] The Se doping enhances the active sites on the surface of a catalyst by inducing oxygen vacancies, and Ni doping helps in generating highly active Co^{4+} species.

4.4 Hydroxides

Hydroxides, oxyhydroxides, and layered double hydroxides (LDHs) of oxides of TMs, such as Ni, Co, Fe, Mn, and V, are

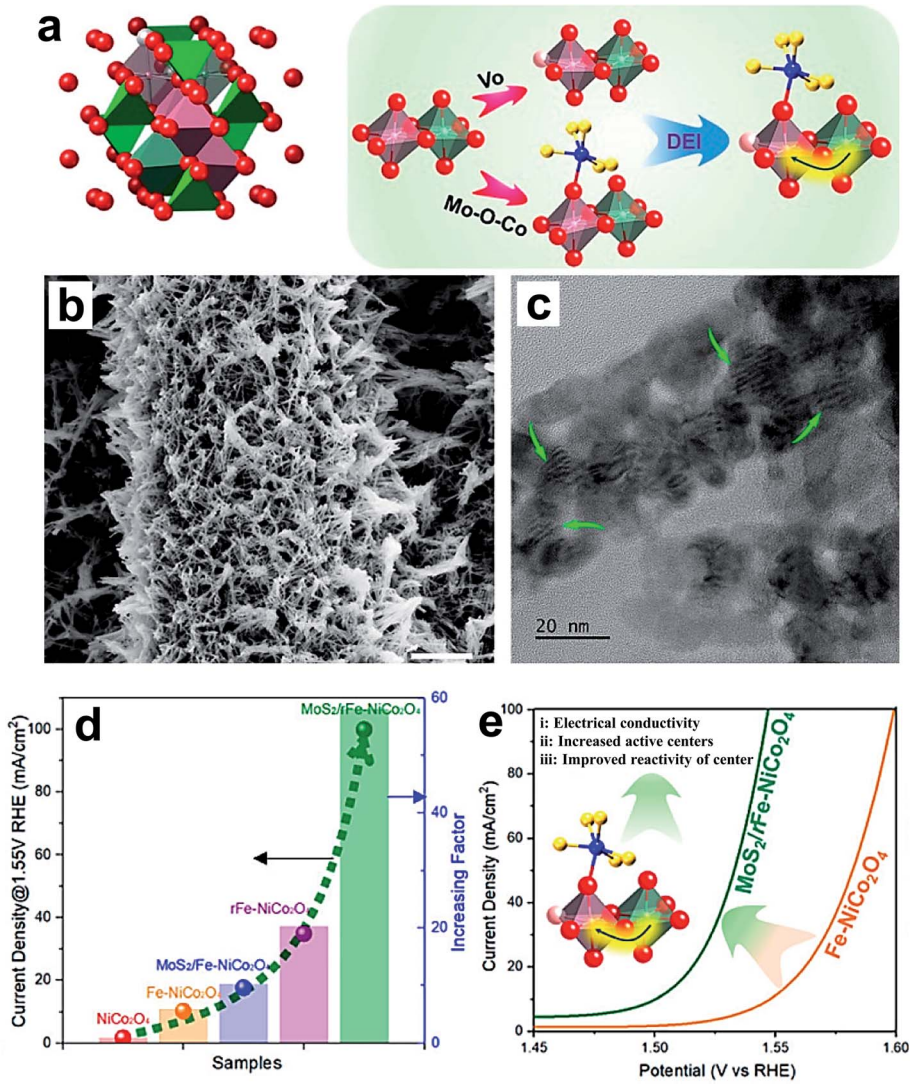

Fig. 9 (a) Crystal structure of spinel oxides, and the creation of a double-exchange interaction (DEI); (b) SEM and (c) TEM images of MoS_2/rFe–$NiCo_2O_4$; (d) OER performance of the electrocatalysts $NiCo_2O_4$, Fe–$NiCo_2O_4$, MoS_2/Fe–$NiCo_2O_4$, rFe–$NiCo_2O_4$, and MoS_2/rFe–$NiCo_2O_4$ with respect to current density at 1.55 V RHE and the current density increasing factor; (e) schematic representation of the enhanced OER arising from the DEI effect.[72] Reproduced from ref. 72 with permission, © 2020 American Chemical Society.

highly active in the electrocatalytic oxygen evolution reaction.[86,117,118] They exhibit typical layered stacking conformation with proton sandwiching between layers, and the metal is centered in the octahedron surrounded by oxygen anions at the corners as MO_6.[117] Some representative hydroxides and their catalytic performances are listed in Table 2.

Fe doping of TM hydroxides is most widely reported in the literature for enhancing their OER performance.[119] Specifically, Fe doping in $Ni(OH)_2$ (ref. 94 and 120–123) and $Co(OH)_2$ (ref. 89 and 124–126) has been widely studied. In 1901, Edison,[127] for the first time, noticed an increase in the OER activity of $Ni(OH)_2$ because of Fe impurity in the electrolyte in a Ni-based alkaline battery.[120,128] Because of oxygen evolution, the capacitance and cycle life of the battery were decreased considerably by the incorporation of Fe into the $Ni(OH)_2$ electrode. Later, researchers revealed that the OER activity of $Ni(OH)_2$ shortened the voltage window of the battery owing to the presence of Fe in the electrolyte, and they also found that the presence of a discrete amount of Fe (<1%) considerably contributed to augmentation of OER activity.[129] Corrigan demonstrated that the presence of 0.01% Fe impurity in electrolytes substantially decreased the discharge capacitance.[130]

Boettcher's group studied the role of Fe doping in enhancing the OER performance of $Ni(OH)_2$ thin films and provided more insights on catalytic reactions at the electrode/electrolyte interface.[122,124–126] They witnessed an increase in conductivity of thin films with systematically increasing the doping amount from 5 to 25%. Still, the CV curves show drastic changes, which signify the change in surface reconstruction with varying dopant levels.[122] Klaus *et al.* studied the Fe inclusion by aging the thin films in an electrolyte with or without Fe impurities for 6 days.[131] The sample aged in the electrolyte with Fe impurity

shows an increase in OER activity gradually from the first day to the 6th day. In contrast, the other one without Fe shows a decrease in activity gradually upon aging, and the enhanced OER activity is attributed to the increase in conductivity. Landon *et al.* noticed a rise in the coordination number of Fe in the OER environment using an *in situ* extended X-ray absorption fine structure (EXAFS) method.[132] They proposed that forming a new phase ($NiFe_2O_4$) through reconstruction increased the coordination number of Fe. Nevertheless, the formation of $NiFe_2O_4$ is rejected by other researchers with the aid of *in situ* Raman spectroscopy.[133] They did not notice any signals for $NiFe_2O_4$ formation in the *in situ* Raman spectra (700 cm^{-1}), even after aging in KOH electrolyte with Fe at high OER potentials. In contrast, they observed two peaks which are characteristic of the NiOOH phase at 555 and 475 cm^{-1}, even in the presence of a high percentage of Fe.

Recently, Zhao's group studied the effect of doping Co and Fe into the lattice of $Ni(OH)_2$ for improving the OER performance, and they conducted electron energy-loss spectroscopy (EELS) characterization and Hubbard corrected density functional theory (DFT + *U*) calculations to understand the activity trend.[90] The Fe-doped sample shows superior OER activity to Co and Fe co-doped or Co-doped samples.[90] EELS analysis suggests electronic interactions between Ni, Co, and Fe dopants even after surface reconstruction during the OER process. A DFT + *U* study reveals that the d-band center of the Fe-doped sample is much closer to the Fermi level than that of the others, enhancing the binding energy values of OER intermediates to an optimal value. Wang *et al.* demonstrated an enhancement in OER activity of $Ni(OH)_2$ by co-doping Mn and F elements.[91] A considerable increase in oxygen deficiencies was found after doping, which reduced the energy barrier for the key OER of *OH → *O. Ma's group doped a single atom of W^{6+} into the lattice of $Ni(OH)_2$ and studied its electrocatalytic oxygen evolution behavior.[96] Interestingly, W doping significantly enhances the OER activity compared to the pristine sample, and the superior activity is ascribed to the boosting of carrier migration at the interface of the electrode and electrolyte. Furthermore, a DFT study reveals that low spin W^{6+} (d^0) stabilizes the O* and thus helps in the formation of O–O.

The augmentation of OER activity was also reported for the $Co(OH)_2$ catalyst by Fe doping. Boettcher's group reported the effect of Fe doping on the OER activity of electrodeposited films of $Co(OH)_2$.[124] They observed an enhancement of OER performance by 100 fold when the stoichiometric ratio of Co and Fe was 1 : 0.6–0.7. The reason for the superior OER activity is increased Co^{3+} population and improved thin-film conductivity with Fe doping. Unlike $Ni(OH)_2$, $Co(OH)_2$ requires a huge amount of Fe doping (60–70%) to display enhanced OER activity, while $Ni(OH)_2$ shows a significant effect even with 0.01% Fe inclusion. Above the 60–70% level, the OER activity started decreasing for $Co(OH)_2$. Researchers also doped other TMs into $Co(OH)_2$ to improve its OER performance. For example, Chen *et al.* doped Cu into the lattice of $Co(OH)_2$, which significantly enhances its OER activity and outperforms the state-of-the-art catalyst IrO_2. The considerable increase in the catalytic performance is attributed to an increase in Co^{3+} population after doping with Cu.[88] Koel's group studied the doping effect on the OER behavior of CoOOH nanowires by doping with Ni and Mn.[92] Among them, Ni doping turned out to be fruitful compared to Mn doping because of Ni's ability to stabilize the OER intermediates. Similarly, FeOOH was also doped with different elements such as Ni, Co, and Se to enhance its OER performance. Tolstoy *et al.* doped Ni^{2+} into the lattice of FeOOH nanocrystals, and 25% Ni^{2+} doping was proven to improve the OER activity considerably.[93] Zhang *et al.* doped Co into FeOOH, and the $Co_{0.54}Fe_{0.46}OOH$ composition showed superior activity to other doped samples because Co inclusion created more active sites at the edges of the three-dimensional hierarchical structures.[87] Recently, Niu *et al.* reported doping of Se into FeOOH *via* electrochemical oxidation of an FeSe/iron foam (IF) pre-catalyst by applying a constant 10 mA cm^{-2} current density for 4 h.[95] XRD patterns, as shown in Fig. 10a, display the complete disappearance of diffraction peaks of FeSe which was converted into Se-doped FeOOH. However, the electrochemical oxidation did not disturb the nanosheet morphology as revealed by SEM and TEM images in Fig. 10b and c, respectively. Fig. 10d shows the polarization curves of the as-prepared catalysts, and among them, FeOOH(Se)/IF delivers industrial scale 500 mA cm^{-2} current density at 348 mV overpotential. Tafel plots of these catalysts are presented in the inset of Fig. 10d, which shows that the FeOOH(Se)/IF catalyst possesses OER kinetics with the lowest Tafel slope value of 54 mV dec^{-1}. As a unary Fe-based catalyst, FeOOH(Se)/IF shows comparative activity and even outperforms Ni and Co-based OER catalysts as observed in Fig. 10e. Furthermore, DFT calculations revealed a considerable decrease in the energy barrier for the RDS from 3.20 eV to 1.45 eV after Se inclusion, which accounts for the superior OER activity.

4.5 Other oxides

TM oxides, such as NiO, CoO, and MnO_2, are widely reported as catalysts for the OER owing to their high durability and low cost.[5] Some other representative oxides and their catalytic performances are listed in Table 2. The electrochemical activity of these oxides was further improved by tuning their electronic structure through the inclusion of various dopants. For instance, lithium-doped NiO ($Li_xNi_{1-x}O$) has shown unprecedented OER performance and even outperformed non-noble benchmark perovskite catalysts, such as BSCF and $LaNiO_3$.[134] Zhang *et al.* studied the role of lithium incorporation into the lattice of NiO.[134] Fig. 11a shows the BET surface area normalized LSV curves of pristine and Li-doped NiO catalysts, and among them, the catalyst with a 1 : 1 ratio of Li and Ni shows 11 fold higher activity than pristine NiO. The inset of Fig. 11a presents cyclic voltammogram (CV) curves, which further reveals a positive shift in redox potential with an increase in Li content. A combinatorial study of the electronic structure of $Li_xNi_{1-x}O$ was conducted using X-ray absorption spectroscopy and synchrotron-based photoemission spectroscopy. The schematic illustration of covalency of Ni 3d–O 2p from DFT calculations is shown in Fig. 11b, which reveals the formation of a new hole state near the Fermi level, and the increased covalency of Ni 3d–O 2p that ensured higher OER activity.

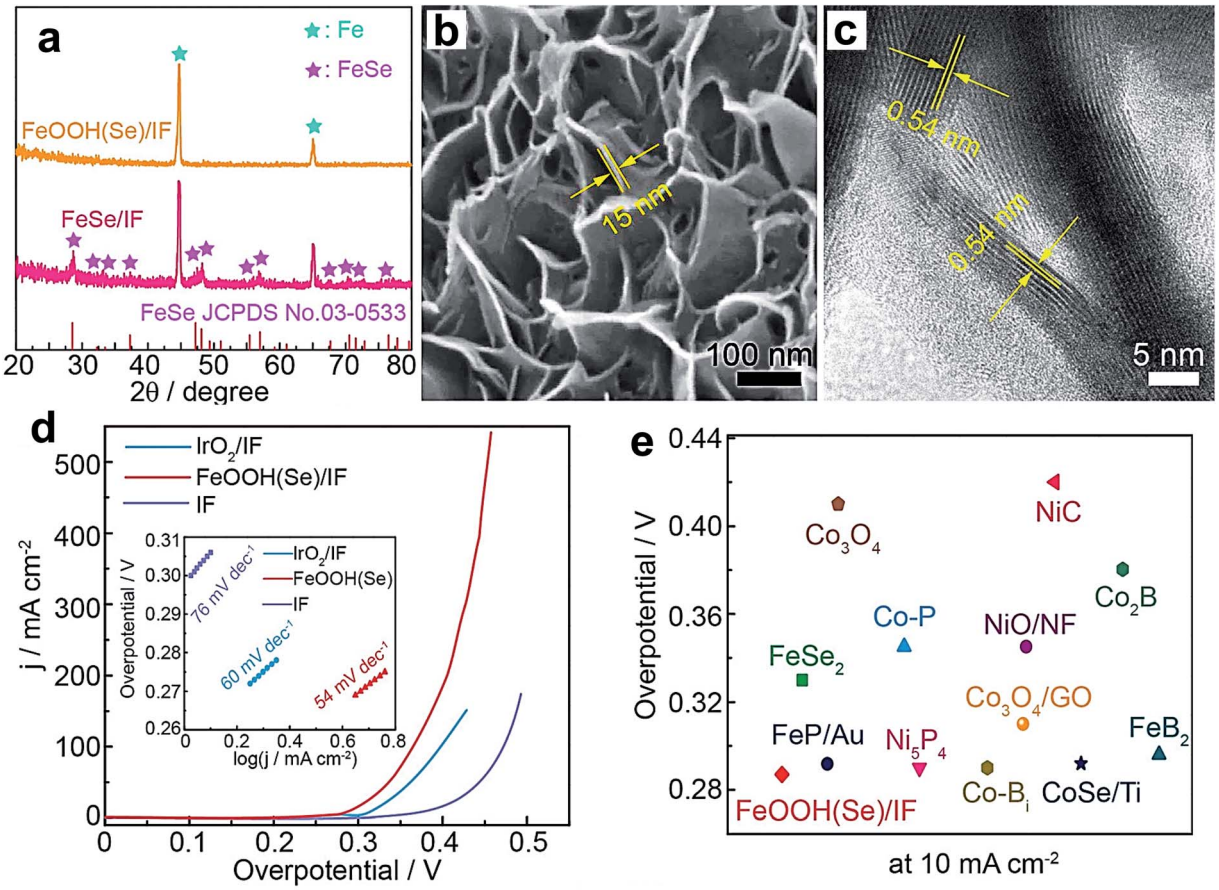

Fig. 10 (a) XRD patterns of FeSe/iron foam (IF) and FeOOH(Se)/IF; (b) SEM image of FeSe/IF; (c) HRTEM image of FeSe/IF; (d) LSV curves of the as-prepared catalysts (inset: Tafel plots); (e) overpotential comparison of FeOOH(Se)/IF and state-of-the-art unary metal-based OER electrocatalysts.[95] Reproduced from ref. 95 with permission, © 2019 American Chemical Society.

Enhancement in the OER activity of the NiO catalyst with Fe doping was first observed by Corrigan in 1987,[130] and Fe doping into the NiO thin film was found to be affected by the impurities present in KOH electrolyte.[135] Recently, Nocera *et al.* identified the essential role of Fe doping in improving the electrocatalytic activity of Ni oxides.[136] 5–10% doping of Fe increased the population of Ni^{4+} ions, as revealed by coulometric titrations. Consequently, O and Ni K-edge spectra indicated an increase in hybridization between Ni 3d and O 2p orbitals. Both experimental and computational studies showed that Fe^{3+} is a Lewis

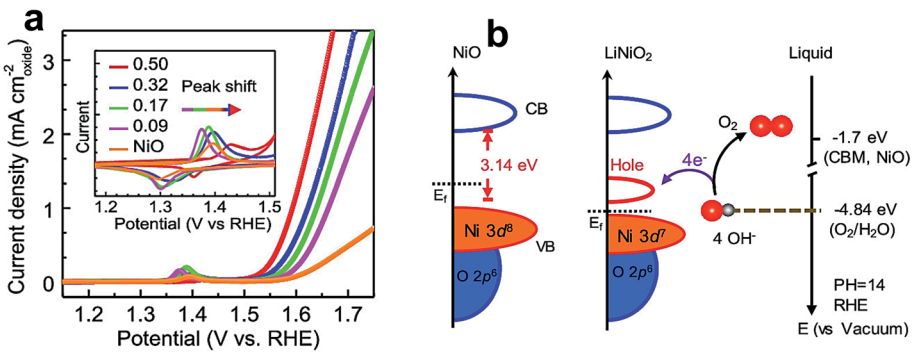

Fig. 11 (a) LSV polarization curves of the OER normalized by the BET surface area in 1 M KOH solution at a scan rate of 10 mV s^{-1}; the inset shows cyclic voltammogram curves at a scan rate of 10 mV s^{-1}; (b) schematic diagram for electronic structures of NiO (left) and $LiNiO_2$ (middle), and energy diagram at the oxide–liquid interface on the vacuum level scale at pH = 14 (right); the redox level for O_2/H_2O (red dashed line) is −4.84 eV, the conduction band minimum (CBM) level for NiO is −1.7 eV according to the formula $E_{CBM} = E_{bandgap} - E_{ionization}$ ($E_{bandgap}$ = 3.7 eV, $E_{ionization}$ = 5.4 eV).[134] Reproduced from ref. 134 with permission, © 2019 American Chemical Society.

acid with $pK_a = 2.2$, and is the most acidic among TMs. Hence, the incorporation of Fe^{3+} into Ni oxides helps in enhancing the acidity of OH_x moieties coordinated with Ni, which increases the population of Ni^{4+} ions by lowering the Ni^{3+}/Ni^{4+} reduction potential.[136] Ce-doped NiO_x deposited on a Au substrate shows significantly higher OER performance than pristine NiO_x.[97] The enhanced OER activity is accredited to the modification of the local environment favorable for binding of OER intermediates.

A nickel-doped rock-salt-structured OER catalyst, $Ni_xCo_{1-x}O$, was synthesized using a solid-state method.[102] The inclusion of a discrete amount of Ni into the lattice of CoO stabilizes the crystal structure and tunes its e_g value. Within the doped series, the $Ni_{0.3}Co_{0.7}O$ catalyst displays the highest OER activity with an e_g value of ~1.3. Huo *et al.* reported the improved OER performance of CoO nanoflowers by doping with Zn.[106] A DFT study confirmed that OER active sites were increased by Zn doping, and the high surface area of nanoflowers was another contributor to the improved catalytic activity. Like in NiO, Fe doping of CoO could also greatly enhance its electrocatalytic performance by increasing the number of OER active sites.[101] Ye *et al.* prepared V-, Fe-, Co-, and Ni-doped MnO_2 ultrathin nanosheets on carbon fiber paper (CFP) using an electrodeposition method as shown in Fig. 12a, and studied their OER activity in a basic medium.[104] Fig. 12b and c show the doped MnO_2 ultrathin nanosheet/CFP composite electrode at low and high magnifications, which shows very dense nanoclusters with 5 nm thick nanosheets. Fig. 12d shows the LSV curves of CFP, pure MnO_2/CFP, metal-ion-doped MnO_2 ultrathin nanosheet/CFP, and IrO_2/CFP composite electrodes in 1 M KOH with a scan rate of 5 mV s^{-1}. The authors noticed that doping with these TM cations vastly enhances MnO_2 conductivity, resulting in higher catalytic activity compared to the pristine sample. The electrochemical stability of doped and pristine MnO_2 compared with IrO_2 evaluated at 20 mA cm^{-2} is shown in Fig. 12e. Doped MnO_2 ultrathin nanosheet/CFP shows significant stability compared to the pristine sample with a slight increase in overpotential.

Yang *et al.* intercalated 3d block metal cations such as Zn^{2+}, Cu^{2+}, Ni^{2+}, Co^{2+}, and Fe^{3+} into MnO_2 nanosheets to enhance OER activity.[103] Among them, the inclusion of Ni^{2+} ions was more effective in enhancing the OER activity of MnO_2 nanosheets. The increased activity is associated with strengthening the Mn–O bond perpendicular to layered chains to promote the catalysis between two Mn sites. Oxygen vacancy formation in MnO_2 nanosheets by Co doping is demonstrated by Zhao *et al.*[99] Co doping enhances the OER activity of MnO_2 considerably by enhancing its conductivity and decreasing the energy barrier for adsorption of OER intermediates on the catalyst surface. Interestingly, a small amount of cobalt doping (3.47%) could activate the OER activity of ZnO. Theoretical studies suggest that Co activates inherently inactive adjacent Zn sites by increasing conductivity, which act as OER active sites for adsorption of OER intermediates.[100] Co doping also activates the OER activity in CuO. Sun *et al.* demonstrated a multifold enhancement of OER activity in a basic electrolyte after doping with Co on a Cu foam substrate,[98] which was related to a change in the electronic structure of CuO by Co doping. Meyer *et al.* reported the fabrication of an OER catalyst by modifying fluorine-doped tin oxide (FTO) by Co^{2+} single-atom doping.[137] X-ray photoelectron spectroscopy (XPS) and TEM reveal that

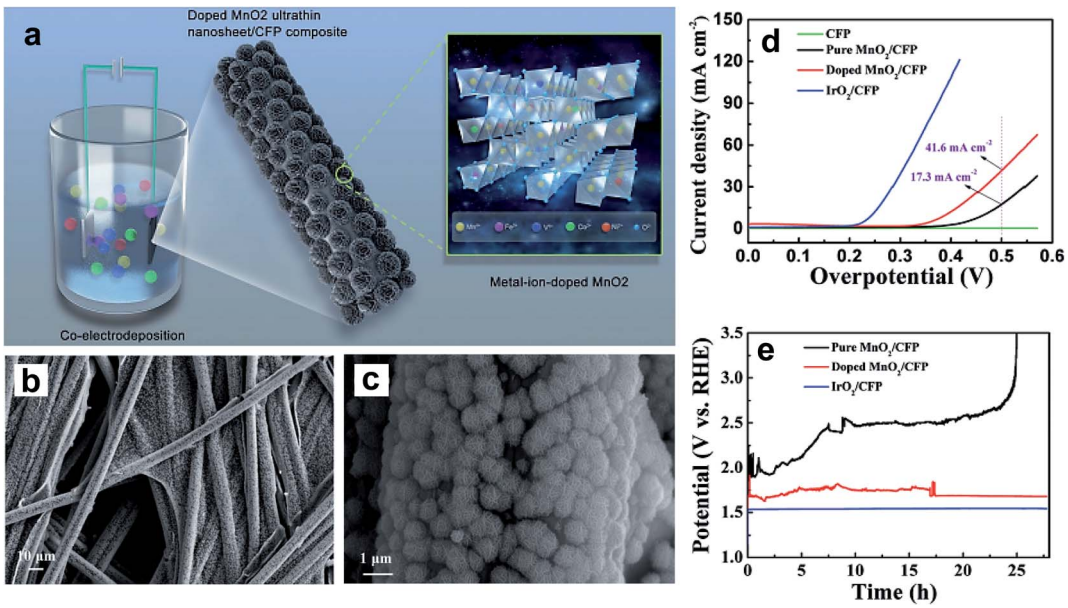

Fig. 12 (a) Schematic representation for the preparation of the metal-ion (Fe, V, Co, and Ni)-doped MnO_2 ultrathin nanosheet/CFP composite; (b and c) FESEM images showing the morphology of the metal-ion-doped MnO_2 ultrathin nanosheet/CFP composite electrode at different magnifications; (d) LSV curves of the CFP, the metal-ion-doped MnO_2 ultrathin nanosheet/CFP and the IrO_2/CFP composite electrodes measured in 1 M KOH with a scan rate of 5 mV s^{-1}, where the current is normalized by the geometrical area of the carbon fiber paper; (e) galvanostatic measurements at a current density of 20 mA cm^{-2} for the different composite electrodes.[104] Reproduced from ref. 104 with permission, © 2017 John Wiley and Sons.

doping Co^{2+} into FTO by replacing Sn^{4+} results in oxygen vacancies. The as-modified FTO electrode shows water oxidation activity at pH 7.2 with a turnover frequency of 29 000 per cobalt site, at a current density of 0.16 mA cm^{-2} during an endurance test for 2 h. Furthermore, the current density was enhanced by 5 fold by utilizing nanoporous FTO in place of planar FTO. Wang *et al.* reported Ba doping of $Y_2Ru_2O_7$ pyrochlore oxide on the yttrium position (YBRO) as an efficient catalyst for the OER in an acid electrolyte.[105] Among the doped samples, YBRO-0.15 shows superior activity, and the OER activity decreases in the following sequence: YBRO-0.15 > YBRO-0.1 > YBRO-0.25 > YBRO-0.4 > YRO > RuO_2. The enhanced activity is attributed to the oxygen vacancy-rich surface because of partial replacement of Ba^{2+} with Y^{3+} and simultaneous formation of multivalent Ru (Ru^{5+}/Ru^{4+}) species.

5. Doping non-oxide catalysts

Non-oxide catalysts include metal sulfides, metal selenides, metal phosphides, metal nitrides, and metal carbides. These catalysts are pre-catalysts, and the actual catalysts are the oxides of the corresponding cations generated on the surface during electrochemical water oxidation.

5.1 Metal sulfides

Transition metal sulfides are widely explored in electrocatalysis due to their high stability in acidic and alkaline electrolytes and abundant redox chemistry.[138] Some doped metal sulfides and their catalytic performances are listed in Table 3. Like in metal oxides and hydroxides, Fe doping is effective in significantly improving the OER activity of TM sulfides.[139,140] For example,

Table 3 Summary of representative doped metal sulfides and selenides and their catalytic performances

Catalyst	Overpotential at a specific current density	Tafel slope (mV dec^{-1})	Durability	Electrolyte
Metal sulfides				
Al-doped Ni_3S_2/NF[146]	223 mV @ 10 mA cm^{-2}	37	15 h @ 1.53 V *vs.* RHE	1 M KOH
Ce-doped Ni_3S_2 (ref. 147)	257 mV @ 50 mA cm^{-2}	81	24 h @ 0.6 V *vs.* Ag/AgCl	1 M KOH
Co-doped WS_2 (ref. 148)	303 mV @ 10 mA cm^{-2}	79	—	1 M KOH
CoFeS/CNT-P 1000 (ref. 149)	309 mV @ 100 mA cm^{-2}	47	12 h @ 20 mA cm^{-2}	1 M KOH
Fe-doped CoS[141]	290 mV @ 10 mA cm^{-2}	52.6	10 h @ 10 mA cm^{-2}	1 M KOH
Fe-doped Co_9S_8 (ref. 142)	270 mV @ 10 mA cm^{-2}	70	10 h @ 270 mV	1 M KOH
Fe-doped NiS_2 (ref. 143)	231 mV @ 100 mA cm^{-2}	43	15 h @ 20 mA cm^{-2}	1 M KOH
Fe-doped Ni_3S_2 (ref. 144)	223 mV @ 200 mA cm^{-2}	55.7	14 h @ 223 mV	1 M KOH
Fe-doped Ni_3S_2/NF[139]	249 mV @ 100 mA cm^{-2}	42	20 h @ 270 mV	1 M KOH
$Fe_{2.1\%}$ doped Ni_3S_2/NF[140]	213 mV @ 100 mA cm^{-2}	33.2	—	1 M KOH
Fe-doped H–CoMoS[145]	282 mV @ 10 mA cm^{-2}	58		1 M KOH
$Ni_{1.29}Co_{1.49}Mn_{0.22}S_4$ (ref. 150)	348 mV @ 10 mA cm^{-2}	65	40 000 s @ 10 mA cm^{-2}	1 M KOH
N-doped Co_9S_8/G[151]	409 mV @ 10 mA cm^{-2}	82.7	—	0.1 M KOH
Ni-doped FeS[152]	228 mV @ 10 mA cm^{-2}	53	10 h @ 1.47 V *vs.* RHE	1 M KOH
N_2–NiS_2-500 (ref. 153)	270 mV @ 10 mA cm^{-2}		40 h @ 270 mV	1 M KOH
(N–Ni_3S_2@C)/NF[154]	310 mV @ 100 mA cm^{-2}	75	20 h @ 1.70 V *vs.* RHE	1 M KOH
N-doped NiS/NiS_2 (ref. 155)	270 mV @ 10 mA cm^{-2}	99	20 h @ 270 mV	1 M KOH
P-doped Co–Ni–S nanosheets[156]	296 mV @ 100 mA cm^{-2}	61.1	16 h @ 10 mA cm^{-2}	1 M KOH
P–Ni_3S_2/NF[157]	256 mV @ 10 mA cm^{-2}	30	30 h @ 1.525 V *vs.* RHE	1 M KOH
P–Ni_3S_2/NF[158]	306 mV @ 100 mA cm^{-2}	99	10 h @ 1.54 V *vs.* RHE	1 M KOH
(P-(Ni,Fe)$_3S_2$/NF[159]	196 mV @ 10 mA cm^{-2}	30	15 h @ 295 mV	1 M KOH
Zn-doped Ni_3S_2 (ref. 160)	330 mV @ 100 mA cm^{-2}	87	20 h @ 300 mV	1 M KOH
Metal selenides				
Fe-doped $CoSe_2$/NF[161]	256 mV @ 100 mA cm^{-2}	35.6	10 h @ 231 mV	1 M KOH
Ag-doped $CoSe_2$ nanobelts[162]	320 mV @ 10 mA cm^{-2}	56	—	0.1 M KOH
B-doped $Fe_5Co_4Ni_{20}Se_{36}$ (ref. 163)	279.8 mV @ 10 mA cm^{-2}	59.5	10 h @ 10 mA cm^{-2}	1 M KOH
Co-doped NiSe[164]	380 mV @ 100 mA cm^{-2}	111	>10 h @ 320 mV	1 M KOH
Co-doped nickel selenide[165]	275 mV @ 30 mA cm^{-2}	63	24 h @ 1.5 V *vs.* RHE	1 M KOH
$Co_{0.75}Fe_{0.25}(S_{0.2}Se_{0.8})_2$ (ref. 166)	293 mV @ 10 mA cm^{-2}	77	—	1 M KOH
Cu-14-Co_3Se_4/GC[167]	166 mV @ 10 mA cm^{-2}	111	12 000 s @ 166 mV	1 M KOH
Cu-doped $FeSe_2$ (ref. 168)	193 mV @ 10 mA cm^{-2}	59.2	10 000 s @ 1.526 V *vs.* RHE	1 M KOH
FCS@N-CT[169]	330 mV @ 10 mA cm^{-2}	74	—	1 M KOH
Fe-doped NiSe[170]	291 mV @ 1000 mA cm^{-2}	43	22 h @ 217 mV	1 M KOH
Fe-doped $NiSe_2$ (ref. 171)	231 mV @ 10 mA cm^{-2}	83	20 h @ 15 mA cm^{-2}	1 M KOH
Fe-doped Ni_3Se_4 (ref. 172)	225 mV @ 10 mA cm^{-2}	41	26 h @ 10 mA cm^{-2}	1 M KOH
Fe-doped Ni_3Se_2 (ref. 173)	225 mV @ 10 mA cm^{-2}	35.3	12 h @ 20 mA cm^{-2}	1 M KOH
$Ni_{1.12}Fe_{0.49}Se_2$ (ref. 174)	227 mV @ 10 mA cm^{-2}	37.9	10 h @ 10 mA cm^{-2}	1 M KOH
$Ni_{0.04}Fe_{0.16}Co_{0.8}Se_2$ (ref. 175)	230 mV @ 10 mA cm^{-2}	39	15 h @ 1.5 V *vs.* RHE	1 M KOH
V_{Se}–$Ni_{0.70}Fe_{0.30}Se_2$ (ref. 176)	210 mV @ 10 mA cm^{-2}	61	20 h @ 10 mA cm^{-2}	1 M KOH
Zn-doped $CoSe_2$ (ref. 177)	286 mV @ 10 mA cm^{-2}	37	24 h @ 10, 20, and 50 mA cm^{-2}	1 M KOH

Zeng *et al.* synthesized Fe-doped CoS electrocatalysts *via* a simple hydrothermal method, and 20% Fe doping produced considerably the highest OER activity among them because of the high electrical conductivity by doping, which accelerated the charge transfer process by changing the local Co–S environment for easy adsorption of OER intermediates.[141] Dong and coworkers synthesized nano-micro spheres of Fe-doped Co_9S_8 on nickel foam using a hydrothermal method; for comparison, they also synthesized Ni-doped Co_9S_8.[142] The Fe-doped sample showed superior OER activity to the pristine and Ni-doped samples. It was found that the high activity was contributed by the synergetic effect of tuning the electronic structure of cobalt by an Fe dopant and high surface area induced by the nickel foam. Sun *et al.* synthesized Fe-doped NiS_2 nanoarrays on a Ti mesh through sulfidation of a NiFe layered hydroxide as a precursor, and they found that the catalyst with 10% Fe doping showed superior OER activity with an overpotential of 231 mV at 100 mA cm^{-2} current density.[143] Wu's group reported Fe-doped Ni_3S_2 nanowires synthesized on a Ni foam and found that Ni_3S_2 nanowires with a 13.7% dopant level of Fe exhibit superior activity and only require 223 mV overpotential to achieve 200 mA cm^{-2} in alkaline electrolyte.[144] The incorporation of iron into the matrix of Ni_3S_2 enhances the number of active site edges along with conductivity. Sugahara and coworkers prepared hollow iron-doped bimetallic CoMoS heterostructures, which show enhanced OER activity over the gold standard catalyst RuO_2.[145]

In addition to the Fe inclusion, doping other metals such as Ni,[152,178] Co,[148] Mn,[150] Zn,[160] Ce,[147] and Al[146] is also found to enhance the OER activity of metal sulfides. For instance, Lin *et al.* fabricated Ni-doped FeS nanosheets as an OER catalyst in alkaline electrolyte through a one-pot synthesis approach.[152] The Ni-doped FeS nanosheets showed significant OER activity compared to commercial IrO_2 with 228 mV overpotential at 10 mA cm^{-2} current density, by the consequent doping effect of exposing more active sites. Similarly, Kuila *et al.* synthesized binder-free self-standing Ni-doped FeS OER catalysts on Ni foam *via* an electrodeposition method.[178] The Ni doping amount is controlled by varying the electrodeposition time, and the electrode fabricated by electrodeposition at 0.9 V for 30 min shows superior activity among them. The change in the electronic structure and charge carrier density *via* the incorporation of Ni into the lattice domain of FeS significantly improves its electrocatalytic activity. Likewise, Wen and coworkers incorporated Ce into the lattice of Ni_3S_2 *via* a one-step electrodeposition method.[179] Doping with Ce preserves the original structure and morphology. Still, it promotes the OER activity by regulating the active sites and chemical states on the surface of Ni_3S_2. Yang *et al.* significantly enhanced the electrocatalytic ability of WS_2 by incorporating nearly 1% Co into its lattice.[148] The overpotential was decreased from 492 to 303 mV after incorporation of Co, and the improved activity was ascribed to the presence of Co(II/III) species that improved the binding of reactants and facilitated the formation of the *OOH intermediate. Darr and coworkers optimized the OER activity of bimetallic cobalt–nickel sulfides by doping with various TMs, such as Ag, Fe, Mn, Cr, V and Ti.[150] Among them, Mn-incorporated cobalt–nickel sulfide ($Ni_{1.29}Co_{1.49}Mn_{0.22}S_4$) shows enhanced activity through tuning of the electronic structure of the host by Mn(III) cations. Zn-doped Ni_3S_2 nanoarrays on nickel foam grown by Sun *et al.* have better OER activity than their pristine counterpart, with excellent stability for 20 h at 300 mV overpotential.[160] The extended endurance and comparable activity were caused by modulation of the electronic structure of the Ni_3S_2 catalyst through Zn incorporation.

Recently, researchers reported incorporating non-metals, such as N, P, and F, into the lattice of metal sulfides to improve their electrocatalytic capability.[149,151,153–159,180] N doping of a NiS_2 catalyst using $NH_3 \cdot H_2O$ as a precursor considerably increased its water oxidation ability by overcoming the intrinsic limits of reaction kinetics through optimizing d-states.[153] 3D N-doped Ni_3S_2 nanoflakes grown on Ni foam show superior durability for 20 h at 1.7 V with ~93% retention of their initial activity.[154] The experimental results indicate that N doping plays a key role in the quick discharging of OER intermediates and improved intrinsic activity.[155] Dou *et al.* found that a Co_9S_8/graphene hybrid, doped with N using NH_3 plasma etching, showed a significant improvement in its OER performance compared with a pristine sample.[151] The synergetic effect of N-doping and surface etching considerably tuned the electronic structure of the Co_9S_8/graphene hybrid and thus enhanced the number of active sites on the surface. He *et al.* synthesized 3D self-supported and P-doped Ni_3S_2 on Ni foam by a one-step hydrothermal process by simultaneous phosphorization and sulfuration.[157] The as-fabricated electrode exhibits enhanced OER activity with an overpotential of 256 mV at 10 mA cm^{-2}. The inclusion of P anions optimizes the electronic structure and provides facile adsorption of reactants and thus enables a faster mass transfer. Similarly, P-doped bimetallic nickel–iron sulfide nanosheets on Ni foam were synthesized *via* a one-pot process.[159] The incorporated P considerably enhances the electrochemical surface area and electrical conductivity by optimizing the adsorption of OER intermediates. F-doped CoS_2 on Ni foam was synthesized using NH_4F as a fluorine source by a hydrothermal process.[180] The F dopant significantly enhances the wettability of the catalyst, and thus facilitates the maximum interaction with electrolyte in both alkaline and neutral media.

5.2 Metal selenides

Some doped metal selenides and their performances are listed in Table 3. The electrocatalytic behavior of metal selenides depends on the number of exposed edge sites.[21] Edge sites are step-like apertures or defects generated at the basal plane because of doping.[181] Besides the edge sites, the electrical conductivity and intrinsic activity of metal selenides are enhanced by doping; specifically, doping with TMs significantly improves the OER activity of metal selenides.[169,171,173,174] For example, Zare *et al.* designed a self-supported electrocatalyst on Ni foam by doping Fe into the lattice domain of $CoSe_2$, which only requires 256 mV overpotential to attain 100 mA cm^{-2} current density.[161] Here, Fe improves the intrinsic electrical conductivity, and thus lowers the energy barrier for the OER. Zhao and coworkers improved the OER activity of $CoSe_2$

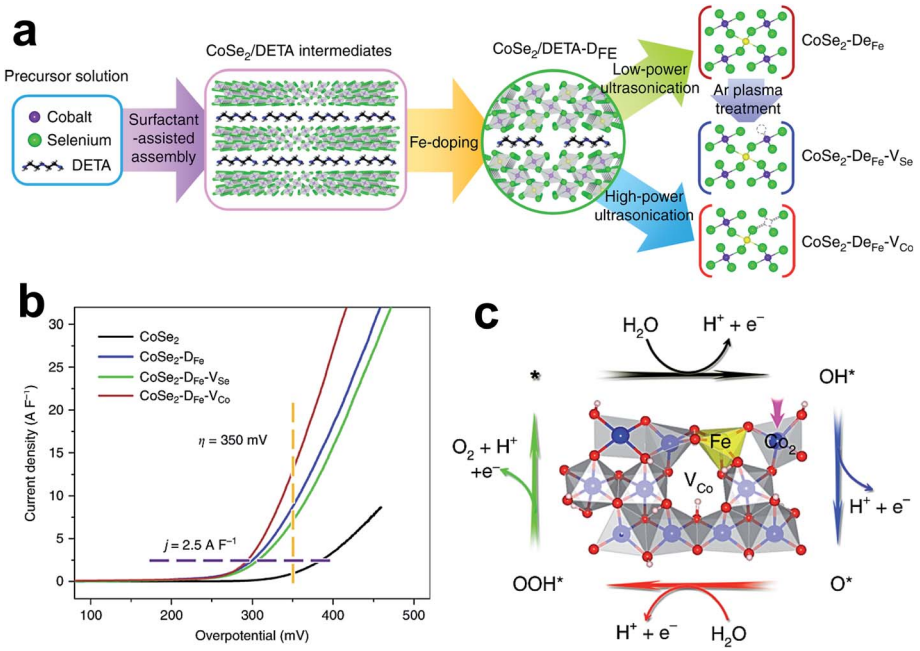

Fig. 13 (a) Schematic illustration of the synthetic methods for different catalysts; (b) LSV curves normalized by electrochemical double-layer capacitance; and (c) crystal structure of FeCoOOH-V_{Co} and the oxygen evolution reaction pathway on the (01–12) facets.[182] Reproduced with open access.

nanobelts by simultaneous Fe doping and Co vacancy creation, as shown in Fig. 13a.[182] LSV curves of $CoSe_2$, $CoSe_2$-D_{Fe}, $CoSe_2$-D_{Fe}-V_{Se}, and $CoSe_2$-D_{Fe}-V_{Co} catalysts, normalized by electrochemical double-layer capacitance, are shown in Fig. 13b, and suggest that $CoSe_2$-D_{Fe}-V_{Co} has superior OER activity among the catalysts. Fig. 13c displays the FeCoOOH with Co vacancies and the OER mechanism occurring on its surface, which involves three OER intermediates (*OH, O*, and *OOH) and four proton-coupled electron transfer steps. The Gibbs free energy profiles of this catalyst show different catalytic mechanisms for Co and Fe sites. The transformation of OH* to O* potentially limits the activity of Co active sites owing to the large Gibbs free energy difference (ΔG_2). In contrast, the conversion of O* to *OOH is the RDS (ΔG_3) in case of Fe sites, due to the high free energy difference. Theoretical simulations identified that the cobalt dimer (Co_2) is the most active site for the OER, and is present adjacent to the Co vacancy near the surface Fe site. The combinatorial effect of Co vacancy and Fe doping significantly intensifies the OER performance by reducing the peak intensity near the Fermi level, so the binding of *OH with active sites is weakened. Zou *et al.* found that the minimal amount of Fe (7.4%) inclusion into the NiSe nanorod/nanosheet lattice significantly improved its OER activity.[170] The Fe-doped NiSe only required 291 mV overpotential to achieve 1000 mA cm^{-2} current density. This superior activity is accredited to the increased electrical conductivity, active sites, and mass transfer. Xu *et al.* fabricated hierarchical Fe-doped Ni_3Se_4 on Ni foam using a hydrothermal method, and NiFe LDH was used as a precursor material.[172] The doped sample shows superior OER activity than IrO_2 and pristine catalysts, because of its higher electrical conductivity. Mohanty *et al.* reported an increase in OER activity of nickel selenide, owing to the synergetic effect of Fe doping along with the creation of Se vacancies by chemical reduction with $NaBH_4$.[176] Computational studies suggest an increase in DOS near the Fermi level because of Fe doping and Se vacancies, which helps in decreasing the energy barrier for OER intermediates.

Besides Fe, Co was also used as a dopant to improve the OER performance of nickel selenides,[165] and Co-doped NiSe nanoflowers grown on Ni foam exhibited considerable activity compared to their pristine counterpart. Here, Co doping generates more OER active sites *via* tuning the electronic structure of NiSe. Wang *et al.* showed MOF-derived Co-doped nickel selenide on Ni foam and analyzed its OER activity in alkaline electrolyte.[164] The as-designed catalyst exhibits an overpotential of 275 mV at 30 mA cm^{-2}, and the high activity is ascribed to an increase in electrical conductivity because of Co doping. Zhang *et al.* co-doped Ni and Fe into the matrix of $CoSe_2$, and noticed that the catalyst with a stoichiometric formula of $Ni_{0.04}Fe_{0.16}Co_{0.8}Se_2$ has remarkable OER activity among the prepared catalysts.[175] Ni doping does not alter the OER mechanism but reduces the energy barrier for the RDS and keeps Co-active sites intact, and Fe doping improves the charge transfer kinetics by transferring the active sites from Co to Fe. $FeSe_2$ was doped with various transition elements (Co, Ni, Mn, and Cu) by Wei *et al.*[168] Among these dopants, Cu is found to be more effective and shows enhanced OER activity. The theoretical and experimental results reveal that Cu doping optimizes the electronic structure of the $FeSe_2$ lattice to enable faster electron transfer and thus boosts the reaction kinetics of the OER. In cobalt selenide, the Cu doping results in a phase transformation from orthorhombic $CoSe_2$ to monoclinic

Co_3Se_4, causing improved OER performance of cobalt selenide.[167] The electronic structure change in cobalt selenide by Cu doping is evident from X-ray photoelectron spectroscopy and theoretical simulations. DFT calculations further reveal that because of structural transformation from orthorhombic $CoSe_2$ to monoclinic Co_3Se_4, and the Gibbs free energy for the RDS was drastically decreased from 2.64 to 1.90 eV.

The minimal amount of Ag (1%) doping into the lattice domain of $CoSe_2$ nanobelts significantly increases its electrical conductivity without much loss of active sites (Co).[162] Ag-doped $CoSe_2$ nanobelts exhibit high OER activity relative to pristine $CoSe_2$ nanobelts, because of high electrical conductivity and active site retention. Incorporation of low-valence Zn into the $CoSe_2$ lattice domain triggers subtle changes in the lattice and increases the number of active sites for the OER.[177] Theoretical simulations suggest that Zn inclusion decreases the kinetic energy barrier for the adsorption of OER intermediates by encouraging adsorption on Co sites and neighboring Zn sites. Boron doping into the lattice of ternary pyrite selenide ($Fe_5Co_4Ni_{20}Se_{36}$) decreased its overpotential from 543 to 279.8 mV at 10 mA cm^{-2}, with the Tafel slope lowered from 161 to 59.5 mV dec^{-1}.[163] Fig. 14a and b show the schematic representation of $NiSe_2$ and $Fe_5Co_4Ni_{20}Se_{36}B_x$ crystal structures, and the doped B atoms are incorporated into the interstitial positions and some B atoms even bond with metals (Ni, Co, and Fe). The proposed OER mechanisms on pristine and doped pyrite are shown in Fig. 14c and d, and reveal that B doping facilitates an easy discharge of *OOH from the active sites, as a consequence of lower Gibbs free energy. The PDOS reveals that B doping significantly reduces the total d electrons around metals, enhancing the interaction between them and thus weakening the bond between *OOH and active sites. Recently, anion doping, *i.e.*, doping on the Se site, was also found to be beneficial in enhancing the OER activity. For example, Xu *et al.* reported doping of sulfur on the Se site, enhancing the OER activity of bimetallic cobalt iron selenide $Co_{0.75}Fe_{0.25}(S_{0.2}Se_{0.8})_2$ as compared to non-doped $Co_{0.75}Fe_{0.25}S_2$ and $Co_{0.75}Fe_{0.25}Se_2$, since charge transfer and electrochemical surface area were increased by doping.[166]

5.3 Metal phosphides

In the past five years, metal phosphides have emerged as one of the most promising types of catalyst for water oxidation, even though the first metal phosphide catalyst was reported as early as in 1990.[183] Some doped metal phosphides and their performances are listed in Table 4. Incorporation of a second element into the matrix of a metal phosphide could enhance the OER performance, in terms of both activity and stability.[184,185] For instance, Chen *et al.* doped Fe into the matrix of CoP ultrathin nanosheets grown on Ni foam, which exhibited a very low overpotential of 67 mV at 10 mA cm^{-2} in 1 M KOH.[186] The excellent OER activity is attributed to the interference of Fe/Co/Ni in the low current density region. Post OER characterization revealed the complete absence of P because of the formation of CoOOH active species during the OER. Baek and coworkers synthesized Fe-doped porous CoP polyhedrons from MOFs by varying the Fe/Co ratio.[187] Among them, $Co_{0.68}Fe_{0.32}P$ had better OER activity over its pristine counterparts, *i.e.*, CoP and FeP. Fe doping accelerated the discharge of OER intermediates by optimizing their adsorption energy and stabilized the P species during contact with air. Peng's group initially conducted theoretical simulations to predict the Fe influence on the water oxidation capability of Ni_2P by constructing partially oxidized

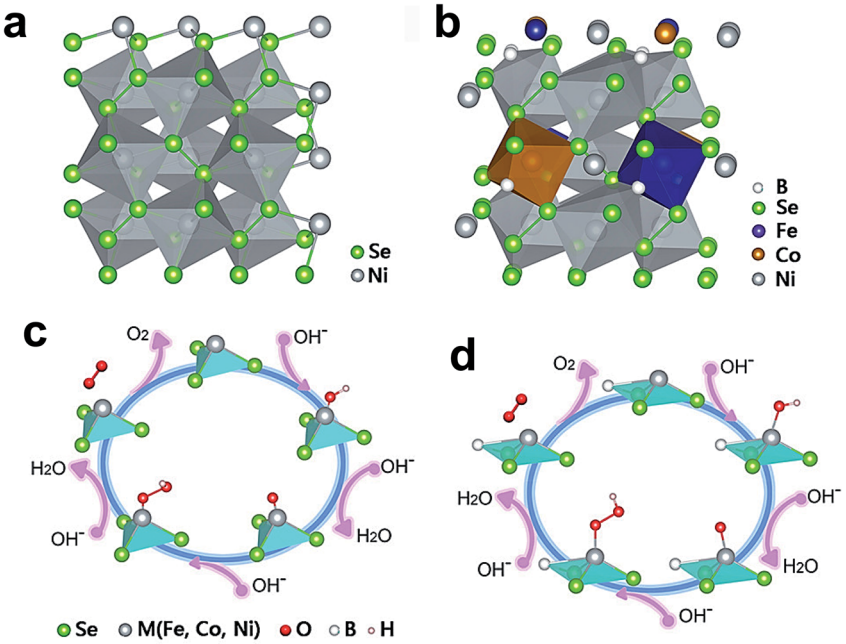

Fig. 14 (a and b) Schematic illustration of $NiSe_2$ and $Fe_5Co_4Ni_{20}Se_{36}B_x$ crystal structures, and (c and d) proposed OER mechanisms for pyrite selenides before and after B dopant incorporation.[163] Reproduced from ref. 163 with permission, © 2019 American Chemical Society.

Table 4 Summary of representative doped phosphides, nitrides, and carbides and their catalytic performances

Catalyst	Overpotential at a specific current density	Tafel slope (mV dec^{-1})	Durability	Electrolyte
Metal phosphides				
Al-doped CoP[193]	360 mV @ 200 mA cm^{-2}	38	150 h @ 10 mA cm^{-2}	1 M KOH
$Co_{0.68}Fe_{0.32}P$[187]	289 mV @ 50 mA cm^{-2}	64	3600 s @ 10 mA cm^{-2}	1 M KOH
$Fe_{0.27}Co_{0.73}P/NF$[184]	251 mV @ 10 mA cm^{-2}	59.1	40 h @ 40 mA cm^{-2}	1 M KOH
Fe-doped CoP[186]	166 mV @ 50 mA cm^{-2}	65.82	50 h @ 50 mA cm^{-2}	1 M KOH
Fe-doped Ni_2P[192]	330 mV @ 20 mA cm^{-2}	39	10 h @ 20 mA cm^{-2}	1 M KOH
Fe-doped Ni_2P[188]	300 mV @ 1000 mA cm^{-2}	52	—	1 M KOH
$Fe_xV_{y-x}PC/NF$[189]	201 mV @ 10 mA cm^{-2}	75	24 h @ 10 mA cm^{-2}	1 M KOH
Mn-doped CoP[194]	261 mV @ 10 mA cm^{-2}	44.9	24 h @ 10 mA cm^{-2}	1 M KOH
Mn-doped Ni_2P[195]	330 mV @ 100 mA cm^{-2}	116.7	18 h @ 320 mV	1 M KOH
NiCoFeP/NF[191]	271 mV @ 200 mA cm^{-2}	45	10 h @ 1.485 V *vs.* RHE	1 M KOH
$NiCoFe_xP/CC$[190]	275 mV @ 50 mA cm^{-2}	50	150 h @ 1.70 V *vs.* RHE	1 M KOH
NCNP[196]	229 mV @ 10 mA cm^{-2}	78.6	100 h @ 100 mA cm^{-2}	1 M KOH
$Ni_{1.85}Fe_{0.15}P$ NSAs/NF[185]	270 mV @ 20 mA cm^{-2}	96	10 h @ 330 mV	1 M KOH
Ni_2P/(NiFe)2P(O) NAs[197]	530 mV @ 800 mA cm^{-2}	60	100 h @ 500 mV	1 M KOH
N-NiVFeP/NFF[198]	229 mV @ 10 mA cm^{-2}	78.6	100 h @ 100 mA cm^{-2}	1 M KOH
O-doped Co_2P/CuO NWs/CF P[199]	270 mV @ 10 mA cm^{-2}	74.4	30 h @ 10 mA cm^{-2}	1 M KOH
S-doped CoP/NF[200]	300 mV @ 10 mA cm^{-2}	82	20 h @ 350 mV	1 M KOH
Metal nitrides				
Co-doped MoNi nitride[201]	294 mV @ 10 mA cm^{-2}	73	10 h @ 317 mV	0.1 M KOH
Fe-doped cobalt nitride[202]	200 mV @ 10 mA cm^{-2}	42.44	10 h @ 200 mV	1 M KOH
$Mn_{0.15}$ $Co_{0.85}N$[203]	265 mV @ 10 mA cm^{-2}	48	30 h @ 280 mV	1 M KOH
$Mn_{0.15}$ $Co_{0.85}N$[203]	285 mV @ 10 mA cm^{-2}	64	30 h @ 285 mV	1 M phosphate-buffered saline
P,F-$Ni_{1.5}Co_{1.5}N$[204]	350 mV @ 100 mA cm^{-2}	66.1	—	1 M KOH
P-$NiMo_4N_5$@Ni[205]	435 mV @ 100 mA cm^{-2}	65	24 h @ 50 mV	1 M KOH
Metal carbides				
B, N:Mo_2C@BCN[206]	360 mV @ 100 mA cm^{-2}	61	20 h @ 350 mV	1 M KOH
Co_3C-NB[207]	354 mV @ 10 mA cm^{-2}	90	24 h @ 50 mA cm^{-2}	0.1 M KOH
Co-doped β-Mo_2C[208]	262.2 mV @ 10 mA cm^{-2}	28.8	16 h @ 1.49 V *vs.* RHE	1 M KOH
Co-doped Ni_3C/Ni@C[209]	325 mV @ 10 mA cm^{-2}	67.76	100 000 s @ 10 mA cm^{-2}	1 M KOH
FCC@CNOs/NF[210]	271 mV @ 10 mA cm^{-2}	48.9	40 h @ 100 mA cm^{-2}	1 M KOH
Fe-doped Ni_3C[211]	275 mV @ 10 mA cm^{-2}	62	10 h @ 1.5 V *vs.* RHE	1 M KOH
$V_{0.28}Co_{2.72}C$/CNFs[212]	210 mV @ 10 mA cm^{-2}	147	10 h @ 1.4 V *vs.* RHE	1 M KOH

surfaces of Ni (111), Ni_2P (111), and Fe-doped Ni_2P (111) models.[188] The Gibbs free energy studies reveal that the Fe-doped sample requires an energy 0.14 eV lower than that of Ni_2P for the RDS (O* to *OOH). Experimental results were in accordance with the theoretical calculations, and they observed the formation of Fe, P co-doped γ-NiOOH during the electrochemical water oxidation reaction from the Fe-doped Ni_2P. Fe, P co-doped γ-NiOOH is a good catalyst for improved OER activity, and Fe doping primarily enhances the active sites for the OER. Xiang *et al.* tuned the electronic structure of vanadium phosphide by including Fe into its lattice domain, which demonstrated remarkable OER activity.[189] Among all the samples, the sample with a 1 : 3 ratio of Fe/V has the highest activity. XPS analysis identifies increased valency of V because of the incorporation of Fe, which optimizes the adsorption of *OH on active sites. Fe doping of bimetallic phosphides was also found to significantly contribute to improving electrochemical water oxidation.

Like monometallic phosphides, bimetallic phosphides can also convert into their respective oxyhydroxides at high anodic potentials. Fe-doped NiCoP converts into Fe-doped NiOOH and CoOOH, and Fe doping improves the OER activity by accelerating the discharge of OER intermediates.[190,191] Simultaneously, the conductive metallic phosphide support improves OER kinetics by promoting the proton transfer. Tsang and coworkers studied the comparative doping effects of TMs (Co, Fe, Mn, and Mo) on the OER activity of NiP.[192] Among them, the Fe doped sample was found to have more prominent activity since Fe is able to tune the electronic structure of Ni to interact optimally with OER intermediates.

Mn doping of cobalt phosphide and nickel phosphide improves their catalytic activity for electrochemical water oxidation. In cobalt phosphide, Mn doping enhances the electrochemical surface area by increasing the number of exposed active sites.[194] The optimal Mn/Ni ratio of 0.053 is found to provide superior activity, as the Ni_2P electronic structure is optimized.[195] Al doping was also used to enhance the electrochemical surface area of cobalt phosphide by dissolution during the OER. Al-doped cobalt phosphide shows a fourfold increase in electrochemical surface area compared to the pristine sample by the formation of Al/Co spinel oxide and partial leaching of Al.[193]

Along with doping of metals, doping of non-metals such as N, O, and S can also enhance the electrocatalytic activity of phosphide catalysts for the OER.[196,198–200] N doping in the anionic site (P) of NiCoP improved its OER performance, with better activity compared to NiCoP and NiCoN. The high activity was induced by the formation of abundant oxygen vacancies, improving the charge transfer during oxygen generation.[196] Likewise, oxygen and sulfur were also doped on the anionic sites to increase the OER activity of metallic phosphides. Oxygen doping of cobalt phosphide generates abundant defects and electroactive sites on the surface by optimizing the adsorption energy of reactants.[199] In the case of bimetallic nickel–iron phosphide, the OER activity is enhanced by oxygen doping on account of an efficient decrease in the energy barrier of OER intermediates and products.[197] Electronegative sulfur doping in the anionic site of cobalt phosphide significantly improved its OER activity, owing to the tuning of the electronic structure and increased number of active sites.[200]

5.4 Metal nitrides and carbides

Metal nitrides belong to an interstitial compound family, which contains nitrogen atoms on the interstitial sites of parent compounds. The presence of N atoms on the interstitial sites increases the distance between metal atoms; thus, it tunes the d band structure.[20] Some doped metal nitrides and carbides and their performances are listed in Table 4. Recent studies on the electrochemical activity of metal nitrides suggest that they are highly active for the OER owing to their high electrical conductivity.[204,205] However, the OER activity and stability were further improved by tuning their electronic structure by doping with TMs and non-metals. For instance, Mn-doped CoN nanowires grown on carbon cloth exhibit good OER activity in alkaline and neutral electrolytes.[203] Among the doped catalysts, $Mn_{0.15}Co_{0.85}N$ shows superior activity, and Mn doping considerably increases the charge transfer kinetics and facilitates the optimized discharge of OER intermediates. Zhou *et al.* investigated the doping effect of various metal atoms, such as Zn, Ni, Fe, and Mn, on the OER activity of cobalt nitride nanosheets.[202] The Fe doped one has better OER activity, and XPS analysis suggests more Co^{4+} OER active species because of the doping effect of Lewis acid Fe^{3+}.

Cobalt doping into the lattice of bimetallic MoNi nitride nanowires shows a considerable increase in their OER activity by reduced charge transfer resistance and augmentation of the electrochemically active surface area.[201] The dual modulation in the electronic structure of Mo and Ni was induced by cobalt doping that improved the electrical conductivity for highly active OER sites. Liang *et al.* theoretically studied the doping effect of first-row TMs (Sc to Zn) for improving the OER activity of Al/GaN.[213] The inclusion of transition metals from Sc to Fe resulted in low OER activity because they bonded to OER intermediates too firmly and resulted in high overpotentials. Meanwhile, Cu and Zn also displayed no or low OER activity, as they attached to the intermediates very weakly. Only Ni doping had significant OER activity because it could switch from a high spin state to a low spin state and stabilized the OOH adsorbate. Tong and coworkers synthesized P and Co dual-doped vanadium nitride nanowires using a combined hydrothermal and annealing approach.[214] The dual-doped vanadium nitrate catalyst showed better activity and durability for the OER, compared to the single-doped or pristine sample, or IrO_2. Dual doping of Co and P synergistically tunes the number of active sites on the catalyst surface by moving the d states of vanadium closer to the Fermi level.

Zhang and coworkers demonstrated an increase in the OER performance of bi-metallic nitrides by co-doping with phosphorus and fluorine.[204] Fig. 15a shows the schematic representation of the fabrication process for P and F co-doped nickel–cobalt nitride ($PF/Ni_{1.5}Co_{1.5}N$) nanorods using an ionic liquid. The $PF/Ni_{1.5}Co_{1.5}N$ prepared without using any ionic liquid results in a lamellar structure, as displayed in Fig. 15b. The SEM and elemental mapping analysis results of $PF/Ni_{1.5}Co_{1.5}N$ nanorods are presented in Fig. 15c and d, which indicates the uniform distribution of N and F dopants all over the catalyst. Fig. 15e and f show the IR uncompensated LSV curves and comparison of η_{10} values (potentials required to reach 10 mA cm^{-2}) for $PF/Co_xNi_{3-x}N$ catalysts. Electrochemical studies reveal that the $PF/Ni_{1.5}Co_{1.5}N$ catalyst shows augmented OER activity as well as facile reaction kinetics among the prepared catalysts. DFT calculations suggest that co-doping of P and F atoms into the lattice of the $Ni_{1.5}Co_{1.5}N$ catalyst considerably decreases the free energy barrier for OER intermediates, thus helps in improving the electrocatalytic performance.

Recently, researchers found that metal carbides, specifically transition metal carbides, can be applied as electrocatalysts for the OER owing to their high stability.[215] Some doped metal carbides and their performances are listed in Table 4. The activity of TM carbides was improved by including one or more foreign dopants into their lattice domain. Yan *et al.* improved the OER activity of Ni_3C by doping 2% atomic iron, which yields an overpotential of 275 mV at 10 mA cm^{-2}.[211] The optimized doping of Fe tuned the electronic structure of Ni and thus improved the number of active sites on the surface. Similarly, Jia *et al.* tuned the water oxidation ability of Ni_3C *via* incorporation of a small amount of Co into it using a MOF-derived method.[209] The as-fabricated catalyst had better activity than the IrO_2 catalyst in the alkaline electrolyte, and the improved activity was associated with the active surface sites through optimization of electronic properties. In general, the Mo_2C catalyst is inactive for the OER, but doping 10% cobalt into the Mo_2C catalyst was found to increase its OER performance through significant enhancement in the density of active sites of the catalyst.[208] Zhao *et al.* optimized the electronic structure of Co_3C by doping with low electronegativity vanadium element.[212] Specifically, $V_{0.28}Co_{2.72}C$ shows superior activity by forming local negative Co centers through the intake of electrons from vanadium dopants. Xu *et al.* doped TMs such as Mn, Co, and Ni into the matrix of Fe_3C and evaluated its OER performance.[210] They noticed that Co-doped iron carbide had enhanced activity, and the Gibbs free energy was estimated in the different steps in the OER process. The free energy profiles of the Co and Fe sites were compared, and the Gibbs free energy required for the Co site (2.35 eV) was lower than that for the Fe site (2.75 eV), for the

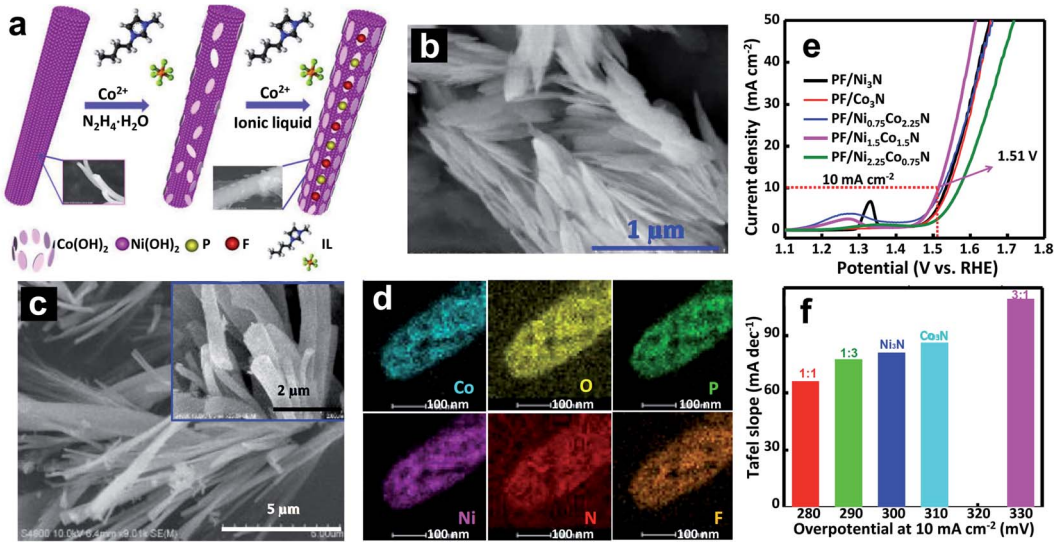

Fig. 15 (a) Schematic illustration of the fabrication processes for PF/$Ni_{1.5}Co_{1.5}N$ nanorods; (b) SEM; (c) highly magnified SEM; (d) HAADF-STEM elemental mapping results of the heteroatom doped Ni–Co (1 : 1) precursor; (e) LSV curves of PF/$Co_xNi_{3-x}N$ catalysts for the OER (400 mg of ionic liquid, without IR compensation); and (f) comparison of η_{10} values (potentials required to reach 10 mA cm^{-2}) for various catalysts (Ni : Co = 1 : 1, 1 : 3, 1 : 0, 0 : 1, and 3 : 1).[204] Reproduced from ref. 204 with permission, © 2017 John Wiley and Sons.

conversion of *O to *OOH (RDS). From the comparison, Fe has a stronger affinity towards *O compared to Co, hence doping of Co into the Fe_3C facilitates the discharge of intermediates, thus lowering the potential.

Doping of metal carbides on the anionic site also improves their activity for electrocatalytic oxygen evolution. Generally, WC is a poor OER catalyst; however, when the carbon site is doped with nitrogen, it shows even better OER performance than IrO_2 in an acid electrolyte.[216] The N doping helps in accelerating the discharge of intermediates and thus improves activity, but its poor stability is still a concern. Dual doping of N and B on the anionic site of Co_3C considerably increases its water oxidation ability compared to the pristine or single-doped sample, or IrO_2. The synergetic effect of N and B dopants improves both activity and stability by boosting the charge transfer kinetics of intermediates.[207] Likewise, Lee and coworkers synthesized dual-doped N and B into the matrix of Mo_2C embedded in the B, N doped carbon network (B,N:Mo_2C@BCN), which shows a considerable increase in OER activity compared to the mono-doped or pristine sample, or IrO_2.[206] The significant improvement in electrocatalytic performance is accredited to the formation of active B- and N-doped molybdenum oxide at high anodic potentials.

6. Tuning carbon-based catalysts

Although metal-based catalysts are employed in electrocatalytic OER applications widely because of their promising capabilities to deliver efficient catalytic activity by variable oxidation states,[217] these catalysts suffer from relatively poor endurance, low selectivity, susceptibility towards potential gas poisoning, and hazardous environmental effects. In 2009, the first carbon-based catalyst was reported by Dai's group in fuel cells as an alternative to the platinum catalyst.[218] Since then, carbon-based catalysts, particularly those doped with various heteroatoms or metals, have received extensive attention and tremendous progress has been made in electrocatalysis.[219,220] Table 5 provides a summary of some representative doped carbon-based electrocatalysts and their catalytic performances.

6.1 Graphene

Graphene is a thin layer of single atoms packed with sp^2 hybridized carbon atoms in a hexagonal lattice. It is considered either a zero-bandgap semiconductor or conductor because of its symmetric band structure.[244] Hence, pristine graphene shows low or no catalytic activity; however, the unique structural flexibility of graphene allows extensive functionalization *via* doping to improve catalytic activity. The dopants could interrupt the sp^2 hybridized network and induce the formation of sp^3 in the lattice, resulting in an electronic density change that imparts catalytic activity to it.[244] For instance, doping of N into the lattice of graphene disrupts the charge distribution and spin density of neighboring carbon atoms and, consequently, imparts OER activity. Yang *et al.* conducted a study to gain mechanistic insights into N-doped graphene in the OER.[230] They identified the formation of electron-withdrawing pyridinic N functionalities, which is the key reason for the superior OER performance of N-doped graphene. Xia's group studied the active sites in N-doped graphene nanoribbons combined with other dopants, such as B, Cl, P, and S, using DFT calculations.[245] Gibbs free energy analysis for the OER on doped graphene nanoribbons suggests that the conversion of *O to *OOH is the RDS. The co-doping shows better activity than mono-doping, and the synergetic effect of co-doping is mostly related to the distance between them. In another report, N doping was done by using polyaniline and graphene oxide as precursors, which

Table 5 Summary of representative doped carbon-based electrocatalysts and their catalytic performances

Catalyst	Overpotential at a specific current density	Tafel slope (mV dec^{-1})	Durability	Electrolyte
20-NMWNT[221]	320 mV @ 10 mA cm^{-2}	68	—	1 M NaOH
B, N-carbon[222]	340 mV @ 10 mA cm^{-2}	84	—	1 M KOH
Co-C_3N_4/CNT[223]	380 mV @ 10 mA cm^{-2}	68.4	—	1 M KOH
Co-N/GF[224]	313 mV @ 10 mA cm^{-2}	84.1	30 h @ 1.6 V *vs.* RHE	1 M KOH
Co-TA[225]	460 mV @ 10 mA cm^{-2}	66	—	0.1 M KOH
GO-PANi31-FP[226]	300 mV @ 10 mA cm^{-2}	136	—	0.1 M KOH
N/C[227]	380 mV @ 10 mA cm^{-2}	—	—	0.1 M KOH
NCHCs[228]	290 mV onset potential	90	12 h @ 1.6 V *vs.* RHE	0.1 M KOH
NCNTFs[229]	370 mV @ 10 mA cm^{-2}	93	10 000 s @ 1.70 V *vs.* RHE	1 M KOH
N-GRW[230]	360 mV @ 10 mA cm^{-2}	47	24 h @ 10 mA cm^{-2}	1 M KOH
N-HC@G-900 (ref. 231)	350 mV @ 10 mA cm^{-2}	88.1	25 000 s @ 10 mA cm^{-2}	1 M KOH
N-HC@G-900 (ref. 231)	350 mV @ 10 mA cm^{-2}	297.5	7500 s @ 1 mA cm^{-2}	0.5 M H_2SO_4
NiFe@g-C_3N_4/CNT[232]	326 mV @ 10 mA cm^{-2}	67	16 h @ 10 mA cm^{-2}	1 M KOH
Ni, Fe@PCN[233]	310 mV @ 10 mA cm^{-2}	38	2 h @ 1.53 V *vs.* RHE	1 M KOH
Ni, N doped graphene[234]	270 mV @ 10 mA cm^{-2}	59	40 h @ 1.40 V *vs.* RHE	1 M KOH
Ni-O-G SACs[235]	224 mV @ 10 mA cm^{-2}	42	50 h @ 115 mA cm^{-2}	1 M KOH
N, S-CNT[236]	360 mV @ 10 mA cm^{-2}	56	—	1 M KOH
N, S doped graphene[237]	310 mV @ 10 mA cm^{-2}	65	25 h @ 1.55 V *vs.* RHE	0.1 M KOH
O-CNTs[238]	360 mV @ 10 mA cm^{-2}	47.7	24 h @ 5 mA cm^{-2}	1 M KOH
O Doped MWCNTs[239]	450 mV @ 10 mA cm^{-2}	72	10 000 s @ 5 mA cm^{-2}	0.1 M KOH
P-doped C_3N_4 (ref. 240)	400 mV @ 10 mA cm^{-2}	61.6	15 h @ 10 mA cm^{-2}	0.1 M KOH
P-doped graphene[241]	330 mV @ 10 mA cm^{-2}	62	—	1 M KOH
S, N-Fe/N/C-CNT[242]	370 mV @ 10 mA cm^{-2}	82	40 000 s @ 10 mA cm^{-2}	0.1 M KOH
S,S′-CNT[243]	350 mV @ 10 mA cm^{-2}	95	75 h @ 10 mA cm^{-2}	1 M KOH

produced nanoporous layered and N-doped graphene that exhibits enhanced OER activity.[246] Nearly 51% quaternary N plays a significant role in the considerable increase in OER activity. Wang *et al.* demonstrated a significant improvement in the OER performance of graphene by P doping.[241] They found that the stronger oxygen adsorbing ability of P, which was present at the edges of graphene, played a crucial part in stabilizing OER intermediates.

Besides single atom doping of graphene, dual- and multi-atom doping were also found to deliver significant results in improving OER activity by their synergistic effects. Zhao and Xia studied several combinations of dual doping such as N–N, N–P, N–S, N–B, and N–Cl in optimizing the OER activity of graphene using first-principles modeling.[247] They suggested that optimizing the distance between dopants, selecting the right combination of dopants, and efficient utilization of edge effect are the vital factors in designing a highly efficient electrocatalyst. For example, the co-doping of P and N into the graphene lattice results in graphene formation with P, N population at the edges, as a consequence of the large atomic size of P that always moves away from the planar surface. This co-doped catalyst exhibits a significant improvement in OER performance, and the elevated activity is attributed to the synergetic effect of both dopants, the high oxidation ability of the P-site that initially adsorbs O_2, and the N-site that stabilizes the OER intermediates and promotes desorption.[248]

Qiao's group synthesized N and S dual-doped graphene microwires using an ionic liquid assisted method, which showed an overpotential of 310 mV at 10 mA cm^{-2}, stability for 25 h and 95% faradaic efficiency.[237] Moreover, this electrode was employed as an efficient cathode for Zn–air batteries, and this superior OER activity is attributed to the numerous active sites created by C–N–S spin density. Furthermore, Zhang and Dai demonstrated tri-doping of graphene with N, P and F atoms, yielding a multifunctional electrocatalyst.[226] The N and P doping roles in improving OER performance were elaborated. Still, it is inconclusive how F inclusion into the graphene lattice contributes to the electrocatalytic activity. Li *et al.* demonstrated a significant improvement of the OER performance of graphene by including single nickel atoms.[235] The single-atom doped graphene displayed 50 h of long-term stability at a very high current density of 115 mA cm^{-2}. This unusual activity is accredited to the bonding between single nickel atoms and oxygen sites of graphene. Chen *et al.* doped Ni single atoms on N-doped nano-porous graphene *via* a chemical vapor deposition (CVD) method, followed by chemical etching.[234] The dual-doped catalyst showed superior OER activity to other catalysts, and even outperformed the IrO_2 catalyst. The DFT calculations suggest that Ni, N co-doping significantly decreased the stability difference between O* and *OH intermediates by 0.3 eV.

6.2 Carbon nanotubes (CNTs)

CNTs are 1D structural allotropes of carbon that consist of hexagons of carbons arranged in a concentric fashion. CNTs possess good electrical–thermal properties due to their unique hollow geometry and conjugated long-range π electron structure.[249] However, CNTs in their pristine form exhibit poor electrocatalytic properties. To improve the electrocatalytic properties, CNTs need to be functionalized with several dopants.[250] This functionalization can be done through two

methodologies, *i.e.*, covalent and non-covalent methods. The covalent functionalization proceeds *via* forming a covalent bond between the functional group and CNTs, which could disrupt the unique structure of CNTs. In the non-covalent method, the functionalization happens through physical processes such as electrostatic, hydrogen bonding, π stacking and van der Waals interactions, which leaves the CNT structure undisturbed.[249] For example, Tian *et al.* doped nitrogen into CNTs and synthesized highly active CNT@NCNT for the OER as a catalyst.[251] The superior OER activity is ascribed to the highly exposed integrated N atoms present on the surface with the combined mechanical stability of the undisrupted inner walls of CNTs. Likewise, the Kallio group doped nitrogen into multiwalled CNTs (MWCNTs) and observed a considerable increase in OER performance after doping, compared with pristine MWCNTs.[221] The significant OER activity of N-doped MWCNTs is induced by pyridinic N functionalities that are electron-withdrawing. Wang's group designed a generalized approach to make highly efficient hollow N-doped CNTs as a catalyst for the OER from a MOF. The remarkable electrochemical activity is attributed to the synergistic effects from interconnected N-doped CNT structures and chemical compositions with high mechanical stability.[229]

Qiao's group synthesized dual-doped CNTs with nitrogen and sulfur inspired by the features of polydopamine (PDA), as depicted in Fig. 16a.[236] N and S doped CNTs were prepared through a two-step "graft-and-pyrolyze" route using PDA. Initially, PDA was deposited on the surface of multiwalled CNTs and sulfur was incorporated at room temperature *via* chemical grafting, and subsequent pyrolysis at 700 °C resulted in a N and S uniformly co-doped carbon framework with enhanced S-doping efficiency. Even after doping and pyrolysis, the nanotube morphology of CNTs was preserved, as shown in Fig. 16b. The OER performance of pristine and doped CNT catalysts is displayed in Fig. 16c, which shows that the N, S-CNT catalyst exhibited superior OER activity among them with an overpotential of 360 mV and a Tafel slope of 56 mV dec^{-1} (Fig. 16d). Theoretical studies show a considerable increase in spin-charge

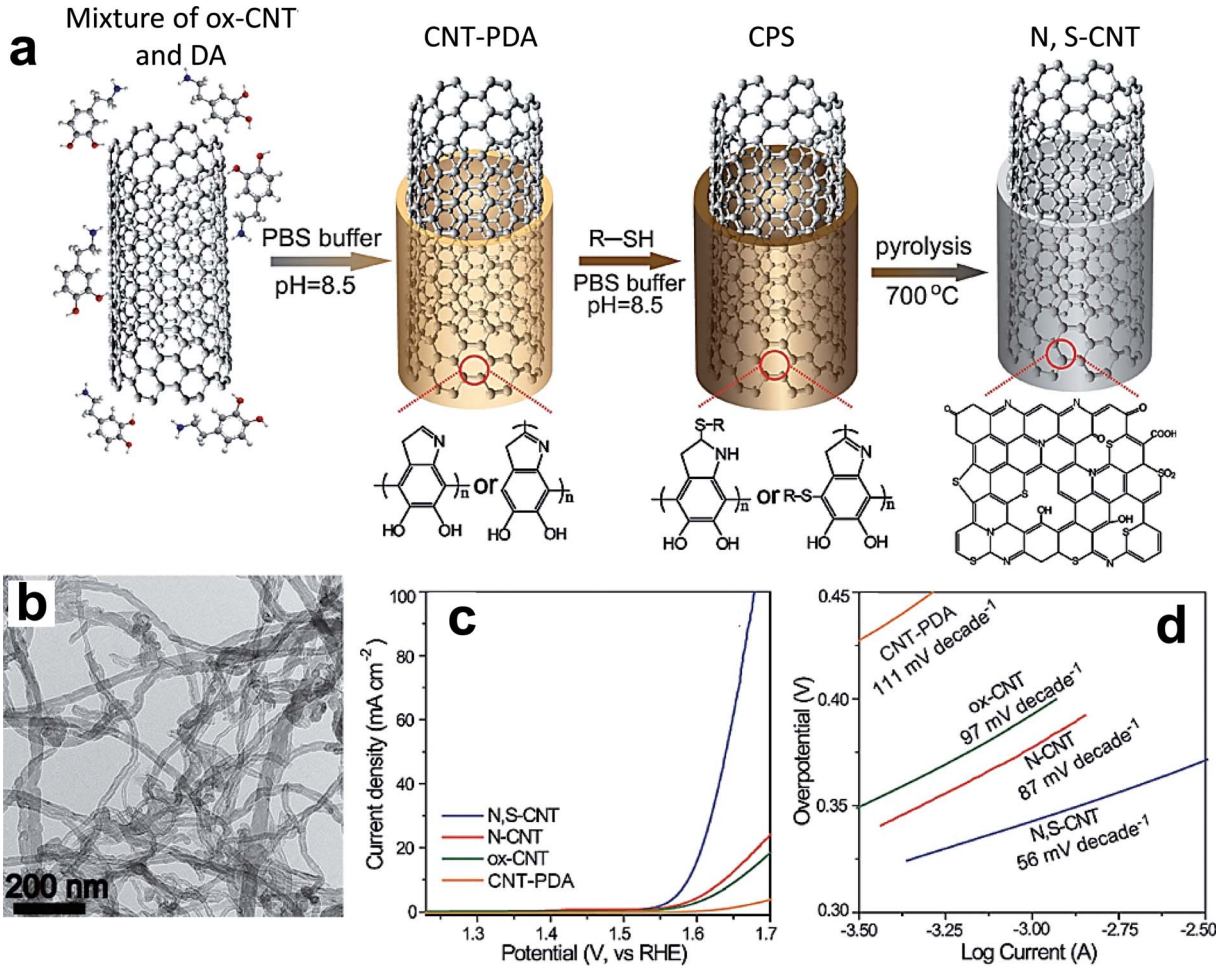

Fig. 16 (a) Fabrication of the N, S-CNT following a two-step "graft-and-pyrolyze" route. The oxidized CNT (ox-CNT) was mixed with dopamine (DA) in PBS buffer to obtain a CNT–PDA hybrid. After the addition of R-SH, CNT–PDA modified with thiol (CPS) was synthesized, which produced N, S-CNT after pyrolysis. R-SH = 2-mercaptoethanol; (b) TEM image of the N, S-CNT; (c) OER polarization curves; and (d) corresponding Tafel plots of CNT–PDA, ox-CNT, N-CNT, and N, S-CNT in 1 M KOH solution.[236] Reproduced from ref. 236 with permission, © 2017 John Wiley and Sons.

density difference among carbon atoms with doping; these carbon atoms act as electrocatalytically active sites. As a consequence, the apparent OER activity improved with dual doping compared to single doping. Liu's group has extensively studied the doping effect of oxygen on the OER performance of CNTs by synthesis *via* two different methods, *i.e.*, oxygen plasma oxidation (O-CNTs) and thermal reduction (R-CNTs).[238] O-CNTs exhibit enhanced OER activity over R-CNTs and pristine CNTs, and DFT calculations reveal that both O-CNTs and R-CNTs have the same active sites, *i.e.*, carbon near C=O. The high-water oxidation ability of O-CNTs was thought to be possible due to the presence of a high density of active sites, with high $E_{a,app}$ at the specific reaction temperature.

Lu *et al.* oxidized the surface of MWCNTs through hydrothermal annealing and electrochemical activation, which results in a highly active OER catalyst.[239] The superior OER activity originated from the formation of carbonyl functionalities on the outer wall, which altered the electronic structure of neighboring carbon atoms and facilitated adsorption of OER intermediates. Suib *et al.* fabricated a highly stable metal-free catalyst at high anodic potentials by successive two-step doping of sulfur into the MWCNTs, displaying two orders of magnitude higher turnover frequency (TOF) compared to the Ir/C catalyst.[243] The enhanced OER activity was caused by the inclusion of heterocyclic sulfur into the hexagonal rings of CNTs. Wu and co-workers developed a single-atom doped catalyst for the water oxidation reaction by coating CNTs with Fe salt and 2,2 bipyridine, followed by pyrolysis and acid leaching, yielding FeN_x species on the S and N co-doped CNT catalyst.[242] This catalyst exhibits superior OER activity in alkaline medium, as a result of high exposure of Fe atoms and synergetic effects of S and N doping.

6.3 Other carbon-based catalysts

In addition to graphene and CNTs, other forms of carbon-based catalysts were also reported for OER activity. Graphitic carbon nitride (g-C_3N_4) has a C–N structure with graphite like sp^2 bonding, which exhibits semiconducting behavior due to π-conjugation.[252] Like graphene and CNTs, g-C_3N_4 is also inactive in its pristine form, and tuning its electronic structure by doping non-metal or metal elements significantly improves its water oxidation ability.[233,240] For instance, Huang *et al.* dual-doped N and B into 3D porous g-C_3N_4 and observed superior OER activity in alkaline solution, compared to N-doped or N and P co-doped 3D g-C_3N_4.[253] It was found that the N and B co-doped g-C_3N_4 has a high population of pyrrolic and pyridinic nitrogen for enhanced OER.[222] Based on DFT calculations, Jiang and coworkers proposed doping single transition elements such as Pt, Pd, Co, Ni, and Cu into carbon nitride (CN) that could lead to a cost-efficient, highly efficient OER catalyst.[254] Specifically, the electrocatalysts of non-noble metal Co/Ni@CN and Co–O@CN exhibit excellent activity and function with extremely low overpotential. Qiao's group conducted the theoretical study and experimental validation on cobalt inclusion on g-C_3N_4 for OER activity in alkaline medium.[223] The combinative evaluation of theoretical and experimental methods reveals that metal–nitrogen M–N_2 coordination in the matrix of g-C_3N_4 is the origin of high electrocatalytic activity compared to the pristine sample. Song *et al.* studied the effect of dual metal doping in enhancing the OER activity, and doped Ni and Fe metals in tri-*s*-triazine units of g-C_3N_4 enveloped by CNTs.[232] Synchrotron-based X-ray absorption with combination of atomic microscopy indicated that the electronic configuration of both Fe and Ni was reconfigured, and the valence state of Ni was increased, and thus more OER active sites were created compared to single doping. Sun and coworkers dual-doped Ni and Fe into the framework of polymeric carbon nitride (Ni, Fe@PCN), in which superior activity was found.[233] Computational studies suggest that the enhanced OER activity of NiFeOH@PCN is a consequence of the vastly reduced energy barrier (0.10 or 0.22 eV for U $\frac{1}{4}$ 1.58 V) through synergetic contribution of adjacent Ni and Fe atoms.

In 2013, Zhao *et al.* reported N-doped carbon nanomaterials as metal-free OER catalysts other than graphene and CNTs for the first time.[227] In alkaline electrolyte, the catalyst exhibits 380 mV overpotential at a current density of 10 mA cm^{-2}, which is comparable to iridium and cobalt oxide catalysts. The pyridinic and quaternary nitrogen species shorten the diffusion path of OER intermediates. The N-doped carbon hollow cubes (NCHCs) for the OER were synthesized from biomass lysine using a NaCl-template method by Yang and coworkers.[228] The NCHCs show comparable OER activity and high endurance compared with the RuO_2/C catalyst in alkaline medium. Synergetic effects of N-doping and high specific surface area were found. Ozkan *et al.* demonstrated the OER activity of N-doped carbon nanostructures (CN_x) in an acidic medium, which showed significantly higher OER performance than the Ir/C catalyst.[255] XPS results suggested the presence of pyridinic N species for the enhanced OER activity of the CN_x catalyst. Zhao's group demonstrated a novel strategy to fabricate a highly efficient OER catalyst by synthesizing an ultra-thin N-doped holey carbon layer (HCL) on graphene through a two-step process as displayed in Fig. 17a.[231] Fig. 17b presents the HR-TEM image of Zn@G-hydro annealed at 900 °C, which exhibits nanoholes with an approximate diameter of 2 nm, as a result of Zn evaporation (N-HC@G-900). The nano-holes are not observed when zinc gluconate is not used in the synthesis (N-C@G-900). N-HC@G-900 displayed enhanced OER activity, as observed in Fig. 17c, because of pyridinic N moieties at the edges of the HCL, and the sandwiched graphene sheet provided mechanical support.

The combination of N and transition metal doping into the carbon materials effectively improved the OER performance and stability by creating more active sites.[224,225,256] For instance, Mu *et al.* co-doped Co and N into the matrix of graphene-like porous carbon nanosheets (Co@N-PGCS), which possess a high specific surface area of 1716 cm^2 g^{-1}.[256] The Co@N-PGCS catalyst showed comparable activity over the state-of-the-art catalyst IrO_2 by a synergetic effect of Co and N co-doping, and the porous surfaces open more diffusion channels. In another report, Tong and coworkers designed an efficient self-standing OER catalyst by dual doping Co and N into a graphite foam matrix (Co–N/GF).[224] The Co–N/GF catalyst prepared at 700 °C could deliver significant OER activity, compared to the catalyst

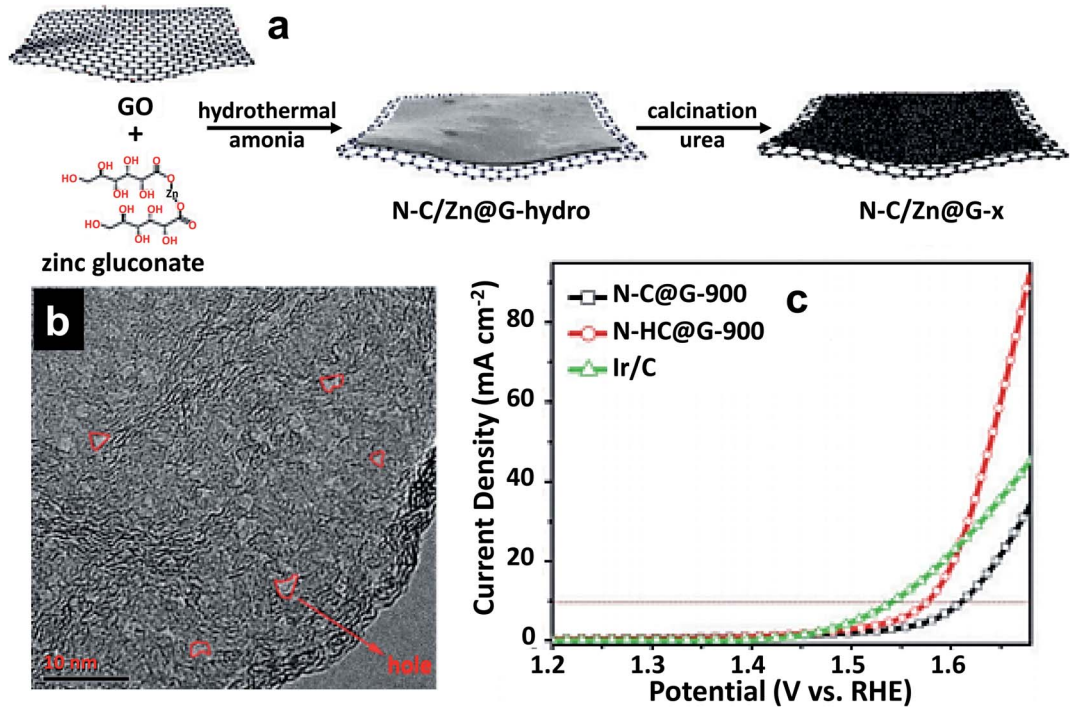

Fig. 17 (a) Schematic representation of the N-HC@G@x synthesis procedure; (b) HRTEM image of N-HC@G-900 (nanoholes marked in red); (c) LSV curves of N–C@G-900, N-HC@G-900 and Ir/C in 1 M KOH.[231] Reproduced from ref. 231 with permission, © 2018 John Wiley and Sons.

prepared at other temperatures in alkaline electrolyte. Initially, Co–N species were partly oxidized to CoOOH/Co–N. At higher anodic potentials, CoOOH was further oxidized to the most active CoO_2, which considerably promoted the oxidation of OH^- species. Wang's group, for the first time, fabricated a Co/N co-doped carbon composite for water oxidation from metal–polyphenol (Tanin) crystals, which are highly abundant in nature.[225] Co/N co-doping in a carbon composite was found to produce a synergistic effect with a high specific surface area (180 $m^2 g^{-1}$), producing excellent OER activity in the alkaline electrolyte. Lee *et al.* demonstrated the synthesis of a tri-doped carbon catalyst for acidic OER.[257] Here, they doped N, O, and TMs, such as Fe, Co, and Ni, onto the carbon, and they noticed that N/Fe/O and N/Ni/O doped carbon catalysts showed high OER activity, and N/Co/O displayed better stability.

7. Summary and concluding remarks

Searching for eco-friendly renewable energy that can replace carbon-based fossil fuels for future fuel is a prime goal of the research community. Electrochemical oxygen evolution plays a crucial role in energy storage by converting renewable energies, such as solar, wind, and tidal forms, into storable chemical fuel of hydrogen. Hence, the fundamental priority is to fabricate efficient OER catalysts that can be applied in the real world. This review summarized the research on the tuning of OER catalyst properties by doping. Doping of foreign elements can significantly alter the electrical conductivity and binding ability of OER intermediates by optimizing the host electronic structure. The considerable changes in the OER activity of metal oxides, non-metal oxides, and carbon-based catalysts *via* doping were reviewed. Experimental and theoretical studies were discussed to explain the OER mechanisms. Among the catalysts discussed above, doping in hydroxides, sulfides, selenides, and phosphides has been shown to be relatively more effective compared to the others discussed in this paper. Overall, this review outlines the systematic understanding of experimental and theoretical effects of doping on OER catalysts, which is associated with several challenges involving energy processes such as carbon dioxide reduction, nitrogen reduction, and production of hydrogen peroxide.

Considering the studies reported in this paper, an efficient OER catalyst should have optimum adsorption ability for OER intermediates, neither too weak nor too strong, and possess a good electrical conductivity. The optimized e_g filling value ($\sim$1.2) can be obtained by tuning the electronic structure of TM ions present in metal oxides, and optimizing the covalency of metal and oxygen orbitals, including other metal ions along with TM ions. An optimized surface area can be achieved by preparing nanoforms. Furthermore, the catalyst should possess excellent resistance under extreme OER conditions with high anodic potentials and a good redox center that can lose or gain electrons.

In future, the development of advanced characterization techniques, such as *in situ* XPS, Fourier-transform infrared spectroscopy (FT-IR), X-ray absorption spectroscopy, XRD, *etc.*, will provide more insights into OER intermediates on the surface of a catalyst. To design a highly stable catalyst for industrial-scale applications, it is essential to have the metric of long-term stability without dropping its initial activity evidently.

Several catalysts display high activity, but a few of them can reach long-term endurance. Besides, large surface area and porosity are the other vital parameters in producing catalysts for large-scale use, which could provide high activity with a small catalyst. Most of the catalysts described in this paper were synthesized on a lab scale, while mass production of the same type of catalyst will be challenging in terms of cost effectiveness to fulfill the practical needs. Interdisciplinary collaborative research efforts are needed in science and engineering towards widespread applications of fuel cells.

Conflicts of interest

There are no conflicts to declare.

Acknowledgements

This work was supported by the National Science Foundation (DMR-1827731).

References

1 S. Chu and A. Majumdar, *Nature*, 2012, **488**, 294–303.
2 J. Yin, A. Molini and A. Porporato, *Nat. Commun.*, 2020, **11**, 4781.
3 J. Jurasz, F. A. Canales, A. Kies, M. Guezgouz and A. Beluco, *Sol. Energy*, 2020, **195**, 703–724.
4 Z. Yan, J. L. Hitt, J. A. Turner and T. E. Mallouk, *Proc. Natl. Acad. Sci. U.S.A.*, 2020, **117**, 12558–12563.
5 N.-T. Suen, S.-F. Hung, Q. Quan, N. Zhang, Y.-J. Xu and H. M. Chen, *Chem. Soc. Rev.*, 2017, **46**, 337–365.
6 K. Scott, in *Electrochemical Methods for Hydrogen Production*, ed. K. Scott, Royal Society of Chemistry, London, UK, 2019, ch. 1, pp. 1–27.
7 T. Schuler, T. Kimura, T. J. Schmidt and F. N. Büchi, *Energy Environ. Sci.*, 2020, **13**, 2153–2166.
8 K. S. Exner, I. Sohrabnejad-Eskan and H. Over, *ACS Catal.*, 2018, **8**, 1864–1879.
9 W. Yang, Z. Wang, W. Zhang and S. Guo, *Trends Chem.*, 2019, **1**, 259–271.
10 E. Fabbri and T. J. Schmidt, *ACS Catal.*, 2018, **8**, 9765–9774.
11 K. Kannimuthu, K. Sangeetha, S. S. Sankar, A. Karmakar, R. Madhu and S. Kundu, *Inorg. Chem. Front.*, 2021, **8**, 234–272.
12 F. Song, L. Bai, A. Moysiadou, S. Lee, C. Hu, L. Liardet and X. Hu, *J. Am. Chem. Soc.*, 2018, **140**, 7748–7759.
13 Z. Chen, X. Duan, W. Wei, S. Wang and B.-J. Ni, *Nano Energy*, 2020, **78**, 105392.
14 J. Huang, Y. Jiang, T. An and M. Cao, *J. Mater. Chem. A*, 2020, **8**, 25465–25498.
15 F. Lu, M. Zhou, Y. Zhou and X. Zeng, *Small*, 2017, **13**, 1701931.
16 I. Roger, M. A. Shipman and M. D. Symes, *Nat. Rev. Chem.*, 2017, **1**, 1–13.
17 F. Dionigi and P. Strasser, *Adv. Energy Mater.*, 2016, **6**, 1600621.
18 W.-J. Yin, B. Weng, J. Ge, Q. Sun, Z. Li and Y. Yan, *Energy Environ. Sci.*, 2019, **12**, 442–462.
19 A. Dutta and N. Pradhan, *J. Phys. Chem. Lett.*, 2017, **8**, 144–152.
20 N. Han, P. Liu, J. Jiang, L. Ai, Z. Shao and S. Liu, *J. Mater. Chem. A*, 2018, **6**, 19912–19933.
21 X. Peng, Y. Yan, X. Jin, C. Huang, W. Jin, B. Gao and P. K. Chu, *Nano Energy*, 2020, **78**, 105234.
22 Q. Zhao, Z. Yan, C. Chen and J. Chen, *Chem. Rev.*, 2017, **117**, 10121–10211.
23 J. Song, C. Wei, Z.-F. Huang, C. Liu, L. Zeng, X. Wang and Z. J. Xu, *Chem. Soc. Rev.*, 2020, **49**, 2196–2214.
24 M. J. Craig, G. Coulter, E. Dolan, J. Soriano-López, E. Mates-Torres, W. Schmitt and M. García-Melchor, *Nat. Commun.*, 2019, **10**, 4993.
25 Z.-P. Wu, X. F. Lu, S.-Q. Zang and X. W. (David) Lou, *Adv. Funct. Mater.*, 2020, **30**, 1910274.
26 J. O. Bockris, *J. Chem. Phys.*, 1956, **24**, 817–827.
27 Y. Matsumoto and E. Sato, *Mater. Chem. Phys.*, 1986, **14**, 397–426.
28 W. H. Wade and N. Hackerman, *Trans. Faraday Soc.*, 1957, **53**, 1636–1647.
29 M. R. Tarasevich, A. Sadkowski and E. Yeager, in *Comprehensive Treatise of Electrochemistry: Kinetics and Mechanisms of Electrode Processes*, ed. B. E. Conway, J. O. Bockris, E. Yeager, S. U. M. Khan and R. E. White, Springer US, Boston, MA, 1983, vol. 7, pp. 301–398.
30 J. O. Bockris and T. Otagawa, *J. Electrochem. Soc.*, 1984, **131**, 290.
31 M. Kim, J. Park, M. Kang, J. Y. Kim and S. W. Lee, *ACS Cent. Sci.*, 2020, **6**, 880–891.
32 S. T. Dix, S. Lu and S. Linic, *ACS Catal.*, 2020, **10**, 10735–10741.
33 Y. Liu, Y. Ying, L. Fei, Y. Liu, Q. Hu, G. Zhang, S. Y. Pang, W. Lu, C. L. Mak, X. Luo, L. Zhou, M. Wei and H. Huang, *J. Am. Chem. Soc.*, 2019, **141**, 8136–8145.
34 A. Zunger and O. I. Malyi, *Chem. Rev.*, 2021, **121**, 3031–3060.
35 A. Goryachev, M. Etzi Coller Pascuzzi, F. Carlà, T. Weber, H. Over, E. J. M. Hensen and J. P. Hofmann, *Electrochim. Acta*, 2020, **336**, 135713.
36 O. Kasian, J.-P. Grote, S. Geiger, S. Cherevko and K. J. J. Mayrhofer, *Angew. Chem., Int. Ed.*, 2018, **57**, 2488–2491.
37 T. D. Nguyen, H. H. Nguyen, C. Dai, J. Wang and G. G. Scherer, *Int. J. Hydrogen Energy*, 2020, **45**, 46–55.
38 J. Su, R. Ge, K. Jiang, Y. Dong, F. Hao, Z. Tian, G. Chen and L. Chen, *Adv. Mater.*, 2018, **30**, 1801351.
39 W. Sun, Y. Song, X.-Q. Gong, L. Cao and J. Yang, *Chem. Sci.*, 2015, **6**, 4993–4999.
40 J. Feng, F. Lv, W. Zhang, P. Li, K. Wang, C. Yang, B. Wang, Y. Yang, J. Zhou, F. Lin, G.-C. Wang and S. Guo, *Adv. Mater.*, 2017, **29**, 1703798.
41 Y. Tian, S. Wang, E. Velasco, Y. Yang, L. Cao, L. Zhang, X. Li, Y. Lin, Q. Zhang and L. Chen, *iScience*, 2020, **23**, 100756.
42 S. Chen, H. Huang, P. Jiang, K. Yang, J. Diao, S. Gong, S. Liu, M. Huang, H. Wang and Q. Chen, *ACS Catal.*, 2020, **10**, 1152–1160.

43 W. Gou, M. Zhang, Y. Zou, X. Zhou and Y. Qu, *ChemCatChem*, 2019, **11**, 6008–6014.
44 Y. Lin, Z. Tian, L. Zhang, J. Ma, Z. Jiang, B. J. Deibert, R. Ge and L. Chen, *Nat. Commun.*, 2019, **10**, 162.
45 Y. Wang, S. Hao, X. Liu, Q. Wang, Z. Su, L. Lei and X. Zhang, *ACS Appl. Mater. Interfaces*, 2020, **12**, 37006–37012.
46 F. Lv, J. Feng, K. Wang, Z. Dou, W. Zhang, J. Zhou, C. Yang, M. Luo, Y. Yang, Y. Li, P. Gao and S. Guo, *ACS Cent. Sci.*, 2018, **4**, 1244–1252.
47 Z. Li, S. Wang, Y. Tian, B. Li, H. jun Yan, S. Zhang, Z. Liu, Q. Zhang, Y. Lin and L. Chen, *Chem. Commun.*, 2020, **56**, 1749–1752.
48 R. Ge, L. Li, J. Su, Y. Lin, Z. Tian and L. Chen, *Adv. Energy Mater.*, 2019, **9**, 1901313.
49 H. Sun, G. Chen, J. Sunarso, J. Dai, W. Zhou and Z. Shao, *ACS Appl. Mater. Interfaces*, 2018, **10**, 16939–16942.
50 G. Chen, W. Zhou, D. Guan, J. Sunarso, Y. Zhu, X. Hu, W. Zhang and Z. Shao, *Sci. Adv.*, 2017, **3**, e1603206.
51 Y.-Q. Lyu and F. Ciucci, *ACS Appl. Mater. Interfaces*, 2017, **9**, 35829–35836.
52 L. Yang, H. Chen, L. Shi, X. Li, X. Chu, W. Chen, N. Li and X. Zou, *ACS Appl. Mater. Interfaces*, 2019, **11**, 42006–42013.
53 A. Grimaud, K. J. May, C. E. Carlton, Y.-L. Lee, M. Risch, W. T. Hong, J. Zhou and Y. Shao-Horn, *Nat. Commun.*, 2013, **4**, 1–7.
54 B. Zhao, L. Zhang, D. Zhen, S. Yoo, Y. Ding, D. Chen, Y. Chen, Q. Zhang, B. Doyle, X. Xiong and M. Liu, *Nat. Commun.*, 2017, **8**, 14586.
55 Z. Li, L. Lv, J. Wang, X. Ao, Y. Ruan, D. Zha, G. Hong, Q. Wu, Y. Lan, C. Wang, J. Jiang and M. Liu, *Nano Energy*, 2018, **47**, 199–209.
56 G. Chen, Z. Hu, Y. Zhu, Z.-G. Chen, Y. Zhong, H.-J. Lin, C.-T. Chen, L. H. Tjeng, W. Zhou and Z. Shao, *J. Mater. Chem. A*, 2018, **6**, 9854–9859.
57 S. R. Ede, C. N. Collins, C. D. Posada, G. George, H. Wu, W. D. Ratcliff, Y. Lin, J. Wen, S. Han and Z. Luo, *ACS Catal.*, 2021, 4327–4337.
58 Y. Zhu, W. Zhou, J. Sunarso, Y. Zhong and Z. Shao, *Adv. Funct. Mater.*, 2016, **26**, 5862–5872.
59 Z. Wu, L.-P. Sun, T. Xia, L.-H. Huo, H. Zhao, A. Rougier and J.-C. Grenier, *J. Power Sources*, 2016, **334**, 86–93.
60 C. Su, W. Wang, Y. Chen, G. Yang, X. Xu, M. O. Tadé and Z. Shao, *ACS Appl. Mater. Interfaces*, 2015, **7**, 17663–17670.
61 Y. Guo, Y. Tong, P. Chen, K. Xu, J. Zhao, Y. Lin, W. Chu, Z. Peng, C. Wu and Y. Xie, *Adv. Mater.*, 2015, **27**, 5989–5994.
62 H. Jin, Y. Hong, J. Yoon, A. Oh, N. K. Chaudhari, H. Baik, S. H. Joo and K. Lee, *Nano Energy*, 2017, **42**, 17–25.
63 J. Xu, C. Chen, Z. Han, Y. Yang, J. Li and Q. Deng, *Nanomaterials*, 2019, **9**, 1161.
64 G. George, S. R. Ede and Z. Luo, *Fundamentals of Perovskite Oxides: Synthesis, Structure, Properties and Applications*, CRC Press, Boca Raton, Florida, 2020.
65 J. Suntivich, W. T. Hong, Y.-L. Lee, J. M. Rondinelli, W. Yang, J. B. Goodenough, B. Dabrowski, J. W. Freeland and Y. Shao-Horn, *J. Phys. Chem. C*, 2014, **118**, 1856–1863.
66 G. George, S. L. Jackson, C. Q. Luo, D. Fang, D. Luo, D. Hu, J. Wen and Z. Luo, *Ceram. Int.*, 2018, **44**, 21982–21992.
67 M. Retuerto, L. Pascual, F. Calle-Vallejo, P. Ferrer, D. Gianolio, A. G. Pereira, Á. García, J. Torrero, M. T. Fernández-Díaz, P. Bencok, M. A. Peña, J. L. G. Fierro and S. Rojas, *Nat. Commun.*, 2019, **10**, 2041.
68 Y. Zhao, L. Xu, L. Mai, C. Han, Q. An, X. Xu, X. Liu and Q. Zhang, *Proc. Natl. Acad. Sci. U.S.A.*, 2012, **109**, 19569–19574.
69 B. Hua, Y.-F. Sun, M. Li, N. Yan, J. Chen, Y.-Q. Zhang, Y. Zeng, B. Shalchi Amirkhiz and J.-L. Luo, *Chem. Mater.*, 2017, **29**, 6228–6237.
70 X. Cheng, E. Fabbri, M. Nachtegaal, I. E. Castelli, M. El Kazzi, R. Haumont, N. Marzari and T. J. Schmidt, *Chem. Mater.*, 2015, **27**, 7662–7672.
71 Y. Zhou, S. Sun, C. Wei, Y. Sun, P. Xi, Z. Feng and Z. J. Xu, *Adv. Mater.*, 2019, **31**, 1902509.
72 J. Li, D. Chu, H. Dong, D. R. Baker and R. Jiang, *J. Am. Chem. Soc.*, 2020, **142**, 50–54.
73 K.-L. Yan, J.-Q. Chi, J.-Y. Xie, B. Dong, Z.-Z. Liu, W.-K. Gao, J.-H. Lin, Y.-M. Chai and C.-G. Liu, *Renewable Energy*, 2018, **119**, 54–61.
74 C.-C. Lin and C. C. L. McCrory, *ACS Catal.*, 2017, **7**, 443–451.
75 Y. Tian, L. Cao and P. Qin, *ChemCatChem*, 2019, **11**, 4420–4426.
76 S. L. Zhang, B. Y. Guan, X. F. Lu, S. Xi, Y. Du and X. W. (David) Lou, *Adv. Mater.*, 2020, **32**, 2002235.
77 J. Swaminathan, A. B. Puthirath, M. R. Sahoo, S. K. Nayak, G. Costin, R. Vajtai, T. Sharifi and P. M. Ajayan, *ACS Appl. Mater. Interfaces*, 2019, **11**, 39706–39714.
78 C. W. Cady, G. Gardner, Z. O. Maron, M. Retuerto, Y. B. Go, S. Segan, M. Greenblatt and G. C. Dismukes, *ACS Catal.*, 2015, **5**, 3403–3410.
79 K. Lankauf, K. Cysewska, J. Karczewski, A. Mielewczyk-Gryń, K. Górnicka, G. Cempura, M. Chen, P. Jasiński and S. Molin, *Int. J. Hydrogen Energy*, 2020, **45**, 14867–14879.
80 J. S. Hong, H. Seo, Y. H. Lee, K. H. Cho, C. Ko, S. Park and K. T. Nam, *Small Methods*, 2020, **4**, 1900733.
81 X. Liu, W. Xi, C. Li, X. Li, J. Shi, Y. Shen, J. He, L. Zhang, L. Xie, X. Sun, P. Wang, J. Luo, L.-M. Liu and Y. Ding, *Nano Energy*, 2018, **44**, 371–377.
82 Z. Wang, H. Liu, R. Ge, X. Ren, J. Ren, D. Yang, L. Zhang and X. Sun, *ACS Catal.*, 2018, **8**, 2236–2241.
83 Z. Xiao, Y. Wang, Y.-C. Huang, Z. Wei, C.-L. Dong, J. Ma, S. Shen, Y. Li and S. Wang, *Energy Environ. Sci.*, 2017, **10**, 2563–2569.
84 R. Li, Y. Guo, H. Chen, K. Wang, R. Tan, B. Long, Y. Tong, P. Tsiakaras, S. Song and Y. Wang, *ACS Sustainable Chem. Eng.*, 2019, **7**, 11901–11910.
85 R. Wei, X. Bu, W. Gao, R. A. B. Villaos, G. Macam, Z.-Q. Huang, C. Lan, F.-C. Chuang, Y. Qu and J. C. Ho, *ACS Appl. Mater. Interfaces*, 2019, **11**, 33012–33021.
86 H. Xu, B. Wang, C. Shan, P. Xi, W. Liu and Y. Tang, *ACS Appl. Mater. Interfaces*, 2018, **10**, 6336–6345.
87 X. Zhang, L. An, J. Yin, P. Xi, Z. Zheng and Y. Du, *Sci. Rep.*, 2017, **7**, 43590.
88 L. Chen, H. Zhang, L. Chen, X. Wei, J. Shi and M. He, *J. Mater. Chem. A*, 2017, **5**, 22568–22575.

89 B. Cao, C. Luo, J. Lao, H. Chen, R. Qi, H. Lin and H. Peng, *ACS Omega*, 2019, **4**, 16612–16618.
90 Y. Dou, C.-T. He, L. Zhang, M. Al-Mamun, H. Guo, W. Zhang, Q. Xia, J. Xu, L. Jiang, Y. Wang, P. Liu, X.-M. Chen, H. Yin and H. Zhao, *Cell Rep. Phys. Sci.*, 2020, **1**, 100077.
91 J. Lv, X. Yang, K. Li, X. Chen, S. Sun, H.-Y. Zang, Y.-F. Chang, Y.-H. Wang and Y.-G. Li, *Nanoscale Adv.*, 2019, **1**, 4099–4108.
92 Z. Chen, C. X. Kronawitter, Y.-W. Yeh, X. Yang, P. Zhao, N. Yao and B. E. Koel, *J. Mater. Chem. A*, 2017, **5**, 842–850.
93 V. P. Tolstoy, L. I. Kuklo and L. B. Gulina, *J. Alloys Compd.*, 2019, **786**, 198–204.
94 Q. Zhou, Y. Chen, G. Zhao, Y. Lin, Z. Yu, X. Xu, X. Wang, H. K. Liu, W. Sun and S. X. Dou, *ACS Catal.*, 2018, **8**, 5382–5390.
95 S. Niu, W.-J. Jiang, Z. Wei, T. Tang, J. Ma, J.-S. Hu and L.-J. Wan, *J. Am. Chem. Soc.*, 2019, **141**, 7005–7013.
96 J. Yan, L. Kong, Y. Ji, J. White, Y. Li, J. Zhang, P. An, S. Liu, S.-T. Lee and T. Ma, *Nat. Commun.*, 2019, **10**, 2149.
97 J. W. D. Ng, M. García-Melchor, M. Bajdich, P. Chakthranont, C. Kirk, A. Vojvodic and T. F. Jaramillo, *Nat. Energy*, 2016, **1**, 1–8.
98 X. Xiong, C. You, Z. Liu, A. M. Asiri and X. Sun, *ACS Sustainable Chem. Eng.*, 2018, **6**, 2883–2887.
99 Y. Zhao, J. Zhang, W. Wu, X. Guo, P. Xiong, H. Liu and G. Wang, *Nano Energy*, 2018, **54**, 129–137.
100 C. Meng, Y.-F. Gao, X.-M. Chen, Y.-X. Li, M.-C. Lin and Y. Zhou, *ACS Sustainable Chem. Eng.*, 2019, **7**, 18055–18060.
101 W. Li, M. Li, C. Wang, Y. Wei and X. Lu, *Appl. Surf. Sci.*, 2020, **506**, 144680.
102 R. Mondal, H. Ratnawat, S. Kumar, A. Kumar and P. Singh, *RSC Adv.*, 2020, **10**, 17845–17853.
103 Y. Yang, X. Su, L. Zhang, P. Kerns, L. Achola, V. Hayes, R. Quardokus, S. L. Suib and J. He, *ChemCatChem*, 2019, **11**, 1689–1700.
104 Z. Ye, T. Li, G. Ma, Y. Dong and X. Zhou, *Adv. Funct. Mater.*, 2017, **27**, 1704083.
105 Q. Feng, J. Zou, Y. Wang, Z. Zhao, M. C. Williams, H. Li and H. Wang, *ACS Appl. Mater. Interfaces*, 2020, **12**, 4520–4530.
106 M. Huo, Z. Yang, C. Yang, Z. Gao, J. Qi, Z. Liang, K. Liu, H. Chen, H. Zheng and R. Cao, *ChemCatChem*, 2019, **11**, 1480–1486.
107 F. Cheng, J. Shen, B. Peng, Y. Pan, Z. Tao and J. Chen, *Nat. Chem.*, 2011, **3**, 79–84.
108 T. Maiyalagan, K. R. Chemelewski and A. Manthiram, *ACS Catal.*, 2014, **4**, 421–425.
109 M. H. Mendonça, M. I. Godinho, M. A. Catarino, M. I. da Silva Pereira and F. M. Costa, *Solid State Sci.*, 2002, **4**, 175–182.
110 A. S. Anindita and R. N. Singh, *Int. J. Hydrogen Energy*, 2010, **35**, 3243–3248.
111 R. N. Singh, J. P. Singh, B. Lal, M. J. K. Thomas and S. Bera, *Electrochim. Acta*, 2006, **51**, 5515–5523.
112 M. Cui, X. Ding, X. Huang, Z. Shen, T.-L. Lee, F. E. Oropeza, J. P. Hofmann, E. J. M. Hensen and K. H. L. Zhang, *Chem. Mater.*, 2019, **31**, 7618–7625.
113 I. Nikolov, R. Darkaoui, E. Zhecheva, R. Stoyanova, N. Dimitrov and T. Vitanov, *J. Electroanal. Chem.*, 1997, **429**, 157–168.
114 D. Chanda, J. Hnát, M. Paidar and K. Bouzek, *Int. J. Hydrogen Energy*, 2014, **39**, 5713–5722.
115 B. Chi, H. Lin and J. Li, *Int. J. Hydrogen Energy*, 2008, **33**, 4763–4768.
116 T. Sun, P. Liu, Y. Zhang, Z. Chen, C. Zhang, X. Guo, C. Ma, Y. Gao and S. Zhang, *Chem. Eng. J.*, 2020, **390**, 124591.
117 Z. Cai, X. Bu, P. Wang, J. C. Ho, J. Yang and X. Wang, *J. Mater. Chem. A*, 2019, **7**, 5069–5089.
118 A. Karmakar, K. Karthick, S. S. Sankar, S. Kumaravel, R. Madhu and S. Kundu, *J. Mater. Chem. A*, 2021, **9**, 1314–1352.
119 S. Anantharaj, S. Kundu and S. Noda, *Nano Energy*, 2021, **80**, 105514.
120 M. Gong and H. Dai, *Nano Res.*, 2015, **8**, 23–39.
121 Y.-F. Li and A. Selloni, *ACS Catal.*, 2014, **4**, 1148–1153.
122 L. Trotochaud, S. L. Young, J. K. Ranney and S. W. Boettcher, *J. Am. Chem. Soc.*, 2014, **136**, 6744–6753.
123 J. M. P. Martirez and E. A. Carter, *J. Am. Chem. Soc.*, 2019, **141**, 693–705.
124 M. S. Burke, M. G. Kast, L. Trotochaud, A. M. Smith and S. W. Boettcher, *J. Am. Chem. Soc.*, 2015, **137**, 3638–3648.
125 L. Trotochaud, J. K. Ranney, K. N. Williams and S. W. Boettcher, *J. Am. Chem. Soc.*, 2012, **134**, 17253–17261.
126 M. S. Burke, L. J. Enman, A. S. Batchellor, S. Zou and S. W. Boettcher, *Chem. Mater.*, 2015, **27**, 7549–7558.
127 T. A. Edison, *US Pat.*, US876445A, 1908.
128 R. L. Tichenor, *Ind. Eng. Chem.*, 1952, **44**, 973–977.
129 G. Młynarek, M. Paszkiewicz and A. Radniecka, *J. Appl. Electrochem.*, 1984, **14**, 145–149.
130 D. A. Corrigan, *J. Electrochem. Soc.*, 1987, **134**, 377.
131 S. Klaus, Y. Cai, M. W. Louie, L. Trotochaud and A. T. Bell, *J. Phys. Chem. C*, 2015, **119**, 7243–7254.
132 J. Landon, E. Demeter, N. İnoğlu, C. Keturakis, I. E. Wachs, R. Vasić, A. I. Frenkel and J. R. Kitchin, *ACS Catal.*, 2012, **2**, 1793–1801.
133 M. W. Louie and A. T. Bell, *J. Am. Chem. Soc.*, 2013, **135**, 12329–12337.
134 G. Fu, X. Wen, S. Xi, Z. Chen, W. Li, J.-Y. Zhang, A. Tadich, R. Wu, D.-C. Qi, Y. Du, J. Cheng and K. H. L. Zhang, *Chem. Mater.*, 2019, **31**, 419–428.
135 D. A. Corrigan and R. M. Bendert, *J. Electrochem. Soc.*, 1989, **136**, 723.
136 N. Li, D. K. Bediako, R. G. Hadt, D. Hayes, T. J. Kempa, F. von Cube, D. C. Bell, L. X. Chen and D. G. Nocera, *Proc. Natl. Acad. Sci. U.S.A.*, 2017, **114**, 1486–1491.
137 C. A. Kent, J. J. Concepcion, C. J. Dares, D. A. Torelli, A. J. Rieth, A. S. Miller, P. G. Hoertz and T. J. Meyer, *J. Am. Chem. Soc.*, 2013, **135**, 8432–8435.
138 Y. Sun, T. Zhang, C. Li, K. Xu and Y. Li, *J. Mater. Chem. A*, 2020, **8**, 13415–13436.
139 G. Zhang, Y.-S. Feng, W.-T. Lu, D. He, C.-Y. Wang, Y.-K. Li, X.-Y. Wang and F.-F. Cao, *ACS Catal.*, 2018, **8**, 5431–5441.
140 L. Wang, Y. Li, Q. Sun, Q. Qiang, Y. Shen, Y. Ma, Z. Wang and C. Zhao, *ChemCatChem*, 2019, **11**, 2011–2016.

141 Y. Zhou, M. Luo, Z. Zhang, W. Li, X. Shen, W. Xia, M. Zhou and X. Zeng, *Appl. Surf. Sci.*, 2018, **448**, 9–15.
142 W.-K. Gao, J.-F. Qin, K. Wang, K.-L. Yan, Z.-Z. Liu, J.-H. Lin, Y.-M. Chai, C.-G. Liu and B. Dong, *Appl. Surf. Sci.*, 2018, **454**, 46–53.
143 N. Yang, C. Tang, K. Wang, G. Du, A. M. Asiri and X. Sun, *Nano Res.*, 2016, **9**, 3346–3354.
144 X. Wang, W. Zhang, J. Zhang and Z. Wu, *ChemElectroChem*, 2019, **6**, 4550–4559.
145 Y. Guo, X. Zhou, J. Tang, S. Tanaka, Y. V. Kaneti, J. Na, B. Jiang, Y. Yamauchi, Y. Bando and Y. Sugahara, *Nano Energy*, 2020, **75**, 104913.
146 W. He, F. Wang, D. Jia, Y. Li, L. Liang, J. Zhang, Q. Hao, C. Liu, H. Liu and J. Zhao, *Nanoscale*, 2020, **12**, 24244–24250.
147 W. Gao, F. Ma, C. Wang and D. Wen, *J. Power Sources*, 2020, **450**, 227654.
148 R. Xu, Z. Xu, X. Zhang, Y. Ling, M. Li and Z. Yang, *ChemElectroChem*, 2020, **7**, 148–154.
149 L. Huang, H. Wu, H. Liu and Y. Zhang, *Electrochim. Acta*, 2019, **318**, 892–900.
150 Y. Xu, A. Sumboja, A. Groves, T. Ashton, Y. Zong and J. A. Darr, *RSC Adv.*, 2020, **10**, 41871–41882.
151 S. Dou, L. Tao, J. Huo, S. Wang and L. Dai, *Energy Environ. Sci.*, 2016, **9**, 1320–1326.
152 Z. Jing, Q. Zhao, D. Zheng, L. Sun, J. Geng, Q. Zhou and J. Lin, *J. Mater. Chem. A*, 2020, **8**, 20323–20330.
153 J. Hao, W. Yang, J. Hou, B. Mao, Z. Huang and W. Shi, *J. Mater. Chem. A*, 2017, **5**, 17811–17816.
154 Q. Hao, S. Li, H. Liu, J. Mao, Y. Li, C. Liu, J. Zhang and C. Tang, *Catal. Sci. Technol.*, 2019, **9**, 3099–3108.
155 H. Liu, Z. Liu, F. Wang and L. Feng, *Chem. Eng. J.*, 2020, **397**, 125507.
156 F. Zhang, Y. Ge, H. Chu, P. Dong, R. Baines, Y. Pei, M. Ye and J. Shen, *ACS Appl. Mater. Interfaces*, 2018, **10**, 7087–7095.
157 W. He, D. Jia, J. Cheng, F. Wang, L. Zhang, Y. Li, C. Liu, Q. Hao and J. Zhao, *Catal. Sci. Technol.*, 2020, **10**, 7581–7590.
158 Y. Ding, H. Li and Y. Hou, *Int. J. Hydrogen Energy*, 2018, **43**, 19002–19009.
159 C. Liu, D. Jia, Q. Hao, X. Zheng, Y. Li, C. Tang, H. Liu, J. Zhang and X. Zheng, *ACS Appl. Mater. Interfaces*, 2019, **11**, 27667–27676.
160 Q. Liu, L. Xie, Z. Liu, G. Du, A. M. Asiri and X. Sun, *Chem. Commun.*, 2017, **53**, 12446–12449.
161 A. Zare, A. Bayat, E. Saievar-Iranizad and H. Naffakh-Moosavy, *J. Electroanal. Chem.*, 2020, **878**, 114595.
162 X. Zhao, H. Zhang, Y. Yan, J. Cao, X. Li, S. Zhou, Z. Peng and J. Zeng, *Angew. Chem.*, 2017, **129**, 334–338.
163 Y. Zuo, D. Rao, S. Ma, T. Li, Y. H. Tsang, S. Kment and Y. Chai, *ACS Nano*, 2019, **13**, 11469–11476.
164 D. Liang, J. Mao, P. Liu, J. Li, J. Yan and W. Song, *Int. J. Hydrogen Energy*, 2020, **45**, 27047–27055.
165 F. Ming, H. Liang, H. Shi, X. Xu, G. Mei and Z. Wang, *J. Mater. Chem. A*, 2016, **4**, 15148–15155.
166 H. Kang, H. Li, X. Zhao, L. Yang and S. Xu, *Ceram. Int.*, 2020, **46**, 2792–2797.
167 J. Dai, D. Zhao, W. Sun, X. Zhu, L.-J. Ma, Z. Wu, C. Yang, Z. Cui, L. Li and S. Chen, *ACS Catal.*, 2019, **9**, 10761–10772.
168 X. Wei, Y. Xie, M. Liu, J. Zhou, A. Zhou, P. He, Y. Dou and J.-R. Li, *APL Mater.*, 2019, **7**, 101106.
169 J. Li, G. Liu, B. Liu, Z. Min, D. Qian, J. Jiang and J. Li, *Electrochim. Acta*, 2018, **265**, 577–585.
170 Z. Zou, X. Wang, J. Huang, Z. Wu and F. Gao, *J. Mater. Chem. A*, 2019, **7**, 2233–2241.
171 L. Lin, M. Chen and L. Wu, *ACS Appl. Energy Mater.*, 2019, **2**, 4737–4744.
172 J. Du, Z. Zou, C. Liu and C. Xu, *Nanoscale*, 2018, **10**, 5163–5170.
173 M. Ghaemmaghami, Y. Yamini, E. Saievar-Iranizad and A. Bayat, *Sustainable Energy Fuels*, 2020, **4**, 1150–1156.
174 Y. Du, G. Cheng and W. Luo, *Nanoscale*, 2017, **9**, 6821–6825.
175 Y. Tuo, X. Wang, C. Chen, X. Feng, Z. Liu, Y. Zhou and J. Zhang, *Electrochim. Acta*, 2020, **335**, 135682.
176 B. Mohanty, B. K. Jena, M. Kandasamy, N. Dalai, R. K. Sahu, R. M. Kadam, B. Chakraborty and B. Jena, *Sustainable Energy Fuels*, 2020, **4**, 3058–3065.
177 K. Zhang, G. Zhang, J. Qu and H. Liu, *Small*, 2020, **16**, 1907001.
178 S. Shit, S. Bolar, N. C. Murmu and T. Kuila, *ACS Sustainable Chem. Eng.*, 2019, **7**, 18015–18026.
179 W. Gao, F. Ma, C. Wang and D. Wen, *J. Power Sources*, 2020, **450**, 227654.
180 L. Lei, D. Huang, C. Zhang, R. Deng, S. Chen and Z. Li, *J. Catal.*, 2020, **385**, 129–139.
181 B. Garlyyev, J. Fichtner, O. Piqué, O. Schneider, A. S. Bandarenka and F. Calle-Vallejo, *Chem. Sci.*, 2019, **10**, 8060–8075.
182 Y. Dou, C.-T. He, L. Zhang, H. Yin, M. Al-Mamun, J. Ma and H. Zhao, *Nat. Commun.*, 2020, **11**, 1664.
183 J. Kupka and A. Budniok, *J. Appl. Electrochem.*, 1990, **20**, 1015–1020.
184 C. Lin, P. Wang, H. Jin, J. Zhao, D. Chen, S. Liu, C. Zhang and S. Mu, *Dalton Trans.*, 2019, **48**, 16555–16561.
185 P. Wang, Z. Pu, Y. Li, L. Wu, Z. Tu, M. Jiang, Z. Kou, I. S. Amiinu and S. Mu, *ACS Appl. Mater. Interfaces*, 2017, **9**, 26001–26007.
186 Y. Li, F. Li, Y. Zhao, S.-N. Li, J.-H. Zeng, H.-C. Yao and Y. Chen, *J. Mater. Chem. A*, 2019, **7**, 20658–20666.
187 F. Li, Y. Bu, Z. Lv, J. Mahmood, G.-F. Han, I. Ahmad, G. Kim, Q. Zhong and J.-B. Baek, *Small*, 2017, **13**, 1701167.
188 H. Sun, Y. Min, W. Yang, Y. Lian, L. Lin, K. Feng, Z. Deng, M. Chen, J. Zhong, L. Xu and Y. Peng, *ACS Catal.*, 2019, **9**, 8882–8892.
189 N. Suo, X. Han, C. Chen, X. He, Z. Dou, Z. Lin, L. Cui and J. Xiang, *Electrochim. Acta*, 2020, **333**, 135531.
190 C. Ray, S. C. Lee, B. Jin, A. Kundu, J. H. Park and S. C. Jun, *ACS Sustainable Chem. Eng.*, 2018, **6**, 6146–6156.
191 Q. Zhang, D. Yan, Z. Nie, X. Qiu, S. Wang, J. Yuan, D. Su, G. Wang and Z. Wu, *ACS Appl. Energy Mater.*, 2018, **1**, 571–579.

192 H.-W. Man, C.-S. Tsang, M. M.-J. Li, J. Mo, B. Huang, L. Y. S. Lee, Y. Leung, K.-Y. Wong and S. C. E. Tsang, *Chem. Commun.*, 2018, **54**, 8630–8633.
193 T. E. Rosser, J. P. S. Sousa, Y. Ziouani, O. Bondarchuk, D. Y. Petrovykh, X.-K. Wei, J. J. L. Humphrey, M. Heggen, Y. V. Kolen'ko and A. J. Wain, *Catal. Sci. Technol.*, 2020, **10**, 2398–2406.
194 M. Wang, W. Fu, L. Du, Y. Wei, P. Rao, L. Wei, X. Zhao, Y. Wang and S. Sun, *Appl. Surf. Sci.*, 2020, **515**, 146059.
195 P. Xu, L. Qiu, L. Wei, Y. Liu, D. Yuan, Y. Wang and P. Tsiakaras, *Catal. Today*, 2020, **355**, 815–821.
196 Z. Shao, J. Sun, N. Guo, F. He, K. Huang, F. Tian and Q. Wang, *J. Power Sources*, 2019, **422**, 33–41.
197 W. Xi, G. Yan, Z. Lang, Y. Ma, H. Tan, H. Zhu, Y. Wang and Y. Li, *Small*, 2018, **14**, 1802204.
198 H. Fan, W. Chen, G. Chen, J. Huang, C. Song, Y. Du, C. Li and K. (Ken) Ostrikov, *Appl. Catal., B*, 2020, **268**, 118440.
199 T. L. Luyen Doan, D. T. Tran, D. C. Nguyen, H. Tuan Le, N. H. Kim and J. H. Lee, *Appl. Catal., B*, 2020, **261**, 118268.
200 M. A. R. Anjum, M. D. Bhatt, M. H. Lee and J. S. Lee, *Chem. Mater.*, 2018, **30**, 8861–8870.
201 Z. Yin, Y. Sun, Y. Jiang, F. Yan, C. Zhu and Y. Chen, *ACS Appl. Mater. Interfaces*, 2019, **11**, 27751–27759.
202 T. Liu, M. Li, X. Bo and M. Zhou, *ACS Sustainable Chem. Eng.*, 2018, **6**, 11457–11465.
203 Y. Sun, T. Zhang, X. Li, D. Liu, G. Liu, X. Zhang, X. Lyu, W. Cai and Y. Li, *Chem. Commun.*, 2017, **53**, 13237–13240.
204 X. Bai, Q. Wang, G. Xu, Y. Ning, K. Huang, F. He, Z. Wu and J. Zhang, *Chem.–Eur. J.*, 2017, **23**, 16862–16870.
205 F.-C. Shen, S.-N. Sun, Z.-F. Xin, S.-L. Li, L.-Z. Dong, Q. Huang, Y.-R. Wang, J. Liu and Y.-Q. Lan, *Appl. Catal., B*, 2019, **243**, 470–480.
206 M. A. R. Anjum, M. H. Lee and J. S. Lee, *ACS Catal.*, 2018, **8**, 8296–8305.
207 X. Ma, K. Li, X. Zhang, B. Wei, H. Yang, L. Liu, M. Zhang, X. Zhang and Y. Chen, *J. Mater. Chem. A*, 2019, **7**, 14904–14915.
208 X. Zhu, X. Zhang, L. Huang, Y. Liu, H. Zhang and S. Dong, *Chem. Commun.*, 2019, **55**, 9995–9998.
209 X. Jia, M. Wang, G. Liu, Y. Wang, J. Yang and J. Li, *Int. J. Hydrogen Energy*, 2019, **44**, 24572–24579.
210 S. Xu, M. Wang, G. Saranya, N. Chen, L. Zhang, Y. He, L. Wu, Y. Gong, Z. Yao, G. Wang, Z. Wang, S. Zhao, H. Tang, M. Chen and H. Gou, *Appl. Catal., B*, 2020, **268**, 118385.
211 H. Fan, H. Yu, Y. Zhang, Y. Zheng, Y. Luo, Z. Dai, B. Li, Y. Zong and Q. Yan, *Angew. Chem., Int. Ed.*, 2017, **56**, 12566–12570.
212 S. Zhang, G. Gao, J. Hao, M. Wang, H. Zhu, S. Lu, F. Duan, W. Dong, M. Du and Y. Zhao, *ACS Appl. Mater. Interfaces*, 2019, **11**, 43261–43269.
213 Q. Liang, G. Brocks, X. Zhang and A. Bieberle-Hütter, *J. Phys. Chem. C*, 2019, **123**, 26289–26298.
214 H. Yang, Y. Hu, D. Huang, T. Xiong, M. Li, M.-S. Balogun and Y. Tong, *Mater. Today Chem.*, 2019, **11**, 1–7.
215 Y. Wang, Q. Wu, B. Zhang, L. Tian, K. Li and X. Zhang, *Catalysts*, 2020, **10**, 1164.
216 N. Han, K. R. Yang, Z. Lu, Y. Li, W. Xu, T. Gao, Z. Cai, Y. Zhang, V. S. Batista, W. Liu and X. Sun, *Nat. Commun.*, 2018, **9**, 924.
217 Y. Xu, M. Kraft and R. Xu, *Chem. Soc. Rev.*, 2016, **45**, 3039–3052.
218 K. Gong, F. Du, Z. Xia, M. Durstock and L. Dai, *Science*, 2009, **323**, 760–764.
219 J. Wang, H. Kong, J. Zhang, Y. Hao, Z. Shao and F. Ciucci, *Prog. Mater. Sci.*, 2021, **116**, 100717.
220 X. Liu and L. Dai, *Nat. Rev. Mater.*, 2016, **1**, 1–12.
221 F. Davodi, M. Tavakkoli, J. Lahtinen and T. Kallio, *J. Catal.*, 2017, **353**, 19–27.
222 T. Sun, J. Wang, C. Qiu, X. Ling, B. Tian, W. Chen and C. Su, *Adv. Sci.*, 2018, **5**, 1800036.
223 Y. Zheng, Y. Jiao, Y. Zhu, Q. Cai, A. Vasileff, L. H. Li, Y. Han, Y. Chen and S.-Z. Qiao, *J. Am. Chem. Soc.*, 2017, **139**, 3336–3339.
224 Y. Tong, X. Yu, H. Wang, B. Yao, C. Li and G. Shi, *ACS Catal.*, 2018, **8**, 4637–4644.
225 J. Wei, Y. Liang, Y. Hu, B. Kong, J. Zhang, Q. Gu, Y. Tong, X. Wang, S. P. Jiang and H. Wang, *Angew. Chem., Int. Ed.*, 2016, **55**, 12470–12474.
226 J. Zhang and L. Dai, *Angew. Chem., Int. Ed.*, 2016, **55**, 13296–13300.
227 Y. Zhao, R. Nakamura, K. Kamiya, S. Nakanishi and K. Hashimoto, *Nat. Commun.*, 2013, **4**, 2390.
228 X. Zheng, X. Cao, X. Li, J. Tian, C. Jin and R. Yang, *Nanoscale*, 2017, **9**, 1059–1067.
229 B. Y. Xia, Y. Yan, N. Li, H. B. Wu, X. W. (David) Lou and X. Wang, *Nat. Energy*, 2016, **1**, 1–8.
230 H. B. Yang, J. Miao, S.-F. Hung, J. Chen, H. B. Tao, X. Wang, L. Zhang, R. Chen, J. Gao, H. M. Chen, L. Dai and B. Liu, *Sci. Adv.*, 2016, **2**, e1501122.
231 J. Sun, S. E. Lowe, L. Zhang, Y. Wang, K. Pang, Y. Wang, Y. Zhong, P. Liu, K. Zhao, Z. Tang and H. Zhao, *Angew. Chem., Int. Ed.*, 2018, **57**, 16511–16515.
232 D. Liu, S. Ding, C. Wu, W. Gan, C. Wang, D. Cao, Z. ur Rehman, Y. Sang, S. Chen, X. Zheng, Y. Wang, B. Ge and L. Song, *J. Mater. Chem. A*, 2018, **6**, 6840–6846.
233 C. Wu, X. Zhang, Z. Xia, M. Shu, H. Li, X. Xu, R. Si, A. I. Rykov, J. Wang, S. Yu, S. Wang and G. Sun, *J. Mater. Chem. A*, 2019, **7**, 14001–14010.
234 H.-J. Qiu, P. Du, K. Hu, J. Gao, H. Li, P. Liu, T. Ina, K. Ohara, Y. Ito and M. Chen, *Adv. Mater.*, 2019, **31**, 1900843.
235 Y. Li, Z.-S. Wu, P. Lu, X. Wang, W. Liu, Z. Liu, J. Ma, W. Ren, Z. Jiang and X. Bao, *Adv. Sci.*, 2020, **7**, 1903089.
236 K. Qu, Y. Zheng, Y. Jiao, X. Zhang, S. Dai and S.-Z. Qiao, *Adv. Energy Mater.*, 2017, **7**, 1602068.
237 S. Chen, J. Duan, Y. Zheng, X. Chen, X. W. Du, M. Jaroniec and S.-Z. Qiao, *Energy Storage Mater.*, 2015, **1**, 17–24.
238 L. Li, H. Yang, J. Miao, L. Zhang, H.-Y. Wang, Z. Zeng, W. Huang, X. Dong and B. Liu, *ACS Energy Lett.*, 2017, **2**, 294–300.
239 X. Lu, W.-L. Yim, B. H. R. Suryanto and C. Zhao, *J. Am. Chem. Soc.*, 2015, **137**, 2901–2907.
240 T. Y. Ma, J. Ran, S. Dai, M. Jaroniec and S. Z. Qiao, *Angew. Chem.*, 2015, **127**, 4729–4733.

241 Z. Xiao, X. Huang, L. Xu, D. Yan, J. Huo and S. Wang, *Chem. Commun.*, 2016, **52**, 13008–13011.
242 P. Chen, T. Zhou, L. Xing, K. Xu, Y. Tong, H. Xie, L. Zhang, W. Yan, W. Chu, C. Wu and Y. Xie, *Angew. Chem., Int. Ed.*, 2017, **56**, 610–614.
243 A. M. El-Sawy, I. M. Mosa, D. Su, C. J. Guild, S. Khalid, R. Joesten, J. F. Rusling and S. L. Suib, *Adv. Energy Mater.*, 2016, **6**, 1501966.
244 D. G. Papageorgiou, I. A. Kinloch and R. J. Young, *Prog. Mater. Sci.*, 2017, **90**, 75–127.
245 Z. Zhao, M. Li, L. Zhang, L. Dai and Z. Xia, *Adv. Mater.*, 2015, **27**, 6834–6840.
246 Z. Lin, G. H. Waller, Y. Liu, M. Liu and C. Wong, *Carbon*, 2013, **53**, 130–136.
247 Z. Zhao and Z. Xia, *ACS Catal.*, 2016, **6**, 1553–1558.
248 G.-L. Chai, K. Qiu, M. Qiao, M.-M. Titirici, C. Shang and Z. Guo, *Energy Environ. Sci.*, 2017, **10**, 1186–1195.
249 V. N. Popov, *Mater. Sci. Eng., R*, 2004, **43**, 61–102.
250 Z. Luo, A. Oki, L. Carson, L. Adams, G. Neelgund, N. Soboyejo, G. Regisford, M. Stewart, K. Hibbert, G. Beharie, C. Kelly-Brown and P. Traisawatwong, *Chem. Phys. Lett.*, 2011, **513**, 88–93.
251 G.-L. Tian, Q. Zhang, B. Zhang, Y.-G. Jin, J.-Q. Huang, D. S. Su and F. Wei, *Adv. Funct. Mater.*, 2014, **24**, 5956–5961.
252 M. Inagaki, T. Tsumura, T. Kinumoto and M. Toyoda, *Carbon*, 2019, **141**, 580–607.
253 X. Huang, Q. Wang, D. Jiang and Y. Huang, *Catal. Commun.*, 2017, **100**, 89–92.
254 X. Li, P. Cui, W. Zhong, J. Li, X. Wang, Z. Wang and J. Jiang, *Chem. Commun.*, 2016, **52**, 13233–13236.
255 K. Mamtani, D. Jain, D. Dogu, V. Gustin, S. Gunduz, A. C. Co and U. S. Ozkan, *Appl. Catal., B*, 2018, **220**, 88–97.
256 X. Liu, I. S. Amiinu, S. Liu, K. Cheng and S. Mu, *Nanoscale*, 2016, **8**, 13311–13320.
257 S. Yang, T. Zhang, G. Li, L. Yang and J. Y. Lee, *Energy Storage Mater.*, 2017, **6**, 140–148.